



Paola Machado Barreto Manhães

**Health Assessment of Concrete Structures
with GPR**

Tese de Doutorado

Thesis presented to the Programa de Pós-Graduação em Engenharia Civil of PUC-Rio in partial fulfillment of the requirements for the degree of Doutora em Engenharia Civil.

Advisor: :Prof. José Tavares Araruna Júnior
Co-advisor : Dr. Neil Lennart Anderson

Rio de Janeiro
January 2020

Paola Machado Barreto Manhães

**Health Assessment of Concrete Structures
with GPR**

Thesis presented to the Programa de Pós-Graduação em Engenharia Civil of PUC-Rio in partial fulfillment of the requirements for the degree of Doutora em Engenharia Civil.

Prof. José Tavares Araruna Júnior

Advisor

Departamento de Engenharia Civil e Ambiental –
PUC-Rio

Prof. Genda Chen

Missouri S&T

Dr. Giuseppe Barbosa Guimarães

GBG Engenharia & Consultoria Ltda

Prof. André Bezerra dos Santos

UFC

Prof^a. Deane de Mesquita Roehl

Departamento de Engenharia Civil e Ambiental –
PUC-Rio

Prof. Flávio de Andrade Silva

Departamento de Engenharia Civil e Ambiental –
PUC-Rio

Rio de Janeiro, January 17th, 2020



All rights reserved.

Paola Machado Barreto Manhães

Paola Machado Barreto Manhães holds a B.Sc. and an M.Sc. degrees in Civil Engineering (Geotechnics) from the State University of Norte Fluminense Darcy Ribeiro, Brazil. She has carried out research on centrifuge physical modeling, X-ray microtomography and digital image processing. At the present moment, Mrs. Manhães is involved with structural health monitoring of reinforced concrete structures using a geophysical radar technique. She provides support and assistance to Geochemistry Group and Multiphysical Modeling and Simulation Group at Tecgraf Institute in a digital image processing field.

Bibliographic data

Manhães, Paola Machado Barreto

Health Assessment of Concrete Structures with GPR / Paola Machado Barreto Manhães ; advisor: José Tavares Araruna Júnior ; co-advisor: Neil Lennart Anderson. – 2020.

136 f. : il. color. ; 30 cm

Tese (doutorado)–Pontifícia Universidade Católica do Rio de Janeiro, Departamento de Engenharia Civil e Ambiental, 2020.

Inclui bibliografia

1. Engenharia Civil e Ambiental - Teses. 2. Investigação da saúde de estruturas. 3. Controle estrutural. 4. Estruturas de concreto. 5. GPR. I. Araruna Júnior, José Tavares. II. Anderson, Neil Lennart. III. Pontifícia Universidade Católica do Rio de Janeiro. Departamento de Engenharia Civil e Ambiental. IV. Título.

CDD: 624

Acknowledgments

The space dedicated to gratitude is represented a bit herein, and represent the many contributions to my evolution as research and, mostly, as a person.

Firstly, I would like to thank CAPES for the scholarship granted, which enabled the research that gave origin to this thesis.

To the Graduate Program in Civil Engineering of the Pontifical Catholic University of Rio de Janeiro, I thank the possibility of developing the thesis. To all professors of the department for all the dedication and attention in which they provide to the students.

I also want to thank all the staff of the department, always attentive and patient, especially Rogério, Euclides, Jhansen, José and Rita.

To my advisor José Araruna, who guided me in the doctorate and life. Thank you for the advice, encouragement and conversations during this experience. In the work of guidance, his serenity and objectivity were precise.

To my co-advisor Neil Anderson, a dedicated professional and incredible geophysicist with whom I had the pleasure of having contact. His theoretical expertise was essential for the development of the research.

To Ghenda Chen for accepting to participate as a visiting researcher at the Missouri University of Science and Technology Transportation Center. The acquisition of the processing software was essential for the production of a more complete work.

To my friends who very much shared this experience of accomplishing the visiting at the Missouri University of Science and Technology, specially Adbdullah Hadi, Rairu Penna and Lais Penna for their kind assistance.

To Eric Vallotti for giving way his short beams which were built on his doctorate research, to Weiler Filho and João Lemgruber for helping me with short beams photography.

To my dear friends who very much shared this experience of accomplishing the doctorate's degree in PUC-Rio: Géremy Freitas, Claudia Dominoni, Daiana Eringer, Leticia Oliveira, Raylane Castoldi, Lourdes Maria Souza, Marcelo Sampaio, Ana Carolina Trindade, Fernanda Salgado, Kíssila Botelho, Filipe Sá, Vitor Monteiro.

To my family, Margaret, João Carlos, Carla e Tuane, for all support deposited. Your sacrifices, love and investments have turned into determination.

Anyway, thank you to everyone who, in a way, was part of that journey.

This study was financed in part by the Coordenação de Aperfeiçoamento de Pessoal de Nível Superior - Brasil (CAPES) - Finance Code 001

Abstract

Machado Barreto Manhães, Paola; Tavares Araruna Júnior, José (Advisor); Lennart Anderson, Neil (Co-advisor). **Health Assessment of Concrete Structures with GPR**. Rio de Janeiro, 2020. 136p. Tese de doutorado – Departamento de Engenharia Civil e Ambiental, Pontifícia Universidade Católica do Rio de Janeiro.

This thesis presented the experimental issues concerning the health assessment of concrete structures with the desire to replace the traditional subjective assessment of civil structures with a more objective assessment using the GPR. The emphasis here was on validating a sound procedure of health assessment for buildings, wastewater treatment stations and concrete test specimens. GPR was chosen since it is considered one of the most popular non-destructive testing methods adopted for concrete structure imaging because of its relative insensitivity to ambient conditions, high resolution, effectiveness, and availability of real-time images. The research carried out in this thesis emphasized on as-built designing, damage detection, location, and quantification, which is of interest in the context of structural control. The results presented in this thesis demonstrated that the ground-penetrating radar (GPR) could be used as a useful tool in producing structural detailing drawings since it can provide the thickness of covering concrete and the depth and location of reinforcement. The results also show that deterioration of concrete mass and corrosion of its rebars could be also be assessed by the attributes provided by a GPR scan. Damages are detected by reducing the depth of the reflector, increasing the amplitude of EM waves and increasing attenuation expressed by the dB decay. Further to these, it was also indicated that the rebar condition can be assessed through slices at different times/depths obtained from a 3-D survey. In addition to that, the program also assessed the feasibility of GPR in evaluating steel fiber distribution within short beam test specimens used in several standard test methods for determining mechanical properties. Results revealed that the distribution of steel fibers within a beam is not uniform. Digital and processed images showed that fibers are not evenly distributed and there is a disparity between

the numbers of fibers in different sections of the short beam. A statistical analysis performed on the results also found that the distance between fibers also varies within the short beam. When sketches of the emitted and recorded GPR signal in a single radar trace mode are compared to the digital and processed images it was perceived a good relationship between the GPR signal and the distribution of steel fibers within the short beam. It was additionally noticed that GPR signal amplitude not only supplies information on how the fibers are close to each other but also reflects regions with the absence of fibers. Results have also shown that a GPR system using a high-frequency antenna could assess weaker zones of steel fiber reinforcement within self-consolidating concrete short beams.

Keywords

Health Assessment, Structural Control, Concrete Structures, GPR

Resumo

Machado Barreto Manhães, Paola; Tavares Araruna Júnior, José (Advisor); Lennart Anderson, Neil (Co-advisor). **Análise da Saúde de Estruturas de Concreto com o GPR**. Rio de Janeiro, 2020. 136p. Tese de doutorado – Departamento de Engenharia Civil e Ambiental, Pontifícia Universidade Católica do Rio de Janeiro.

Essa tese apresenta as questões experimentais relativas à avaliação da saúde de estruturas de concreto com o objetivo de propor uma alternativa à avaliação subjetiva tradicional de estruturas civis, complementando-a com uma avaliação mais objetiva utilizando o GPR. A ênfase foi na validação de um procedimento sólido de avaliação da saúde de edifícios, de estações de tratamento de águas residuais e de túneis. O GPR foi escolhido por ser considerado um dos métodos de ensaios não destrutivos mais adotados para investigação de estruturas de concreto devido à sua relativa insensibilidade às condições ambientais, ter alta resolução, eficácia e disponibilidade de resultados preliminares em tempo real. A pesquisa desenvolvida nessa tese teve ênfase na verificação de *as-built* da construção, detecção de danos, locação e quantificação de armadura que são de grande interesse no contexto do controle estrutural. Os resultados apresentados nessa tese demonstram que o *Ground Penetrating Radar* (GPR) pode ser uma ferramenta muito útil para produzir projetos de detalhamento estrutural já que ele pode estimar espessura de recobrimento de concreto e profundidade e locação do reforço. Os resultados também mostram que a deterioração do concreto, bem como a corrosão das barras podem ser verificados após a análise de atributos fornecidos pela verificação feita com o GPR. Danos são detectados por meio da redução da profundidade do refletor, aumentando a amplitude das ondas eletromagnéticas e aumentando a atenuação expressa pelo gráfico de *dB decay*. Além disso, também verificou-se que a condição da barra de aço pode ser avaliada através de fatias em diferentes tempos/profundidade, obtidas na prospecção tridimensional. Adicionalmente, o programa experimentado também avaliou a viabilidade de empregar o GPR na avaliação da distribuição de fibras de aço em revestimento de

túnel de concreto projetado, considerando-se o GPR como uma ferramenta útil para monitoramento e mapeamento *in situ* durante a o método de construção NATM de túneis. Os resultados dos ensaios realizados em prismas de concreto auto adensável reforçado com fibra de aço demonstraram que a distribuição das fibras não é uniforme. O processamento digital de imagem mostrou que as fibras não são distribuídas uniformemente e há variação do número de fibras em diferentes seções do prisma. A análise estatística realizada nos resultados também identificou que a distância entre as fibras também varia. Quando compara-se os resultados obtidos com o GPR e os resultados obtidos das análises digitais de imagens percebe-se uma boa relação entre ambos. Também foi observado que a amplitude do sinal do GPR não apenas fornece informações sobre a distribuição das fibras, mas também sobre regiões com ausência delas. Com base nos resultados do programa experimental, acredita-se que o GPR possa fornecer um *feedback* imediato das informações e pode ser usado como uma ferramenta de ajuste dinâmico no projeto NATM.

Palavras-chave

Saúde de Estruturas, Avaliação Estrutural, Estruturas de Concreto, GPR

Table of contents

1	Introduction	20
2	GPR: Principles and uses	23
2.1	Properties of Electromagnetic Waves	26
2.2	Physical Properties of the Medium	30
2.3	Principles of Ground Penetrating Radar (GPR) Operation	32
2.3.1	Acquisition	32
2.3.2	Data processing	38
2.4	A review of GPR application in concrete imaging	44
3	Study into the effect of steel fiber distribution on the tensile strength of reinforced self-consolidating concrete using the GPR	53
3.1	Experimental program	56
3.1.1	Short beam	56
3.1.2	GPR survey	58
3.1.3	Monotonic four-point test	60
3.1.4	Shot beam cutting	61
3.1.5	Slice imaging	62
3.2	Results and discussions	62
3.3	Conclusions	78
4	Health assessment of deteriorating reinforced concrete structures in residential buildings in coastal areas using GPR: A case study in the Brazilian Northeastern coastline	79
4.1	Theoretical information	81
4.1.1	Chloride induced corrosion	81

4.1.2	GPR principle	83
4.2	Experimental program	85
4.3	Experimental results and discussions	90
4.4	Conclusions	100
5	The use of ground penetrating radar in appraising the serviceability of a wastewater treatment plant concrete structure	101
5.1	Study site	104
5.2	GPR survey	105
5.3	Results and discussion	108
5.4	Conclusions	120
6	Conclusions	121
	References	124

List of figures

Figure 2.1. A typical GPR system for concrete scanning: 1, controller and hardware for data storage and monitoring; 2, transmitter antenna; 3, receiver antenna; 4, encoder for distance measurement.	23
Figure 2.2. Modes of propagation of the electromagnetic field. (a) Electric transverse; (b) Magnetic Transverse. (Jol, 2009)	27
Figure 2.3. Indication of the Brewster Angle in the TE and TM propagation modes, comparing with their respective angle vs. reflection coefficient.	28
Figure 2.4. The radius of the First Fresnel Zone footprint	30
Figure 2.5. Arrangements of antennas that influence polarization. Adapted from Annan (2001)	33
Figure 2.6. Photography of the transmitting and receiving antennas inside an armored antenna and its parallel position.	33
Figure 2.7. Illustration of radargrams of CMP investigations carried out with the antennas generating field in TE (a) and TM (b) (Adapted from Jandyr, 2016)	34
Figure 2.8. External agents that can influence unarmored antennas. (Adapted from Jol, 2009)	38
Figure 2.9. Possible ways of propagating the wave until it reaches the receiver (R)	39
Figure 2.10. Typical trace of an ideal, noise-free, unshielded antenna. (Annan, 2003).	40
Figure 2.11. Analysis of a trace in the processed radargram. (Adapted from Rial et al., 2009)	41
Figure 2.12. Illustration of the meaning of the variables that make up Eq. 22	43
Figure 3.1. Experimental program flowchart	56
Figure 3.2. Short beams used in the experimental program	57
Figure 3.3. GPR concrete scanning system	59
Figure 3.4. Relative dielectric permittivity determination procedure	60
Figure 3.5. The four-point test set up	61

Figure 3.6. Specimen lab saw	61
Figure 3.7. Slice imaging	62
Figure 3.8. GPR data from the determination of the average traveling velocity of the GPR wave in concrete short beams containing 0%, 0.5% and 1% steel fiber	64
Figure 3.9. Fiber distribution within a 1% fiber reinforced concrete short beam	65
Figure 3.10. Comparison between GPR signal in a single radar trace mode, digital and processed images of four slices of a 1% fiber reinforced concrete short beam	67
Figure 3.11. GPR signal amplitude	69
Figure 3.12. GPR energy attenuation	70
Figure 3.13. Schematic sketch of a radargram in greyscale mode	71
Figure 3.14. GPR survey on CP1 short beam with 0.5% fiber reinforcement	72
Figure 3.15. GPR survey on CP2 short beam with 0.5% fiber reinforcement	73
Figure 3.16. GPR survey on CP3 short beam with 0.5% fiber reinforcement	74
Figure 3.17. GPR survey on CP1 short beam with 1% fiber reinforcement	75
Figure 3.18. GPR survey on CP2 short beam with 1% fiber reinforcement	76
Figure 3.19. GPR survey on CP3 short beam with 1% fiber reinforcement	77
Figure 3.20. Shear force and bending moment diagrams for four-point bending test	78
Figure 4.1. Recent residential building collapses in Fortaleza: a) building collapse in Maraponga district after its columns failed (June 2019), b) balcony collapse in Meireles district (March 2015), and c) debris of Andrea building in Dionísio Torres dist.	80
Figure 4.2. Reinforcement corrosion and cracking patterns	83
Figure 4.3. Satellite image of Fortaleza (Google Image)	86
Figure 4.4. Building at Praia do Futuro district	86
Figure 4.5. The building at Varjota district	87
Figure 4.6. Building at Aldeota district	87
Figure 4.7. GPR survey setup at the building on Aldeota district	88
Figure 4.8. Data processing sequence	89
Figure 4.9 (cont.). Results from the GPR scan carried out at column P17 from the Aldeota district building (indicated values are in meter)	91
Figure 4.10. The traveling velocity of the GPR wave	93

Figure 4.11. GPR scanning of corroded rebar in concrete	94
Figure 4.12. Attributes derived from the GPR scan carried out at a cured unreinforced concrete short beam	96
Figure 4.13. Attributes derived from the GPR scan carried out at column P2 from the Aldeota district building	97
Figure 4.14. Attributes derived from the GPR scan carried out at column P5 from the Varjota district building	98
Figure 4.15. Position of rebars within the concrete composite slab showing embedded steel rebars possessing a different thickness of covering	98
Figure 4.16. Attributes derived from the GPR scan carried out at column P1 from the Praia do Futuro district building	99
Figure 5.1. Steel rebar corrosion on a wastewater treatment facility	102
Figure 5.2. The wastewater treatment plant under investigation	105
Figure 5.3. GPR survey targets	105
Figure 5.4. GPR survey at the sieving unit: a) cross-section on the sieving unit; b) slab between sieves #1 and #2; c) slab between sieves #2 and #3, and d) slab under sieves #4, #5, #6 and #7	106
Figure 5.5. Data processing sequence	108
Figure 5.6. Schematic sketch of a radargram in greyscale mode	109
Figure 5.7. Schematic sketch of a time slice	109
Figure 5.8. Hyperbolas on radargrams: a) upper slab between sieves #1 and #2; b) upper slab between sieves #2 and #3 and c) slab under sieves #4, #5, #6 and #7	110
Figure 5.9. GPR survey determined parameters: a) upper slab between sieves #1 and #2; b) upper slab between sieves #2 and #3 and c) slab under sieves #4, #5, #6 and #7	113
Figure 5.10. Amplitude of EM waves: a) a) upper slab between sieves #1 and #2; b) upper slab between sieves #2 and #3 and c) slab under sieves #4, #5, #6 and #7	115
Figure 5.11. GPR scan on the slab between sieve #1 and #2	116
Figure 5.12. GPR scan on the slab under sieves #4, #5, #6 and #7	117
Figure 5.13. Time slice showing rebars in the slab between sieve #1 and #2	118
Figure 5.14. Time slice showing rebars in the slab between sieve #2 and #3	118

Figure 5.15. Position where the 3-D survey took place on the slab between
sieve #2 and #3 119

Figure 5.16. Time slice showing rebars in the slab under sieves #4, #5, #6 and
#7 119

List of tables

Table 2.1. Loss by wave attenuation in the middle for 500MHz and 1GHz frequency antennas.	31
Table 2.2. Dielectric constant values for traditional materials	35
Table 2.3. Central frequency depending on the depth to be investigated	37
Table 2.4. Examples of application of GPR (adapted from Lai et al., 2018)	45
Table 3.1. Summary of different fibre distribution test method	55
Table 3.2. Mix composition of the matrix and the steel fiber self-consolidating concrete	58
Table 3.3. Statistical Analysis on the fiber distribution within the 1% fiber reinforced short beam	66
Table 3.4. Determined values of vertical resolution and maximum horizontal resolution	68
Table 4.1. Determined values of vertical resolution and horizontal resolution	93

List of symbols

\vec{B} - magnetic flux density vector

\vec{E} - electric field strength vector

\vec{J} - electric current density vector

\vec{H} - magnetic field intensity

\vec{D} - electric displacement vector

t - time

q - electric charge density

$\tilde{\sigma}$ - Electrical conductivity

$\tilde{\epsilon}$ - Dielectric permittivity

$\tilde{\mu}$ - Magnetic permeability

k- relative permittivity or dielectric constant

ϵ - scalar constant form for dielectric permittivity

ϵ_0 - permittivity of free space or vacuum ($8.89 \times 10^{-12} F/m$)

σ - scalar constant form for electrical conductivity

μ - scalar constant form for magnetic permeability

v - velocity

c - velocity of free space or vacuum ($3 \times 10^8 m/s$)

D - the antenna to the reflection surface distance

T- two-way travel time

α - attenuation

Z - electromagnetic impedance

ω – excitation

f_t – transition frequency

Z_0 – impedance of free space or vacuum (377)

R - reflection coefficient across two vertical interfaces

k_1 – relative permittivity of the target feature

k_2 - relative permittivity of the background medium

r_{vertical} - vertical resolution

$r_{\text{horizontal}}$ - horizontal resolution

τ_p - effective duration of the radar pulse

λ - wavelength

f – central frequency

L_a – loss by attenuation

R – range to the target

μ_0 – absolute magnetic susceptibility of free space

μ_r – relative magnetic susceptibility of material

ϵ_r –relative permittivity of material

$\tan \delta$ – loss tangent of material

Δz – spatial separation

Δl – dimension of the object that leads to heterogeneity

Δt – time interval

Δx – sampling space

x_r – any position in the investigation above hyperbola

x_s - any position in the investigation that is not positioned above the hyperbole

t' - the response time of the diffraction hyperbole at the point x_r

t_0 - the response time of the diffraction hyperbole crest

1 Introduction

The evolution of the civil engineering field of structural assessment has been rapid, attracting the interest and attention of the academia and the industry over the past decades. According to Housner et al. (1997), structural assessment initiated on aerospace related problems as tracking and pointing, and inflexible space structures, but then quickly moved into civil engineering and infrastructure-related issues.

Some authors, including Moyo et al. (2005), suggested that the driven force on the evolution of structural assessment was the need to improve safety and to optimize maintenance strategies. As He et al. (2011) pointed out, buildings and the civil infrastructure are deteriorating at an accelerating rate causing threats to safety, economy and human life as a consequence of extreme events, material aging and harsh environmental conditions.

A structural assessment could be defined as a practice that seeks to assess the condition or health of a structure. Ideally, such a practice should be able to appraise a structure in a way that any growth of inherent anomalies would be immediately detectable. Following Moyo et al. (op. cit.), anomalies are defined as deterioration and damage resulting from changes in material properties, geometric properties, boundary conditions, system connectivity and the loading environment of the structure.

Structural assessment of reinforced concrete structures might be accomplished by structural health monitoring (SHM) and/or non-destructive testing (NDT). Cross et al. (2013) defined SHM as any automated monitoring practice that seeks to assess the condition or health of a structure. The authors also described NDT as the assessment of a structure or component's health through non-damaging procedures (e.g., x-ray, electron microscopy, measurement of acoustic and electromagnetic emissions and full-scale vibration tests). According to Cross et al (op. cit.), NDTs occur as one-off planned events often applied to a small area of a

structure where damage is suspected to have occurred, whereas SHM aims to be continuous and global. The authors also implied that shortly, it is likely that NDT inspection will form the basis for distinguishing between health and performance anomalies for civil infrastructure where this cannot be accomplished automatically. Needless to call attention to the fact that NDT may be incorporated as part of an SHM system.

One of the most popular NDT methods adopted for civil engineering inspections is the ground penetrating radar because of its high resolution, effectiveness, and availability of real-time images. According to Lai et al. (2018), the advent of GPR started in the field of geoscience after the mid-1950s, and gradually adopted in civil engineering since the mid-1990s. The authors pointed out that the technological advancements and tremendous improvements in digital computation power that took place during the 2000s have led to the blossoming of GPR applications on civil engineering practice. Currently, as implied by Lai et al. (op. cit.), GPR uses are progressing from traditional locating, testing and evaluation of objects in small scale to imaging and diagnosis.

In the case of reinforced concrete, most applications of GPR are related to rebar detection and mapping (Perez-Gracia et al., 2008a; Barrile and Pucinotti, 2005; Lai and Poon, 2012). On the other hand, analysis of GPR surveys is focused on several directions, including:

- Object detection like steel bars, pipes, structural supports and changes in building materials (Topczewski et al., 2007; Mazurek and Łyskowski, 2012; Chang et al., 2009; Barraca et al., 2016);
- Definition of object geometry like the radius of steel bars embedded in concrete (Leucci, 2012; Zanzi and Arosio, 2013);
- Dampness, void and defects of concrete (Laurens et al., 2002; Laurens et al., 2005; Klysz and Balayssac; 2007), and
- Cracks and void detection in concrete (Maierhofer et al., 2003; Zhu and Popovics, 2005; Xie et al., 2013).

This research aims to evaluate the usefulness of GPR on the health assessment of different kinds of civil structures that uses reinforced concrete as their main building material. The author wishes to appraise the suitability of GPR in situations whereupon a detection, any anomaly could be located and its severity inferred so that decisions can be easily made as to what actions need to be taken next (e.g., an immediate halt to use of the structure, immediate repair, etc.). The author believes that civil structures are highly heterogeneous, at both the global and material levels, and a classification of damage type is essential if any prognosis is to be possible.

This thesis is organized into six chapters including this introductory chapter. The second one explain the principles and uses of GPR. The following chapters describe the health assessment surveys carried out on a) short beam test specimens used in several standard test methods for determining mechanical properties, b) residential buildings and c) a wastewater treatment plant. These chapters were formatted as journal papers, so the organization of each chapter reflects the format required to each journal they will be submitted. Finally, the last chapter shows the main conclusions obtained from the experimental program.

2 GPR: Principles and uses

GPR is a geophysical method based on the propagation of electromagnetic waves on porous media to allow the identification of properties of the media and the presence of distinct materials in the region where the investigation is carried out, without the need for an invasive or destructive investigation.

A GPR system comprises a control system, at least one transmitter antenna, at least one receiver antenna, a viewing system for monitoring the data in real-time, some means of data storage, and a distance measurement device (Figure 2.1).



Figure 2.1. A typical GPR system for concrete scanning: 1, controller and hardware for data storage and monitoring; 2, transmitter antenna; 3, receiver antenna; 4, encoder for distance measurement.

The GPR controller generates electromagnetic pulses that are passed into the transmitter antenna which then transmits into the subsurface medium. As the signal passes through this medium, parts of the signal are returned to the receiver. It is the

changing nature of the subsurface material that triggers each of these reflections. The returned signals carry information back through the receiver antenna to the controller and from there to the viewing device. Parts of the signal are returned due to the difference in electromagnetic properties between one material and the one neighboring since the radar can detect any material provided that its magnetic and/or electrical responses are different from the other materials which surround it. A computing device is used to set the controller's survey parameters (e.g., probing depth, frequency of sampling) and also to store the data for postprocessing.

As the GPR is moved across the survey area, the sequence of signals builds up a two-dimensional image of the subsurface in a plot where the x-axis represents the distance traveled by the radar and the y-axis represents the depth probed and from which each signal has been returned.

2.1 Basic Principles of Electromagnetism

In the theory of electromagnetism, Maxwell compiled the knowledge available at the time and summarized the observations about electromagnetism into four equations. The first of these is Faraday's Law, in which he observes that since the magnetic flux (\bar{B}) varies with time (t), an electric field is generated (\bar{E}). The second law is the Ampere Law, which says that an electric current (\bar{J}) gives rise to a magnetic field (\bar{H}). The third law says that the electrical displacement (\bar{D}) begins or ends in an electrical charge (q). The fourth law says that magnetic flux circuits (\bar{B}) should close on itself, because there are no free magnetic charges. All physical relationships determined by the laws of the Theory of Electromagnetism are summarized in mathematical equations presented in Eq. 1, 2, 3 and 4, respectively.

$$\bar{\nabla} \times \bar{E} = -\frac{\partial \bar{B}}{\partial t} \quad \text{Eq. 1}$$

$$\bar{\nabla} \times \bar{H} = \bar{J} + \frac{\partial \bar{D}}{\partial t} \quad \text{Eq. 2}$$

$$\bar{\nabla} \times \bar{D} = q \quad \text{Eq. 3}$$

$$\bar{\nabla} \times \bar{B} = 0 \quad \text{Eq. 4}$$

These equations summarized by Maxwell are related to the theories of classical electromagnetism and can be obtained through Ohm's law associations of electromagnetic fields with the electrical and magnetic properties of the material in which they propagate, as presented by Whitmer (1963).

The equations that describe the response of materials submitted to an electromagnetic field, relating the properties of electromagnetic fields with the electromagnetic properties of materials are called constitutive equations, presented in Eq. 5, 6 and 7.

$$\bar{J} = \tilde{\sigma} \bar{E} \quad \text{Eq. 5}$$

$$\bar{D} = \tilde{\epsilon} \bar{E} \quad \text{Eq. 6}$$

$$\bar{B} = \tilde{\mu} \bar{H} \quad \text{Eq. 7}$$

where, $\tilde{\sigma}$ is the electrical conductivity, $\tilde{\epsilon}$ is dielectric permittivity and $\tilde{\mu}$ is magnetic permeability.

Dielectric permittivity is never null, so sometimes it becomes more convenient to represent this value in a dimensional manner called relative permittivity or dielectric constant (k). The dielectric constant is calculated by the ratio between the permittivity of the material (ϵ) and the permittivity in the vacuum (ϵ_0), as presented in Eq. 8.

$$k = \frac{\epsilon}{\epsilon_0} \quad \text{Eq. 8}$$

2.2 Properties of Electromagnetic Waves

In addition to the properties of the materials studied, it is also important to know the properties of the waves. In this sense, the key properties for this understanding are velocity (v), attenuation (α), and electromagnetic impedance (Z).

At low frequencies, wave properties depend on the square root of ω (note $\omega = 2\pi f$), while at high frequencies, properties become independent of frequency. In this case, velocity, impedance, and attenuation vary depending on the properties of the material as presented in Eq. 9, 10 and 11. Therefore, for the use of GPR it is important to work at high frequencies, that is, above the transition frequency, i.e. $\left(f_t = \frac{\sigma}{2\pi\varepsilon}\right)$.

$$v = \frac{1}{\sqrt{\varepsilon\mu}} = \frac{c}{\sqrt{k}} = \frac{D}{T} \quad \text{Eq. 9}$$

$$\alpha = \frac{\mu\sigma v}{2} \quad \text{Eq. 10}$$

$$Z = \sqrt{\frac{\mu}{\varepsilon}} \quad \text{Eq. 11}$$

The GPR platform typically exhibits a gradual decrease in propagation speed and wave attenuation. This is due to two factors: the first due to the presence of water, with the onset of increasing energy absorption; and second, by the use of high frequencies that generate dispersion losses, losses that are extremely dependent on frequency.

However, another factor causes a variation in wave velocity. When a wave encounters variation of properties of the medium in which it propagates, the direction of propagation of the wave also varies. This fact is expressed by Snell's Law, whose concept refers to the theory of geometric optics proposed by Fresnel.

By introducing electromagnetic radiation into an open, hollow tube bounded by a perfect conductor and it comes across a perfect reflector, the waves will progress into the tube at an undefined distance. This hollow tube is called a waveguide and, according to Slater and Frank (1947), this concept has been applied

to microwaves and electromagnetic waves whose wavelength is in the order of dimensions of the order of centimeters to meters, which is the case of GPR antennas.

At low frequencies, rather than propagating like a guided wave, the wave tends to be dampened or attenuated.

Assuming the electromagnetic field in a waveguide, it can be considered that there are two components of electromagnetic field distribution. The two components, the electrical and the magnetic, are perpendicular to each other. In this case, when the electric field component on the z-axis is null, it is said that the electromagnetic field is distributed in an electrical cross-sectional (TE) mode, while the component of the magnetic field on the x-axis is null, it is said that the electromagnetic field is distributed in a magnetic cross-sectional (TM) mode. The distribution patterns of the electromagnetic field of TE and TM modes are presented respectively by Figures Figure 2.2.a and Figure 2.2.b.

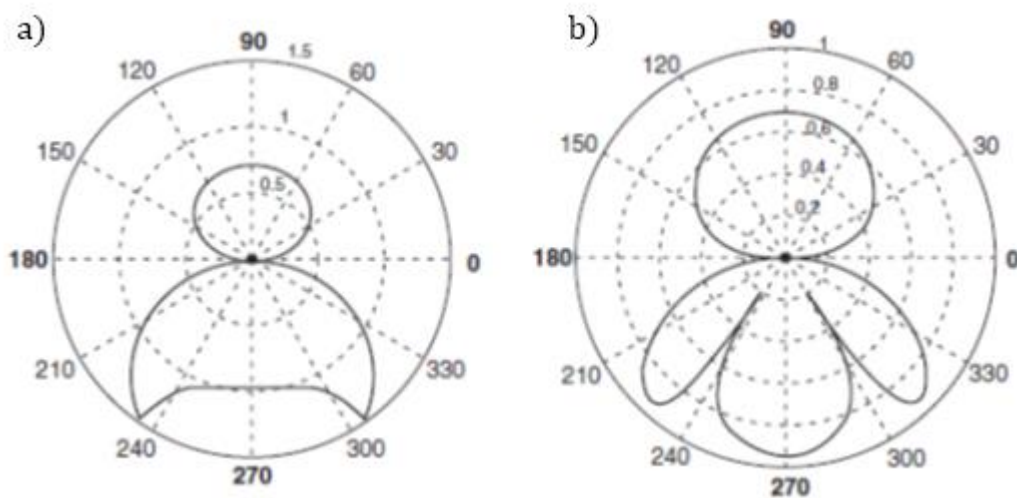


Figure 2.2. Modes of propagation of the electromagnetic field. (a) Electric transverse; (b) Magnetic Transverse. (Jol, 2009)

It can be seen from Figure 2.2 that when the investigation carried out has as propagation mode the transverse electric propagation is less deep, but with larger horizontal amplitude, already in the case of propagation by magnetic transverse the bulb reaches a greater depth. Nevertheless, this mode of propagation has an angle

increment between the 240° and 300° angles called the Brewster angle, because, according to McMichael (2010), the reflection coefficient (Eq. 12) goes to zero at this angle and all incident energy is transmitted to the dielectric medium. Figure 2.3 lists the Propagation Modes shown in Figure 2.2 with the Angle Vs. Reflection Coefficient chart, identifying the Brewster Angle.

$$R = \frac{\sqrt{k_1} - \sqrt{k_2}}{\sqrt{k_1} + \sqrt{k_2}} \quad \text{Eq. 12}$$

where R is the reflection coefficient across two vertical interfaces, k1 denotes the relative permittivity of the target feature and k2 denotes the relative permittivity of the background medium.

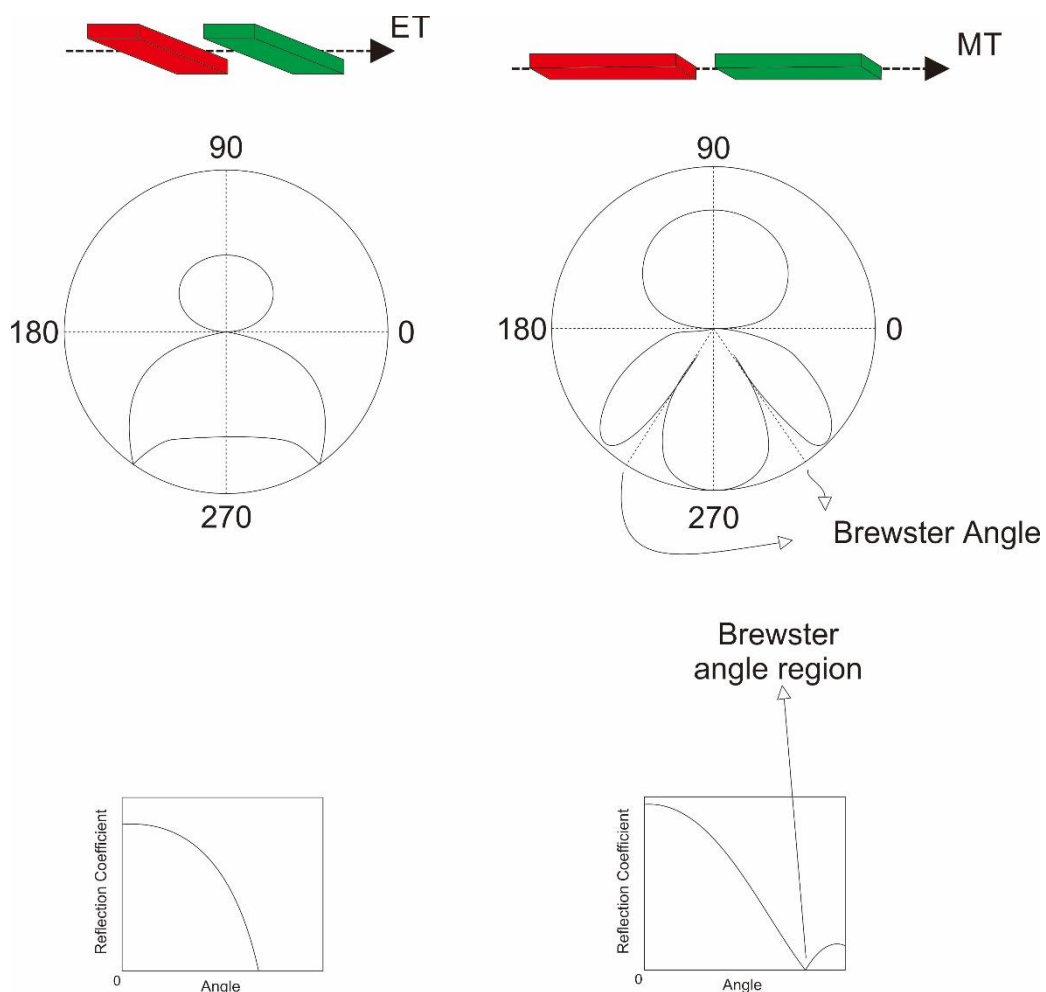


Figure 2.3. Indication of the Brewster Angle in the TE and TM propagation modes, comparing with their respective angle vs. reflection coefficient.

Scattering of light from electromagnetic waves contributes to the visible appearance of most features whereas their visibility is related to the ratio of GPR wavelength to a reflector's radius. Once a feature is visible, Luo et al. (2019) indicated that spatial vertical and horizontal resolution is a concern for a good GPR imaging quality. The horizontal resolution is defined as the capability of a GPR system to distinguish two (2) adjacent targets on the same plane, while vertical resolution describes the GPR system's ability to separate two (2) adjacent features at varying depths. According to Rial et al. (2009), the vertical resolution is a function of the duration of the radar pulse that, in turn, is related to the center frequency of the antenna (i.e., the shorter the pulse duration, the better the resolution will be). The authors pointed out that vertical resolution, $r_{vertical}$, can be calculated from the effective duration of the radar pulse, τ_p , and the wave propagation velocity, v , in the medium according to:

$$r_{vertical} \approx \frac{\tau_p v}{4} = \frac{\tau_p c}{4\sqrt{k}} \quad Eq. 13$$

where c denotes the traveling velocity of a GPR wave in free space, which is a constant of 0.2998 m/ns. Similarly, Pérez-Gracia et al. (2008b), based on Nyquist's sampling equation, suggested that the vertical resolution is considered to be one-quarter of the predominant GPR wavelength, λ , which is determined as follows:

$$\lambda = \frac{v}{f} = \frac{c}{f\sqrt{k}} \quad Eq. 14$$

where λ is the GPR wavelength of the electromagnetic wave, and f is the center frequency of the GPR wave in the particular media.

As Rial et al. (2009) mentioned, the horizontal resolution mainly depends on the number of traces/m, the beam width, the radar cross-section of the reflector, and the depth where the target is located. The number of traces/m is a manageable factor since it is adjusted by the operator before data acquisition. However, the same cannot be said regarding the beam geometry because it depends on the

characteristics of the antenna and the propagation medium. The authors suggested that the beam geometry could be considered as the cone of energy that intersects with the reflector surface, illuminating an area that is known as antenna footprint (i.e., the area which can contain a second target that cannot be uniquely resolved). Hence, the antenna footprint, obtained by using Eq. 15, could be considered as a rough estimation of the horizontal resolution Pérez-Gracia et al. (2008b). The footprint could be determined using the recommendation of Conyers and Goodman (1997):

$$r_{horizontal} \approx r = \frac{\lambda}{4} + \frac{D}{\sqrt{k+1}} \quad Eq. 15$$

where r is the radius of the First Fresnel Zone footprint, D is the antenna to the reflection surface distance as described in Figure 2.4, and k represents the relative dielectric permittivity of the medium.

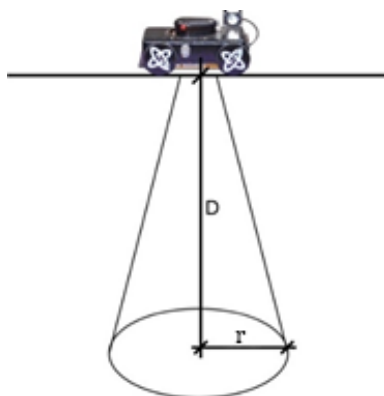


Figure 2.4. The radius of the First Fresnel Zone footprint

2.3 Physical Properties of the Medium

The way in which electromagnetic fields interact with natural materials governs how electromagnetic fields propagate and are attenuated in the middle.

The understanding of constitutive relationships is of great importance to understand the result of investigations using GPR technology because these relationships provide a macroscopic description of how electrons, atoms, and

molecules respond to the application of the electromagnetic field by radar. According to Jol (2009), in most GPR applications variations in dielectric permittivity and electrical conductivity are more important than variations in magnetic permeability.

The electrical conductivity characterizes the movements of the free loads when the material is subjected to an electric field, that is, it is the resistance to the load flow that leads to energy dissipation.

In Eq. 10, it is possible to verify that the attenuation coefficient (α) is proportional to electrical conductivity and magnetic permeability, which explains the fact that the lower the electrical conductivity value of the material, the lower the energy dissipation. Therefore, GPR signal penetration is better in materials with low electrical loss.

Table 2.1 presents values of loss by attenuation (L_a) of some materials, according to Daniels (2007), obtained from Eq. 16.

$$L_a = 8,686 \times 2 \times R \times 2\pi f \sqrt{\left[\frac{\mu_0 \mu_r \epsilon_0 \epsilon_r}{2} (\sqrt{1 + \tan^2 \delta}) - 1 \right]} \text{ Eq. 16}$$

Table 2.1. Loss by wave attenuation in the middle for 500MHz and 1GHz frequency antennas.

Material	Loss with antenna of:	
	100MHz (dBm^{-1})	1GHz (dBm^{-1})
Clay (damp)	5-300	50-3000
Clayey Soil (moist)	1-60	10-600
Sand (Dry)	0,01-2	0,1-20
Ice	0,1-5	1-50
Freshwater	0,1	1
Saltwater	100	1000
Concrete (Dry)	0,5-2,5	5-25
Ceramic Masonry	0,3-2	3-20

Dielectric permittivity characterizes the displacement of restricted loads in the structures of the material submitted to the electric field, which means a displacement of the load resulting in energy storage in the material.

Due to the heterogeneous nature of the materials generally studied in this type of prospecting it is extremely complex to perform quantitative analyses (Jol, 2009). For this reason, as Previatti et al. (2011) suggest, the analyses of GPR data must be accompanied by information ancillary to its interpretation, such as the use of time-domain reflectometry (TDR).

2.4 Principles of Ground Penetrating Radar (GPR) Operation

2.4.1 Acquisition

Acquisitions with the GPR can be made varying some methodological aspects about the positioning of the antennas. They are a) variation of the spacing of the antennas (offset), and b) variation of the position of the antennas (polarization).

Concerning offset, traditional methodologies are (a) common offset prospecting, and (b) multi-offset prospecting. In the first case, the antennas, with fixed geometry (spacing and orientation), perform measurements at regular space intervals. The objective of the application of this methodology is to map reflective subsurfaces. In this case, variations in reflection amplitude and delay time indicate variations in v , α , and Z , i.e., indicate material change.

In the case of the multi-displacement methodology, there is a variation in the distance between the transmitter and receiver antennas. The acquisitions made in this type of investigations can be carried out by keeping one of the antennas in a fixed position and the other varying in position, or by keeping the midpoint between the antennas fixed and varying the position of the antennas to remain equidistant from the midpoint. This latter type of acquisition is called common midpoint research (CMP). These techniques are primarily used to obtain an estimate of the speed of radar signal propagation with depth by a one-dimensional model.

In the issue of polarization, there are five possibilities of positioning the antenna that influences this factor. The antennas vary in the position of one with the

other and also in the position of the two with the direction of the investigation. When the position of one antenna relative to the position of the other, they can be parallel to each other and side by side of each other (BD), parallel to each other and one followed by the other (EF) and perpendicular to each other (XPOL). Concerning the meaning of the investigation, they may be parallel (PL) or perpendicular (PR). The combination of the following possibilities results in the arrangements illustrated by Figure 2.5 and Figure 2.6 shows an example of actual arrangement of antennas within a shielded bow tie antenna.

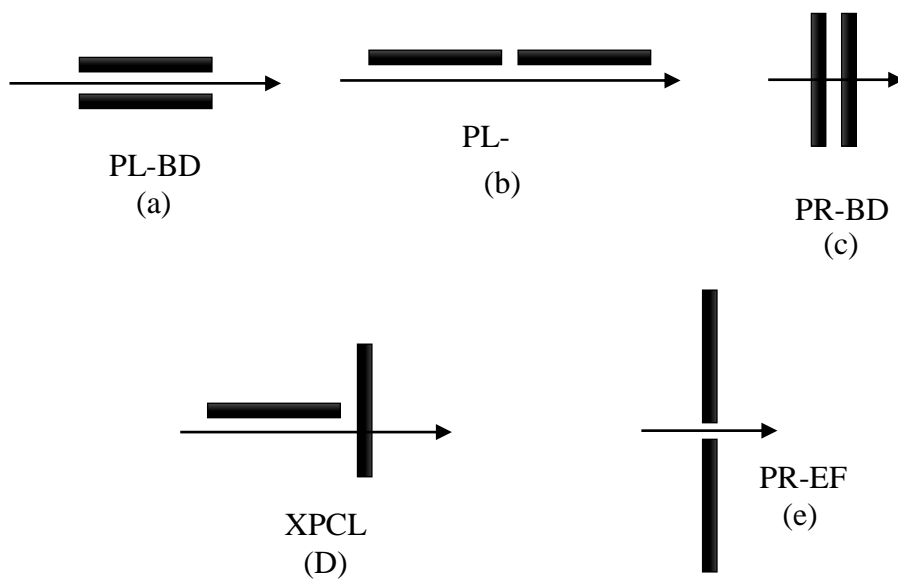


Figure 2.5. Arrangements of antennas that influence polarization (adapted from Annan, 2001).



Figure 2.6. Photography of the transmitting and receiving antennas inside a shielded bow tie antenna and its parallel position.

The positioning of one antenna about the other directly interferes with the distribution of the electromagnetic field seen in item 2.1. If the antennas are arranged with their parallel electric fields (BD), the electromagnetic field distribution is in the Transverse Electric Mode (TE), while the antennas are arranged with their parallel magnetic fields (EF), the distribution of the electromagnetic field is magnetic transverse mode (TM). Figure 2.7 presents the illustration of radargrams of CMP investigations performed with the antennas generating field in Transverse Electric (a) and Magnetic (b), with the presence of attenuation caused by the Brewster angle when using the TM field.

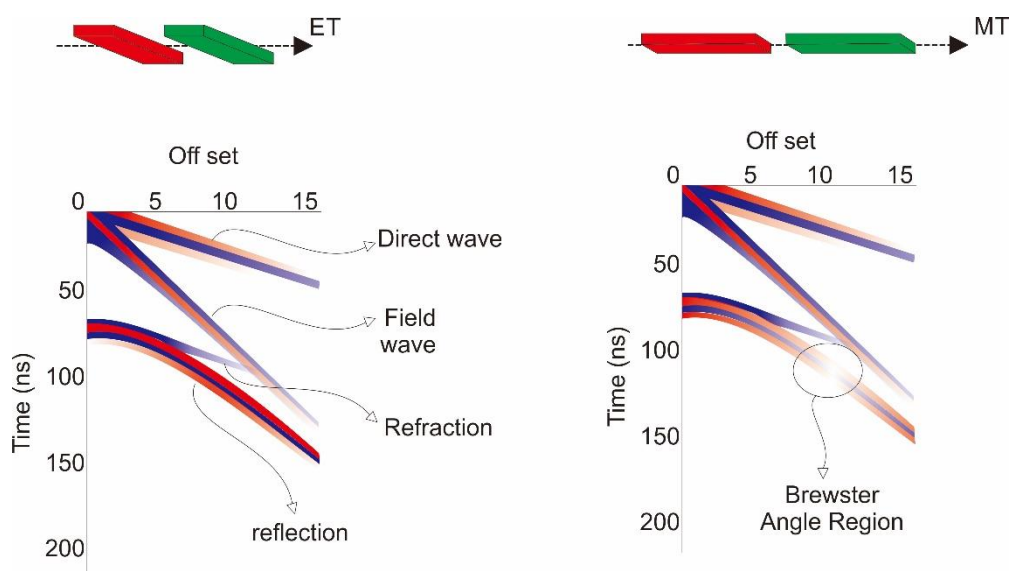


Figure 2.7. Illustration of radargrams of CMP investigations carried out with the antennas generating field in TE (a) and TM (b) (adapted from Jandyr, 2016)

According to Annan (2001), three factors are important when choosing the frequency of operation: desired spatial resolution, limiting disturbances and depth of exploration.

Assuming a central frequency the bandwidth ratio of 1, the restriction in the central frequency (is f_c) calculated as a function of spatial separation (in Δz) meters and the dielectric constant or relative dielectric permittivity (k), according to Eq. 17. Table 2.2 presents typical dielectric constant values for materials commonly found in investigations.

$$f_c > \frac{75}{\Delta z \sqrt{k}} \text{MHz}$$

Eq. 17

Table 2.2. Dielectric constant values for traditional materials

Material	Dielectric constant	Material	Dielectric constant
Ar	1 ¹	Granite	4-6 ¹
Distilled water	80 ¹	Drained granite	5-8 ² 5 ³
Freshwater	80 ¹ 78(25°C)-88 ² 81 ³	Fractured and damp granite	5-15 ²
Saline water	80 ¹ 81-88 ² 81 ³	Drained salt	5-6 ¹
Drained sand	3-5 ¹ 3-6 ² 2-6 ³	Ice	3-4 ¹ 3 ² 4 ³
Wet sand	20-30 ¹ 10-30 ^{2/3}	Frozen sea water	4-8 ^{2/3}
Drained coastal sand	5-10 ²	Solidified snow	6-12 ³
Limestone	4-8 ¹	Permafrost	2-8 ² 4-8 ³
Shale	5-15 ¹	Drained asphalt	2-4 ³
Drained shale	4-9 ³	Wet asphalt	6-12 ³
Saturated shale	6-9 ² 9-16 ³	Drained concrete	4-10 ²
Silt	5-30 ¹	Damp concrete	10-20 ²
Clay	5-40 ¹		
Drained clay	2-20 ²		
Wet clay	15-40 ²		

¹Annan (2001)²Jol (2009)³Daniels (2007)

Table 2.2 shows a range of variation of values. This is due to the presence of diverse values by the cited authors (Annan, 2001; Jol, 2009; Daniels, 2007). There is no clear explanation of how the values were obtained by the authors consulted, but it is imagined that the different values were obtained in materials that were similar but that could present different parameters (e.g., salinity, moisture content, chemical/mineralogical composition).

Another condition to be taken into account when choosing the frequency to be used is the amount of disturbance due to the heterogeneity of the medium to be investigated. Eq. 18 indicates that the frequency must be chosen according to the dimension of the object that leads to heterogeneity (ΔL) and the dielectric constant (k).

$$f_c > \frac{30}{\Delta L \sqrt{k}} \text{MHz} \quad \text{Eq. 18}$$

The third condition defines the frequency as a function of the depth of the target and also of the dielectric constant, as shown in Eq. 19.

$$f_c > \frac{1200\sqrt{k-1}}{D} \text{MHz} \quad \text{Eq. 19}$$

Table 2.3 indicates a relationship between desired depth and typical central frequencies of antennas provided by various manufacturers. The values expressed were based on the practical experience of Annan (2001).

In addition to frequency, it is important to set the time interval (Δt) and sampling space (Δx). For this purpose, Nyquist's sampling theorem is used, whose equations for sampling criteria adapted to a non-ideal system are presented in equations 21 and 22, being f_c expressed in MHz, Δt in ns, and Δx in m.

$$\Delta t \leq \frac{1000}{6f_c} \quad \text{Eq. 20}$$

$$\Delta x \leq \frac{v}{6f_c}$$

Eq. 21

Table 2.3. Central frequency depending on the depth to be investigated

Depth (m)	Central frequency (MHz)
0,5	1000
1,0	500
2,0	200
7,0	100
10,0	50
30,0	25
50,0	10

The antennas used in the investigation can be shielded or unshielded. Shielding increases the efficiency of the system, since a smaller part of the energy disperses in the air, causing the investigation to suffer interference from numerous external agents, as shown in Figure 2.8. Despite the benefits, shielding can promote a wave reverberation. Therefore, armored antennas are more susceptible to the omission of important information due to the reverberation of signals.

It is more common to find shielded antennas of higher frequencies. This is due to the unfavorable size for portability that lower frequency antennas may have.

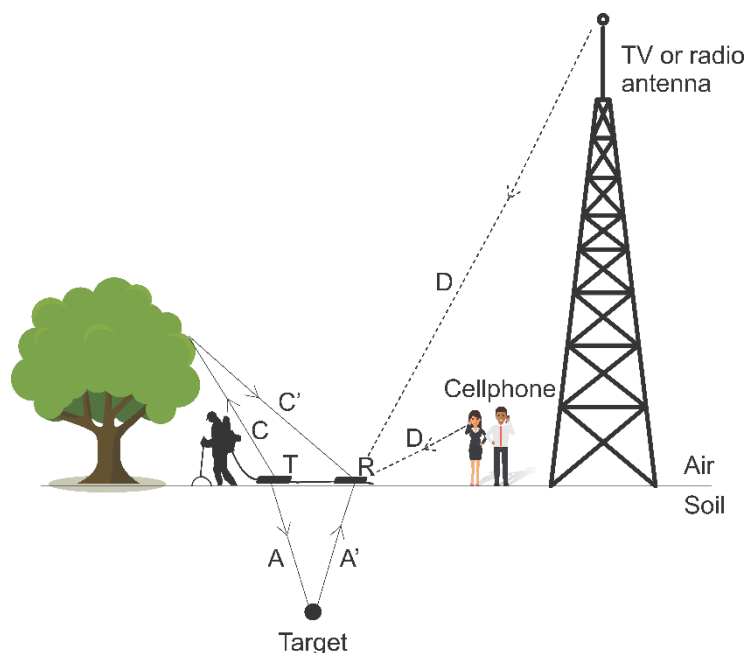


Figure 2.8. External agents that can influence unarmored antennas. (Adapted from Jol, 2009)

2.4.2 Data processing

As good as the contact between the radar antenna and the medium to be investigated, in practice, there will be a space between the antenna and the medium. This interface results from the roughness naturally existing on the surface of the medium. Because of this, there are several ways of propagation of the wave emitted by the transmitter (T) until it reaches the receiver again (R). Figure 2.9 presents the possible ways of wave propagation. A portion of the propagated energy will always pass only through the air until it reaches the receiver as shown in Figure 2.9a and another portion will pass subsurface without reaching the reflector object of interest, as shown in Figure 2.9b. The waves that propagate through the middle, reach the object, and return to the receiver, as shown in Figure 2.9c, 2.9d, 2.9e, and 2.9f will be of greater interest for processing.

Therefore, before knowing the parameters to be analyzed in the processing, it is interesting to understand the formation of the resulting data (i.e., radargrams). Radargrams are composed of a series of strokes that represent the pulses generated at each displacement increment. According to Battista et al. (2009), oscillatory pulses are modulated by the means through which waves propagate. Therefore, each

oscillatory pulse emitted by the transmitter and received by the receiver indicates the condition in which the pulses are reflected in the time domain.

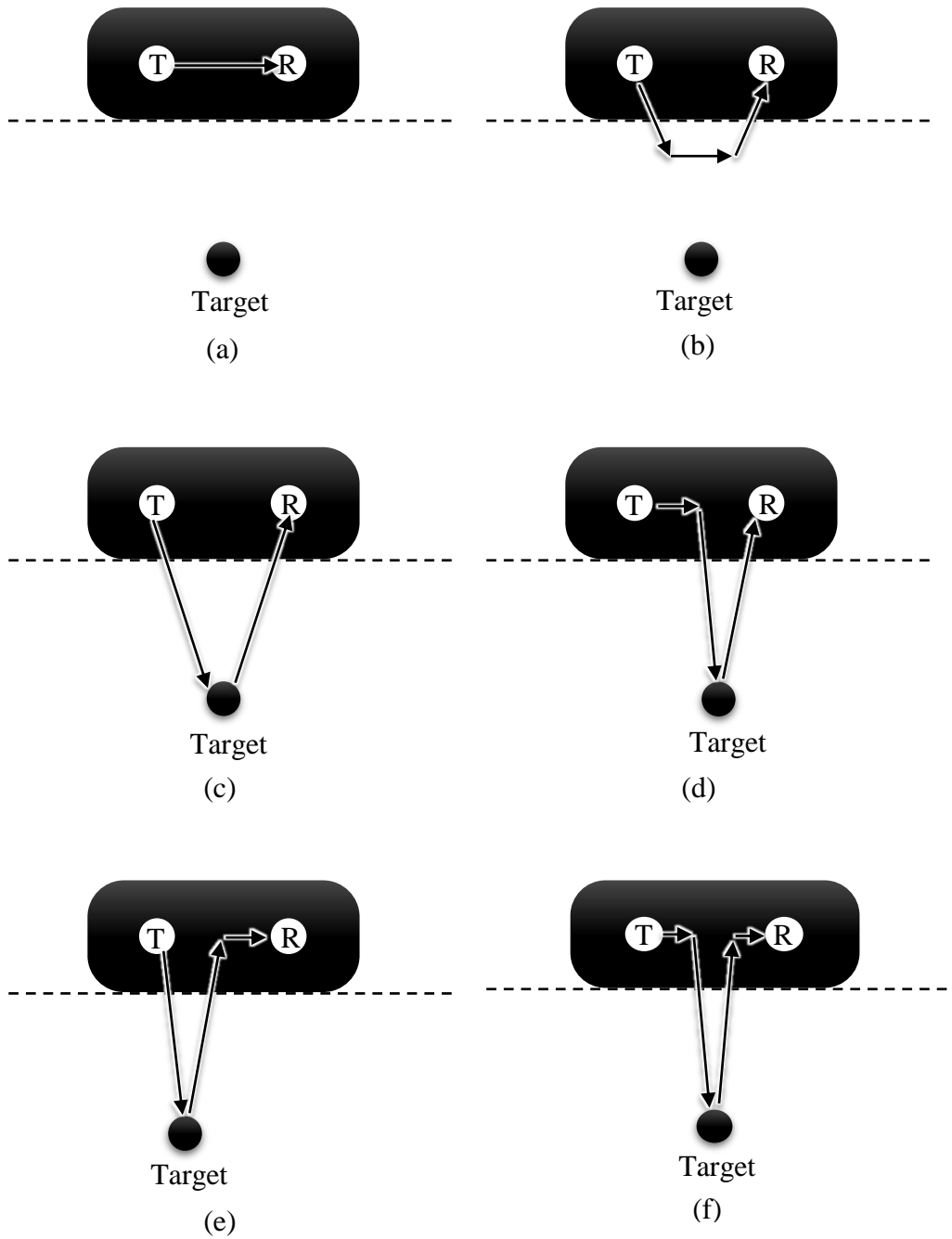


Figure 2.9. Possible ways of propagating the wave until it reaches the receiver (R)

Figure 2.10 presents a typical trace of an ideal, noise-free, unshielded antenna, where B is the wave resulting from the transmission of direct energy, cc' is the wave resulting from the reflection of objects near the antenna, but on the surface of the ground and AA' is the wave resulting from the reflection of the object buried in the ground.

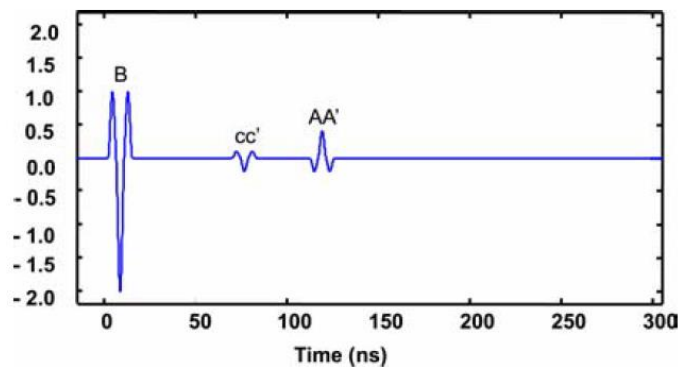


Figure 2.10. Typical trace of an ideal, noise-free, unshielded antenna (Annan, 2003).

The data obtained in the field are affected by the noise and instabilities of the equipment. As a response, the application of GPR should be accompanied by processing that allows the extraction of quantitative data through wave analysis, including speed, attenuation, and impedance.

Data processing consists of four steps in an iterative way: data editing, basic processing, advanced processing and visualization, and interpretation of the data. For this purpose, there are several commercial computational packages such as RadExplorer, Reflexw, Radan and Prism2, as well as software developed from algorithms such as the one presented by Behar et al. (2008).

The first step called data editing encompasses procedures such as data reorganization, data fusion, key or background information refresh, repositioning, and adding elevation information to the data. According to Annan (2003), the central frequency of acquisition is of great importance in this stage of processing.

In the basic processing step, fundamental manipulations are performed so that the data becomes acceptable for an initial interpretation in an iterative manner. For this purpose, traditional filters such as Dewow, Time Gain, Temporal and Spatial

Filter, which are used, respectively, to reduce low-frequency noise, equalize amplitudes that have been attenuated with depth and filter a specific frequency range that is of interest to the investigation.

Szymczyk and Szymczyk (2013) also describe various types of temporal and spatial filters used not only in the basic processing stage but also in advanced processing. Time filters for one-dimensional operations include the simple average filter, median filter, low pass filter, high pass filter. Already among the spatial filters are Simple running average and Average subtraction.

In Figure 2.11 it is possible to observe in a typical radargram after the basic processing step, where you can identify the main characteristics to be analyzed in the later steps.

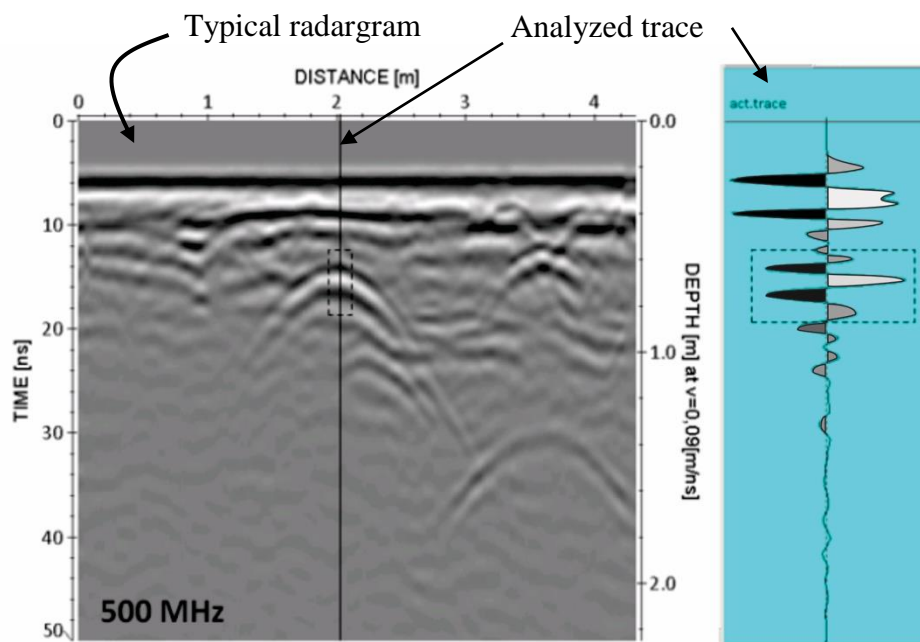


Figure 2.11. Analysis of a trace in the processed radargram (adapted from Rial et al., 2009)

The trace highlighted in the radargram is shown on the right of Figure 2.10. In the radargram, the grayscale colors correspond to the amplitude of the wave illustrated in the stroke, where the white and black colors represent the maximum amplitude in a module and the intermediate grayscales, also in a module. It can be

observed that between 4ns and 7ns is the first reflection present in the radargram. This wave is the result of direct energy transmission, equivalent to the B wave analyzed in Figure 2.10. After the occurrence of the wave formed by direct energy transmission, there is a signal attenuation followed by a further increase in wave amplitude between 14ns and 16ns. In this region, it is now possible to identify the reflection corresponding to the object of interest buried in the soil, equivalent to the wave AA' analyzed in Figure 2.10.

Advanced data processing is the step in which attributes are obtained from the preliminarily processed data. An important attribute to be obtained from radargrams is the velocity of wave propagation because through this data one can identify the type of material of the analyzed medium through its dielectric constant, as observed in Eq. 9.

There are two distinct ways to analyze the velocity along with the depth of the investigation, they are through velocity models obtained from CMPs or through velocity analysis by the hyperbolic velocity analysis method when using the fixed *off-set* investigation method.

According to Tillard and Dubois (1995), only with repetitive acquisitions, as happens in the CMP technique, it is possible to reduce uncertainties about wave propagation velocity. Although this procedure is performed, the author mentions that it is not possible to achieve errors of less than 10% when performing velocity analysis with corrections.

The hyperbolic velocity analysis method is applicable when a fixed off-set investigation is performed, with the presence of diffraction or reflection hyperbola. In these cases, hyperbolic correspondence is performed by combining the velocity of the material with a hyperbolic function formed by the observed data. According to Klemm (2009), the function that is used for the determination of velocity by this method is explained by Eq. 22.

$$v = \sqrt{\frac{x_r^2 t_0 + x_s^2 \Delta t}{t_0 t' \Delta t}} \quad \text{Eq. 22}$$

Where x_r is any position in the investigation above hyperbola, x_s is any position in the investigation that is not positioned above the visualized hyperbole, t' is the response time of the diffraction hyperbole at the point x_r , t_0 is the response time of the diffraction hyperbole crest, Δt is the difference between the times t' and t_0 . Figure 2.12 illustrates each component of Eq. 22.

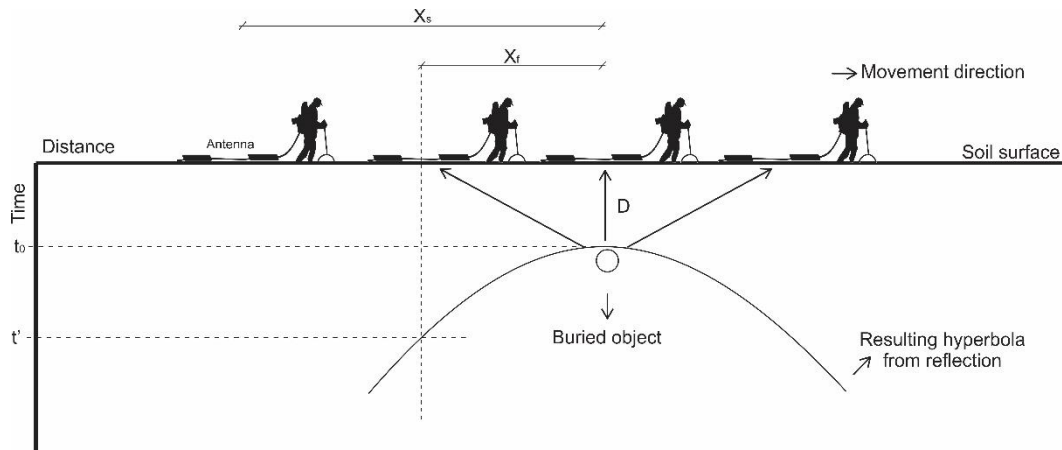


Figure 2.12. Illustration of the meaning of the variables that make up Eq. 22

The degree of saturation of the studied medium has a great influence on the determination of this parameter, therefore, to minimize this type of error, Hamann and Tronicke (2011) proposes the use of CMP to perform the analysis of the velocity spectrum, whose velocity functions are presented in detail by Taner and Koehler (1969).

In the stage of visualization and interpretation of the data, a qualitative analysis of the data is performed, such as the presence of hyperbole. As in the other stages, in this, there are also several types of operations that can be performed to obtain the idealized results. Migration, for example, is extremely used, but according to Annan (2003), it is a type of operation very dependent on the operator's experience.

After all operations, it is possible to identify hyperboles and surface planes. Al Nuamy et al. (2000) and Maas and Schmalzl (2013) propose an automatic pattern recognition methodology for the detection of buried utilities and objects.

2.5 A review of GPR application in concrete imaging

According to Lai et al. (2018), there are three major focus areas when GPR is used in buildings inspections:

1. to locate unseen objects and structures for the sake of heritage conservation and construction compliance check;
2. To map deterioration and to serves as a decision-making tool for preventive/ad-hoc maintenance, and
3. To assess structural damage after natural disasters like flooding, earthquake and landslide.

The authors suggest that GPR is used to evaluate states of cultural heritage buildings as well as modern buildings made of reinforced concrete. In heritage buildings, GPR is useful to evaluate the interface between the old and modern parts of structures built at different periods whereas in modern buildings surveys are focused on:

1. Detection of rebars, pipes, and structural supports;
2. Detection of the geometry of objects embedded in concrete, and
3. Detection of dampness, voids, and cracks of concrete.

For rigid pavements made of concrete, GPR is used to evaluate the thickness and condition of steel rebars, as well as to detect anomalies like cracks and water infiltration. GPR surveys are also carried out on bridges to assess cracks, rebar corrosion, and water leak. Besides those applications, GPR is also used to map rebars, pre-stressed or post-tensioned tendons, and their ducts According to Lai et al. (2018), surveys are carried out either directly from the paved deck or individually on bridge elements like bridge girders, piers or columns. A summary of applications in shown in Table 2.4.

Table 2.4. Examples of application of GPR (adapted from Lai et al., 2018)

References	Antenna frequency	City	Building types	Subject of investigation	3D	Major findings and remarks	
Buildings	Kanli et al. (2015)	400 and 900 MHz	Sopron, Hungary	Fire tower	Voids and cracks before and after cement injection	No	Reflections from the fractured and porous zones are weakened or lost. Cores are available to validate the signal.
	Orlando and Slob (2009)	2 GHz	Chieti, Italy	Historical building	Floor stability affected by a landslide	Yes	Utility, Iron bar and some cracks can be detected from parallel broadside profiles after 3D single component algorithm.
	Xie et al. (2013)				RC structure voids	No	The model is developed to automatically identify voids with high accuracy. Multiple waves caused by steel bars contribute to void positioning.
	Barraca et al. (2016)	500 and 800 MHz, 1.6 GHz	Ihavo, Portugal	Rehabilitation building	Local Geological condition; unknown infrastructure location; removed walls; fracturing investigation	No	GPR is capable of investigating local geological conditions, mapping infrastructure, locating altered elements, as well as understanding changes in construction materials and pathologies and fracturing.
	Rucka et al. (2016)	2 GHz	Gdansk, Poland	Tower of church	Boundary between masonry and reinforced concrete	No	The diffraction-refraction scattering at the boundary are identified with the developed procedure. A series of formulation are derived to describe the refracted hyperbolic diffraction curve. The point of the refraction indicates the boundary between media.
	Ranalli et al. (2004)	600 and 1600 MHz	L'Aquila, Italy	Church	Wall thickness, internal masonry structure and detachments or cracks' locations	No	Wall thickness vary fairly; elongated stones, detachments and cracks in façade and ashlar facing are found. Wall thickness is a significant finding in seismic modelling.

Table 2.4. Examples of application of GPR (adapted from Lai et al., 2018)

References	Antenna frequency	City	Building types	Subject of investigation	3D	Major findings and remarks
Pérez-Gracia et al. (2008c)	500 and 900 MHz	Valencia, Spain	Theatre	Point of contact between before and after modification	No	The velocity obtained in the older part of the theatre are lower than expected because the materials are wet. Sharp variation in wave velocity occurs at the point of contact between different materials
Gonzalez-Drigo et al. (2008)	400 and 900 MHz	Barcelona, Spain	Historical building	Structural strength of the modified columns and load-bearing walls	No	Local weakness of the floor, original power lines and water conduction are detected. Structural elements can be identified by analyzing wave velocities. Reflections of cluttered material around may lead to misinterpretation of the data.
Kilic (2015)	2 GHz	Urla, Turkey	Primary school	Cavities and water ingress hidden within a structure	Yes	Voids, change of materials and pipes are evident in radargram. Integrated approach can detect both visible and hidden structural condition.
Kim et al. (2014)	1200 MHz	Korea	Prototype containment building	Concrete structure	No	Reliable images corresponding to the reinforced steel bars and defects such as void, but void and metal sheath pipes beneath the reinforcing steel bars could not be detected by GPR because of electromagnetic shielding. Pre-test helps in select best array of antenna concerning polarization.
Barrile and Pucinotti (2005)	1600 MHz		Civil building	Location of steel reinforcement.	No	Steel bars are located. Radar wave would be sharply reflected at the interface between rebar and concrete.

Table 2.4. Examples of application of GPR (adapted from Lai et al., 2018)

References	Antenna frequency	City	Building types	Subject of investigation	3D	Major findings and remarks	
Buildings	Anderson et al. (2010)	1500 MHz		Roof of School, Concrete floor of an apartment,	Pattern, Placement and Density of Rebar, Locating Pre-tensioned Tendons	No	They presented different applications in different case studies. The cases of interest are related to characterization of a roof (Rebar spacing and thickness) and a floor constructed with pre-tensioned tendons in order to locate the tendons.
	Cassidy et al. (2011)	900 MHz	University of Leicester	Concrete slab	Void detection	Yes	Void detection comparing GPR and ultrasound system.
	Chang et al. (2009)	1 GHz	Chung Hua University	Concrete test specimens	Reinforcing steel bar diameters	No	Development of a methodology to define the dielectric coefficient in concrete using digital image processing and a methodology that allows reinforcing steel of radii to be quantitatively detected through GPR radargram,
	Hong et al. (2014)	2.6 GHz		Reinforced concrete slab specimen	Rebar corrosion monitoring	Yes	They proposed GPR's attribute analysis for mapping reinforcement corrosion from energy and chloride distribution from peak frequency.
Road pavements	Varela-Gonzalez et al. (2014)	2 GHz		Concrete pavement	Pavement thickness	No	A developed semi-automatic program. Capability of processing large data at a time can led to faster diagnostics.
	Stryk et al. (2013)	1.6 GHz, 2.6 GHz		Concrete pavement	Dowel and tie bar position	No	Accuracy reaches 1 cm in terms of rebar location; the horizontal direction is influenced by the distance of dowels and tie bars in between themselves. Vertical distance depends on velocity measurements in such materials.

Table 2.4. Examples of application of GPR (adapted from Lai et al., 2018)

References	Antenna frequency	City	Building types	Subject of investigation	3D	Major findings and remarks
Li et al. (2016)	1.5 GHz		Reinforced concrete pavement	Pavement thickness and air voids	No	A shorter wavelength range is proposed in dynamic models and P-wave velocity when estimate the thickness. Air voids can affect the estimation of wave velocity. The impact echo methods is proved to be accurate in estimating the thickness of concrete pavements.
Leng and Al-Qadi (2014)	2 GHz		Pavement	Dielectric constant and thickness	No	The extended common mid point (CMP) is developed, but its performance of is not as good as surface reflection, because of the sampling rate limitation and the possible overlap of GPR signal reflection. Higher sampling rate may result in better accuracy in CMP measurement.
Xu et al. (2014)	200 and 400 MHz	Beijing, China	highway	Roadbed damage	No	The developed novel 60 channel GPR joints positioning with video system, improves survey efficiency. Loose roadbed is indicated by the clutter and layer discontinuities.
Sun et al. (2017)	0.5–6.5 GHz: 0.1 GHz step		highway	Roadway structure evaluation	No	Interface roughness is estimated by using Maximum Likelihood Method for time delay. When rough road surface is investigated, the scattering mode can be taken into consideration.
Lorenzo et al. (2011)	500, 800 and 1000 MHz		highway	Roadbed survey	No	With non-metallic chassis and rolling elements, the interference in the GPR signal form elements are minimized.
Pitonak and Filipovsky (2016)	2 GHz and 400 MHz	Ziarnad Hronom, Slovakia	motorway	Layer thickness and pavement roughness	No	The GPR results show that ¼ layers are built by more than 10% thinner than designed structure. The antenna survey speed should be reduced for the sake of a closer contact to the surface of pavement.

Table 2.4. Examples of application of GPR (adapted from Lai et al., 2018)

References	Antenna frequency	City	Building types	Subject of investigation	3D	Major findings and remarks
Hugenschmidt (2002)	1.5 GHz	San Bernardino road, Zurich, Switzerland and Graubunden, Switzerland, Uri, Switzerland	Concrete bridges and motorways	Pavement thickness, rebar position, rebar coverage	No	Three study cases are presented. They show the condition of structures as well some specificities.
Alani et al. (2013)	2 GHz	Edinburgh and Kent, England	Road bridge	Damage rebar and moisture ingress	Yes	Two similar cases are tested. Higher signal attenuation indicates deteriorated area; presence of moisture may be mistaken as subsidence. When surveying bridge, yielding a significant quantity of data is important.
Varnavina et al. (2015)	1.5 GHz		Concrete bridge	The process of deterioration of surface concrete	No	A linear relation between GPR data and depth is established. The map of reinforcing steel, different weather conditions caused varying linear slope and intercepts. GPR data are based on the reflection amplitudes from the top transverse layer of reinforcement and do not present the condition below.
Kosno et al. (2016)	900 MHz		Bridge deck	Flexible soil-steel structure testing	No	Improper backfill drainage and a lower degree of compaction are detected. GPR can be used as an efficient tool for final inspection and identification of poor workmanship.

Table 2.4. Examples of application of GPR (adapted from Lai et al., 2018)

References	Antenna frequency	City	Building types	Subject of investigation	3D	Major findings and remarks
Benedetto (2013)	2 GHz		Concrete bridges	Tracking cracks, corrosion associated with reinforcing bars.	Yes	A new algorithm is presented in automatic tracking cracks in the bridge decks. It features at capacity of following the exact geometry of the crack in 3D space. 3D imaging is applied to detect voids, cracks or buried objects. And numerical approach indicates the noneligible increase of the signal amplitude produced by defects.
Hugenschmidt and Mastrangelo (2006)	1.2 GHz		Bridge planned to demolition	Inspection of concrete bridges	Yes	EMPA approach are carried out and gap in the resultvfor the problems in sectionsare caused by resolution problems and interpretation uncertainties. 3D inspection provides a detail insight into concrete structures. No deeper rebar was found by the mobile acquisition unit.
Solla et al. (2016)	500 MHz	Lubian, Spain	Historical bridges	Evaluation of a bridge suffered different restorations	No	The developed integrated modelling that combines photogrammetry, thermography and FDTD algorithms demonstrates the capabilities of the effective interpretational tool.
Hasan and Yazdani (2014)	1.6 GHz and 2.6 MHz	Roanoke, US	Concrete bridge	Explore inadequate concrete covers	No	Wider and blurry hyperbola shape might indicate the area with more water content. It may not be true to assume that the dielectric constant is uniform in a newly placed concrete.
Kosno et al. (2016)	2 GHz	Trynka river, Grudziadz, Poland	Pre-tensioned Concrete Bridge Beams and precast girders	Rebar location and cover depths and post-tensioning cable trajectories and 'T' bridge girders	No	The rebar location, cover depths, pre-tensioning and post-tensioning cable trajectories are measured. GPR is proven as a good quality control method.

Table 2.4. Examples of application of GPR (adapted from Lai et al., 2018)

References	Antenna frequency	City	Building types	Subject of investigation	3D	Major findings and remarks	
Tunnel liners	Lalagüe et al. (2016)	400 MHz; 1.5, 2.6, 1 and 2 GHz; 100 MHz–3 GHz	Vestfold, Norway	Cave-in penetrated the concrete lining	Void behind the inner lining; rockfall from the tunnel roof	Yes	The Step frequency GPR is suitable for measuring distance between inside and rock surface. Ground-coupled GPR is the best for detecting loose rocks. Tunnel liner should be scanned immediately after tunnel construction.
	Lopez-Rodríguez et al. (2016)	100 MHz	Teotihuacan, Mexico	Tunnel beneath the temple	Archeological subsurface strata	No	Multi-cross wavelet (MCM) reflects the mixed limestone and clay compound; while Fourier multi-cross function (FMC) analysis suggests tunnel and chamber are filled with similar materials. Applying FMC and MCW algorithm helps determine the similarities of the tunnel and chamber filling periods
	Zhang et al. (2010)	250 and 500 MHz; 1 GHz	Shanghai, China	Metro line	Grout thickness behind the lining segments	No	500 MHz is the most suitable frequency. The result can be improved if the dielectric constant of the grout at exact dates corresponding to the field test are measured. Predetermination of travel time through the line segments and dielectric parameters contribute to accurate measurement.
	Hugenschmidt and Kalogeropoulos (2009)	400, 900 and 1500 MHz	Geneva, Switzerland	motorway	Retaining wall	Yes	The use of 400 MHz GPR does not penetrate deeper because of the abundance of rebar; the fusion of datasets obtained from different orientations reduce the directionality of radar data. It is not possible to decide whether the anomalous reflectors are related to rock anchors or not, based on radar data alone.

Table 2.4. Examples of application of GPR (adapted from Lai et al., 2018)

References	Antenna frequency	City	Building types	Subject of investigation	3D	Major findings and remarks	
Tunnel liners	Li et al. (2011)	900 MHz	Long Hai Tunnel, China	tunnel	Liner thickness	No	Lining interfaces are automatically identified by peak value criterion method. Compared to artificial recognition, automatic recognition offers coarseness of lining layer.
	Yu et al. (2016)	800 MHz	Nanchang, China	Metro	Grouting layer thickness; presence and distribution of any damage	No	Thickness is measured 30 cm; damages like low density, voids, crack and fissure were observed. Comparison of the field data with the models makes an accurate interpretation.
	Xiang et al. (2013)	500 MHz	Fujian, China	highway	Locate rebar; estimate lining thickness and damage	No	found; hyperbolic reflection indicates voids and cracks. 2D-FDTD simulation and symmetry-based algorithm locates true rebar positions.
	Li et al. (2010)	31–36 MHz	Qiyunshan, Jinping and Qingdao, China	Tunnel	Water inrush prediction; groundwater in fractures;	Yes	The developed prediction system combines tunnel seismic prediction (TSP), GPR and transient electromagnetic method (TEM). Faults and fractures can be predicted by combining seismic and radar method; while groundwater predicted by combining radar and transient electromagnetic methods.

3 Study into the effect of steel fiber distribution on the tensile strength of reinforced self-consolidating concrete using the GPR

The American Concrete Institute Committee 309 defines self-consolidating concrete as “a concrete that, without the influence of additional consolidation energy, flows and fills the spaces between the reinforcement and the formwork only under the influence of its mass” (ACI Committee 309, 2005). According to Cattaneo et al. (2012), this material is characterized by possessing a higher volume of fines, the addition of chemical admixture, a limited amount of coarse aggregate, and reduced size of the aggregates when compared to ordinary concrete.

The reduction of concrete fragility under tensile stress could be accomplished by the addition of fibers to the mixture as suggested by da Silva et al. (2020). In fact, the addition of fibers as reinforcement in concrete may not change its compressive strength and modulus of elasticity, but some of its properties such as fracture toughness, ductility, permeability, durability and crack-width control are improved (Monteiro et al., 2018; Zhang et al., 2018). In accordance to Gettu et al. (2005), the contribution of fibers to fracture toughness depends on their distribution within the concrete mass (i.e., especially the orientation of the fibers concerning the crack and the uniformity of their distribution), and preferential orientation of the fibers can be more beneficial in controlling cracks in certain structural elements than an isotropic distribution. Zhang et al. (2018) suggested that fiber reinforcement in concrete is compromised when fibers are not uniformly distributed or distributed perpendicular to the tensile stress direction.

The distribution of steel fiber within a reinforced self-consolidating concrete is essential to study its behavior (Zhang et al, 2020). According to Zhang et al. (2018), destructive and non-destructive methods could be carried out to attain this objective. A summary of different test methods is shown in Table 3.1. The authors indicate that destructive tests rely on counting the numbers of fibers on cross-

sections of specimens, either manually or through imaging processing, and performing manual statistical analysis. Despite being simple and direct, destructive methods are rather time-consuming. The main non-destructive test methods currently employed include: X-Ray Computed Tomography (X-CT), Alternating Current Impedance Spectroscopy (AC-IS), C-shaped ferrite core method, Open-Ended Coaxial Probe measurement, and Inductive method (Zhang et al, 2020).

The present chapter focuses on the steel fiber distribution in self-consolidating concrete short beams used in several standard test methods for determining mechanical properties. The objective is to assess the feasibility of the ground penetrating radar (GPR) in evaluating the homogeneity of fibers within the specimen, for use in testing laboratories to study the modes of placing and compaction employed for preparing specimens during quality control or material development. GPR is a non-invasive geophysical method based on the propagation of electromagnetic waves in the microwave band of the radio spectrum. According to Annan (2009), the GPR principle is similar to seismic reflection. The difference arises from the fact the energy may be reflected at boundaries where subsurface electrical properties change rather than subsurface mechanical properties as it occurs with acoustic energy. GPR is a time-domain system that applies an impulse to the antenna, placed close to the air-concrete interface, that creates and detects key electromagnetic fields. According to Annan (op. cit.), the GPR transmitter antenna translates the excitation voltage into a predictable temporal and spatial distributed field and the receiving antenna detects the temporal variation of a vector component of the electromagnetic field (EM) field and translate it into a recordable signal. During a survey, a GPR transmitter emits through an antenna an electromagnetic pulse source into the concrete. When this pulse encounters a boundary between materials having different dielectric permittivity, it will be partially reflected or refracted back to the surface where a receiving antenna records the magnitude and arrival time of the turned pulse. In the case of the present work, a shield is used to focus or direct EM signal through the short beam minimizing: a) the direct transmitter to receiver energy, b) the energy that escapes into the air, and c) electromagnetic noise in the laboratory environment.

Table 3.1. Summary of different fiber distribution test method

Test Method	Applicable fibre	Fiber diameter	Dispersion	Orientation	Test type	References
Manual Statistic	Unlimited	>0.2mm	yes	yes	DT	Gettu et al. (2005), Shuhua et al. (2013), Vandewalle et al. (2008)
X-CT	SF	>0.1mm	yes	yes	NDT	Shen et al. (2004), Krause et al. (2010), Bordelon and Roesler (2014), Herrmann et al. (2016), Pastorelli and Herrmann (2016)
AC – impedance spectroscopy	CF	Unlimited	yes	no	NDT	Woo et al. (2005), Ozyurt et al. (2006a), Ozyurt et al. (2006b), Faifer et al. (2009), Mason et al (2002), Wansom et al. (2006)
C-type ferromagnetic probe method	CF	Unlimited	yes	yes	NDT	Faifer et al. (2011), Faifer et al. (2012), Ferrara et al. (2012)
Open Coaxial probe measurement	CF	Unlimited	yes	no	NDT	Van Damme et al. (2004), Torrents et al. (2009)
Resistivity test	CF	Unlimited	yes	yes	NDT	Lataste et al. (2008), Barnett et al. (2009)
Inductive method	CF	Unlimited	yes	yes	NDT	Torrents et al. (2012), Cavalaro et al. (2014), Cavalaro et al. (2015)
Image processing	SF	>0.2mm	yes	yes	DT	Liu et al (2011), Liu and Sun (2012), Soroushian and Lee (1990), Lee et al. (2002), Zag et al. (2001)

CF: Conductive fibres; SF: Steel fibres; DT: destructive technique; NDT: Non-destructive technique

3.1 Experimental program

The project was undertaken following the flowchart presented in Figure 3.1. A GPR survey was performed on self-consolidating cured casted short beams just before a monotonic four-point test was carried out. After failure, a representative short beam was cut and the resulting slices were photographed to obtain the position and distribution of the steel fibers. Results were processed using dedicated software and an integrated analysis was accomplished.

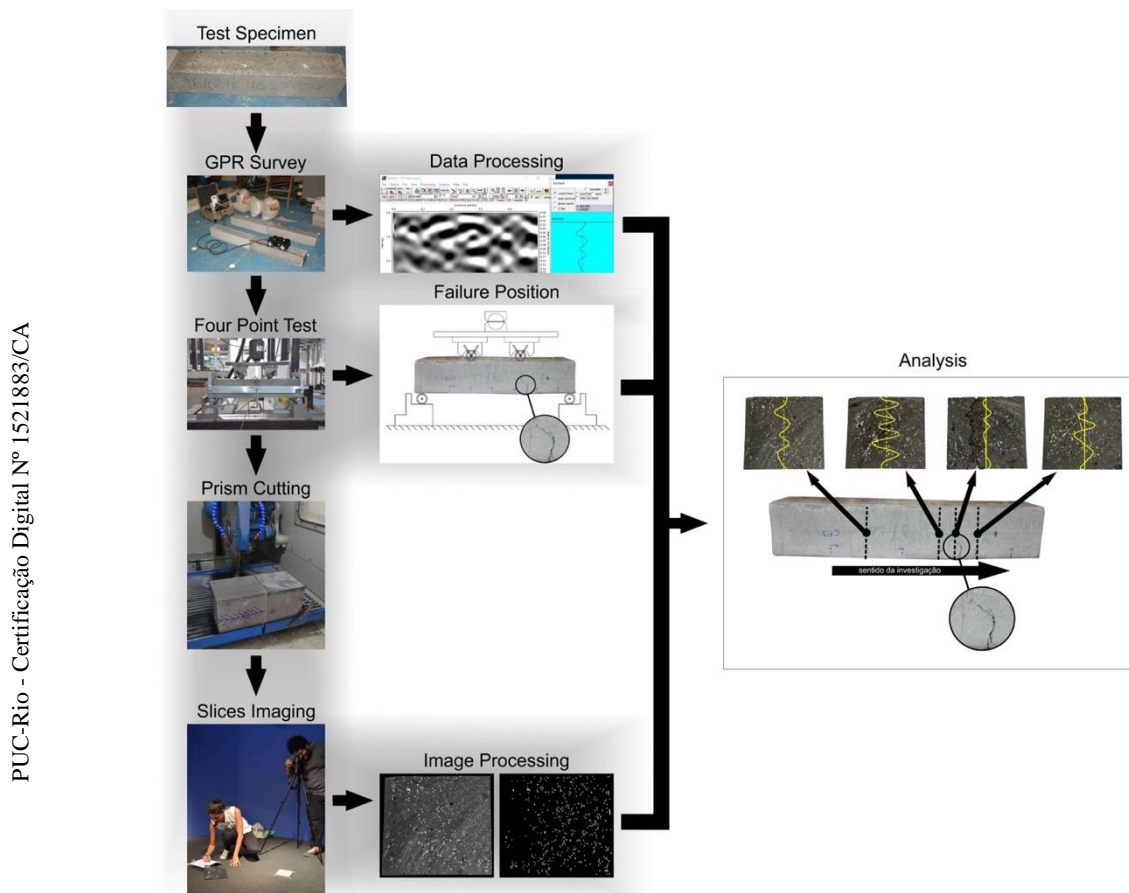


Figure 3.1. Experimental program flowchart

3.1.1 Short beam

Short beams were produced with a cross-section of 150 mm x 150 mm and a 750 mm length as Figure 3.2 shows. The cementitious materials used in the production of the self-consolidating concrete were the Brazilian cement type CPV (ASTM Cement type III), fly ash, and silica fume. Two classes of particle size of

river sand were mixed with the rest of the materials: one ranging from 0.15 mm to 4.8 mm (S1) and the other ranging from 0.15 mm to 0.85 mm (S2). Coarse aggregate with a maximum diameter of 9.5 mm, silica flour (ground quartz), and superplasticizer (Glenium 51) were also mixed with the other materials. The water/cement ratio of the mix was 0.5. The average compressive strength after 28 days was 73 MPa and the obtained slump spreading was 750 mm. For more information on the mixing procedure and matrix mechanical behavior refer to Pereira (2017).



Figure 3.2. Short beams used in the experimental program

To evaluate steel fiber distribution in self-consolidating concrete short beams, three different mixtures were produced. The first one associated with the matrix without fibers and two mixtures with steel fiber volume fractions of 0.50% (40 kg/m³) and 1.00% (80 kg/m³) and named, respectively, as C 0.50%SF and C 1.00%SF. The same fiber volume fractions were used both for SF1 and SF2. The amount of water, sand, cement and the other supplies for the three mixtures is presented in Table 3.2. Steel fibers with hooked ends, a length of 60 mm and an aspect ratio of 80 ($d = 0.75$ mm) were used as reinforcement.

The mixing procedure was carried out through five main stages. First, all the aggregates (sands S1, S2, and coarse aggregate) were mixed with 70% of the water for 1 min with the aid of a previously wet concrete mixer. Soon after, all additives (i.e., silica fume, fly ash and silica flour) were also added to the mix and blended for 1 min. Afterward, the total amount of cement was added and mixed for another minute. The remaining water and all the superplasticizer were then blended with

the rest of the materials for 10 min. Finally, the total amount of fibers was mixed for another 5 min. The specimens were cured for 28 days at room temperature of 24.4° C and 65.7% of humidity before testing.

Table 3.2. Mix composition of the matrix and the steel fiber self-consolidating concrete

Constituent	Mixtures		
	Matrix	C 0.50% SF	C 1.00% SF
Coarse aggregate (G) (kg/m ³)	492.04	478.54	465.04
Sand (S1) (kg/m ³)	826.71	826.71	826.71
Sand (S2) (kg/m ³)	99.60	99.60	99.60
Silica Mesh 325 (SM) (kg/m ³)	70	70	70
Cement (C) (kg/m ³)	360	360	360
Fly Ash (FA) (kg/m ³)	168	168	168
Silica Fume (SF) (kg/m ³)	45	45	45
Superplasticizer (SP) (%)	6.0%	6.0%	6.0%
Water (W) (kg/m ³)	155.65	155.65	155.65
Hooked end fiber (kg/m ³)	0	40	80
Water/Cement ratio	0.50	0.50	0.50

*Sand (S2): Sand (S1) with a diameter of less than 0.85 mm.

3.1.2 GPR survey

Data were acquired on short beams positioned on a reinforced concrete slab along a horizontal line as Figure 3.3 shows. The equipment used consisted of a MALÅ CX ground penetrating radar (GPR) concrete scanning system with a shielded 1.2 GHz center frequency. According to Pérez-Gracia et al. (2009), the shielded 1.2 GHz is a wideband frequency antenna, with bandwidth on the order of its nominal center frequency.



Figure 3.3. GPR concrete scanning system

The acquisition parameters can be summarized as follows:

- Trace length: 8.44 ns;
- Samples per trace: 313;
- Traces per meter: 260;
- Transmitter–receiver offset: 0.079 m, and
- Data processing during acquisition: none.

The relative dielectric permittivity, k , of each media was determined following the procedure suggested by Beneddeto and Tosti (2017). In this procedure, shown in Figure 3.4, a metal plate larger than the GPR antenna footprint is placed underneath the short beam and a comparison of the depth reading in nanoseconds can then be made with the depth reading in centimeters deriving the traveling velocity of the GPR wave in the particular media, following Eq. 9: The relative dielectric permittivity, k , is then determined following Eq. 9.

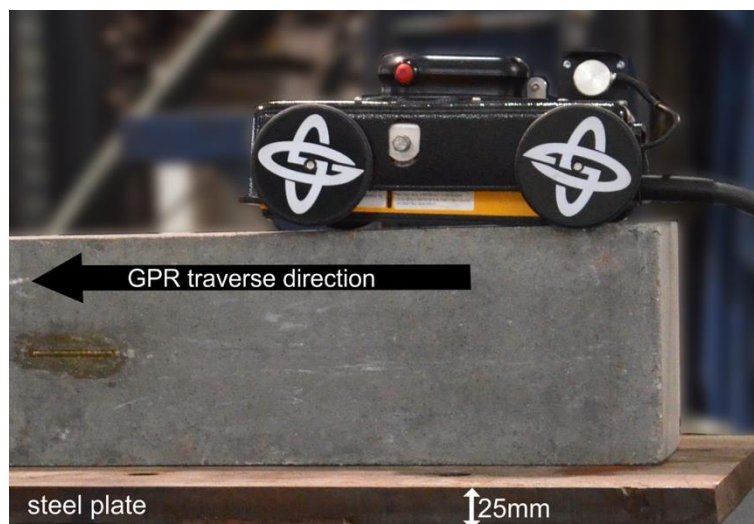


Figure 3.4. Relative dielectric permittivity determination procedure

The authors followed the data processing recommendations given by Bennedeto et al. (2017). In particular, data processing was carried out using REFLEXW software version 9.0 (Sandmeier, 2019) with the following processing sequence:

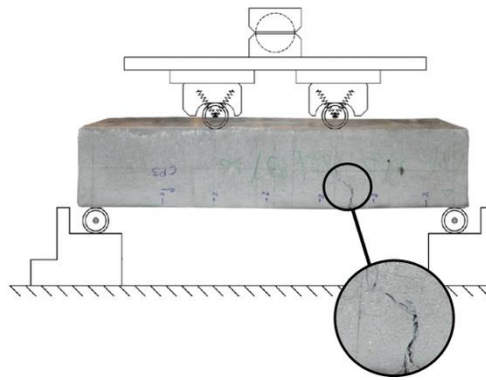
- subtract-mean (dewow);
- correction of surface reflection / direct wave to time zero;
- manual gain, and
- background removal.

3.1.3 Monotonic four-point test

Four-point bending tests were carried on using an MTS servo-controlled hydraulic testing machine with a closed-loop type of control and a load cell of 100 KN. Figure 3.5 shows the test set up.



Figure 3.5. The four-point test set up



Tests were controlled by the CMOD (Crack Mouth Opening Displacement) at a constant rate of 0.10 mm/min using a clip-gauge and limited to 4 mm opening. Figure 3.5 shows that the short beam was positioned with the face where the GPR survey took place in the front (noticed by the blue ink rule marks) so that the resulting crack is formed on the same face as the GPR survey took place.

3.1.4 Shot beam cutting

A reinforced concrete short beam with 1% steel fiber, CP3, was cut to obtain twenty-four 1cm thick slices. The process was carried out by using a lab saw, shown in Figure 3.6, which delivered an even and smooth cut.



Figure 3.6. Specimen lab saw

3.1.5 Slice imaging

Digital images from the concrete slices were taken using a Nikon D7100 camera at the photographic studio of the Department of Journalism as Figure 3.7 shows. Binary images were obtained using the software Adobe Photoshop CS6. The resulting images were then registered and segmented using Fiji, an open-source image processing package. The processed data was mapped, modeled and analyzed through Surfer software. During the process, the nearest-neighbor interpolation algorithm was used to assess fiber distribution.



Figure 3.7. Slice imaging

3.2 Results and discussions

It is very hard to interpret a GPR radargram of shotcrete containing steel fibers as Figure 3.8 demonstrates. This Figure shows the results of the determination of the average traveling velocity of the GPR wave in concrete short beams containing 0%, 0.5%, and 1% steel fiber. GPR data are displayed in either greyscale radargrams and wiggle mode showing the traces amplitude according to their acquisition position.

It is relatively easy to detect the reflector corresponding to the 25 mm steel plate shown in Figure 3.4 in the radargram correspondent to the concrete short beam

containing 0% steel fiber reinforced. The surface indicated by the red arrows was used to calculate the traveling velocity of the GPR wave as 0.0275 m/ns.

On the other hand, the reflector corresponding to the 25 mm steel plate is not perceived on the short beams containing 0.5% and 1% steel fiber as Figure 3.8 shows.

To understand the data, one has to carry out interpretative analysis on the values of the amplitude of several traces acquired during the GPR survey to understand the effect of random wave scattering. Based on these, it was established that the red arrows represent each reflector on the radargrams corresponding to the 25 mm steel plate bellow to the short beams reinforced with 0.5% and 1% of steel fibers. The surfaces indicated by the red arrows were used to calculate the average traveling velocities of the GPR wave as 0.0195 m/ns and 0.0160 m/ns for 0.5% and 1% of steel fibers short beams respectively. Further to these, the results are shown in Figure 8 also suggest that the distribution of fibers varies within the short beams reinforced with steel fibers.

Figure 3.9 shows that the fiber distribution within the concrete short beam CP3, a 1% steel fiber reinforced, in four slices. The position of each representative slice, as well as their digital and processed images, are also shown. These slices were considered representatives, since the GPR survey carried out on this short beam, showed different reflection patterns on the regions where these slices were cut.

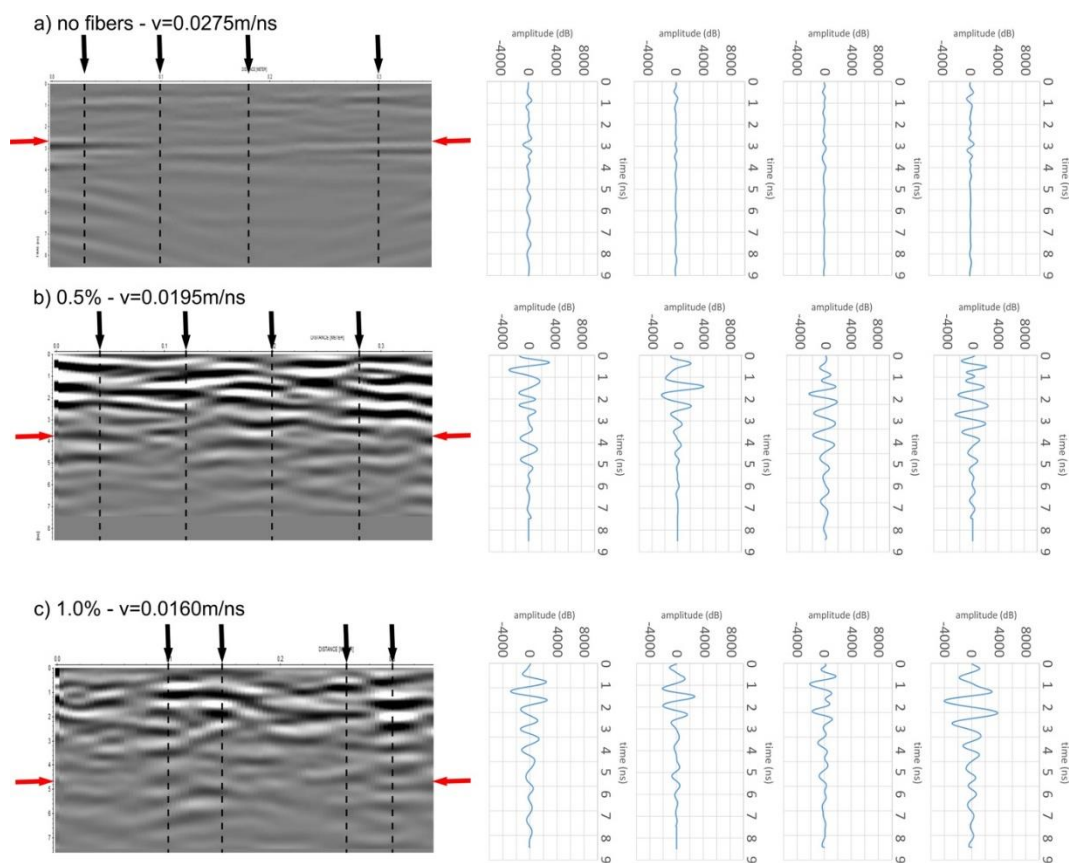


Figure 3.8. GPR data from the determination of the average traveling velocity of the GPR wave in concrete short beams containing 0%, 0.5% and 1% steel fiber

Images from the four slices show that fibers are not evenly distributed in the short beam. Besides, Figure 3.9 shows a wide variation of fiber density in each slice. As shown in Table 3.2, there is a disparity in the numbers of fibers in each slice. For instance, there are 90.8% more fibers in slice 12 than in slice 41. The statistical analysis also shows that distance between fibers also varies within the short beam. Results presented in Table 3.3 indicate that fibers form clusters with the distance between fibers close to 1 mm throughout the short beam but, in some instances, large voids are also formed as can be seen in Figure 3.9.

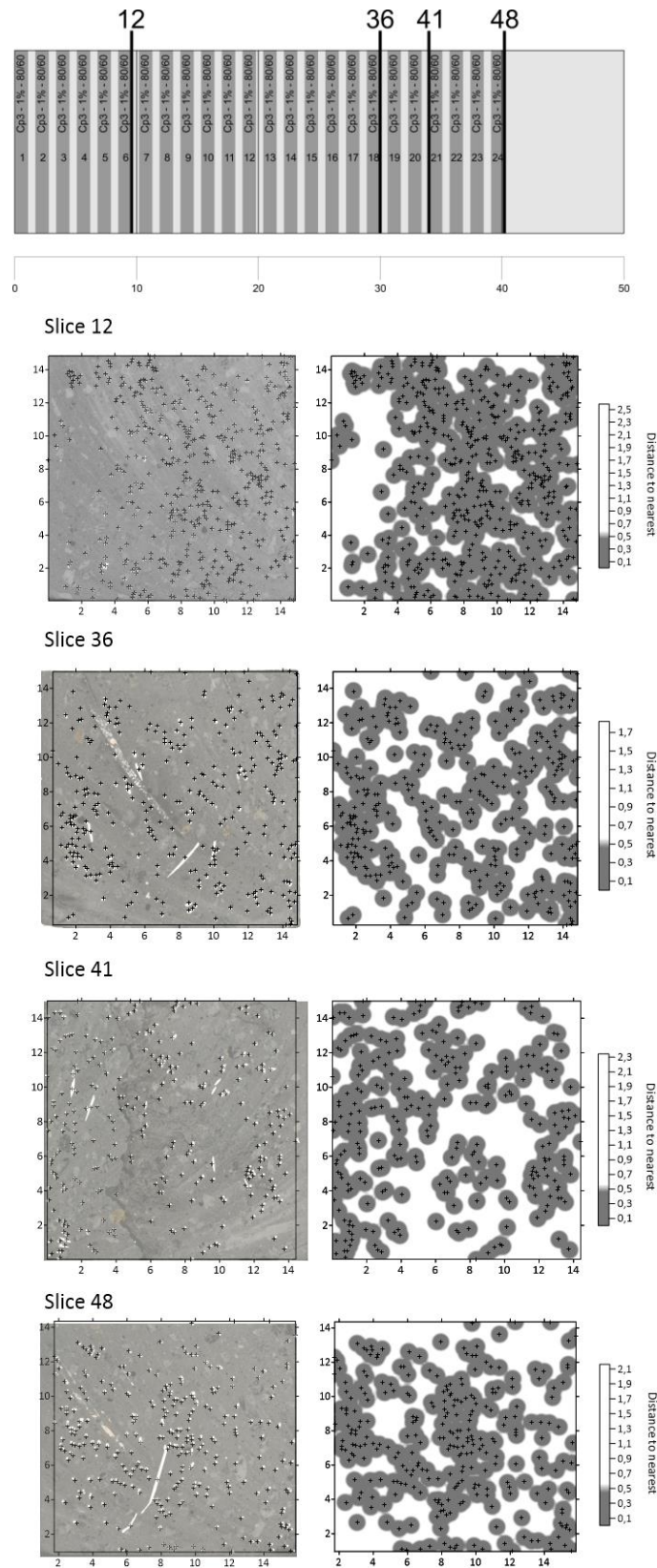


Figure 3.9. Fiber distribution within a 1% fiber reinforced concrete short beam

Table 3.3. Statistical Analysis on the fiber distribution within the 1% fiber reinforced short beam

	Slice #12	Slice #36	Slice #41	Slice #48
Number of fibers:	500	328	262	281
Distance to the nearest fiber (cm)				
Minimum:	0.11	0.11	0.14	0.12
Maximum:	1.39	1.99	1.29	1.54
Mean:	0.30	0.37	0.41	0.39
Median:	0.23	0.30	0.35	0.31
Standard Deviation:	0.18	0.24	0.23	0.24

These voids could generate weakness in fiber reinforcement. In this particular beam, a crack was formed as a result of the four-point test on the position where slice #41 was obtained. As Table 3.3 shows this slice presents the least numbers of fibers and the highest average distance between fibers. Figure 3.9 also indicates that a crack scar was formed in the region where there was a large distance between fibers.

When sketches of the emitted and recorded GPR signal in a single radar trace mode are compared to the digital and processed images of each of the four slices images, as Figure 3.10 shows, it is possible to perceive a good relationship between the GPR signal and the distribution of steel fibers within the short beam. The A-scan, illustrated on the right margin of Figure 3.10, provides punctual information about the subsurface configuration of the steel fibers and it is possible to notice that the amplitude of the GPR signal reflects the distribution of fibers at a specific depth. Its amplitude is not only indicative of how fibers are close to each other but also reflects regions with the absence of fibers.

However, one should notice that electromagnetic signal strength in shotcrete is influenced by important processes including a scattering of energy attenuation, and reflection/transmission losses at interfaces. According to Luo et al. (2019), scattering of light from electromagnetic waves contributes to the visible appearance of most features and their visibility is related to the ratio of GPR wavelength to a reflector's radius. Once a feature is a visible, spatial vertical and horizontal resolution is a concern for a good GPR imaging quality. The authors implied that horizontal resolution is defined as the capability of a GPR system to distinguish 2 adjacent targets on the same plane, while vertical resolution describes the GPR system's ability to separate two adjacent features at different depths.

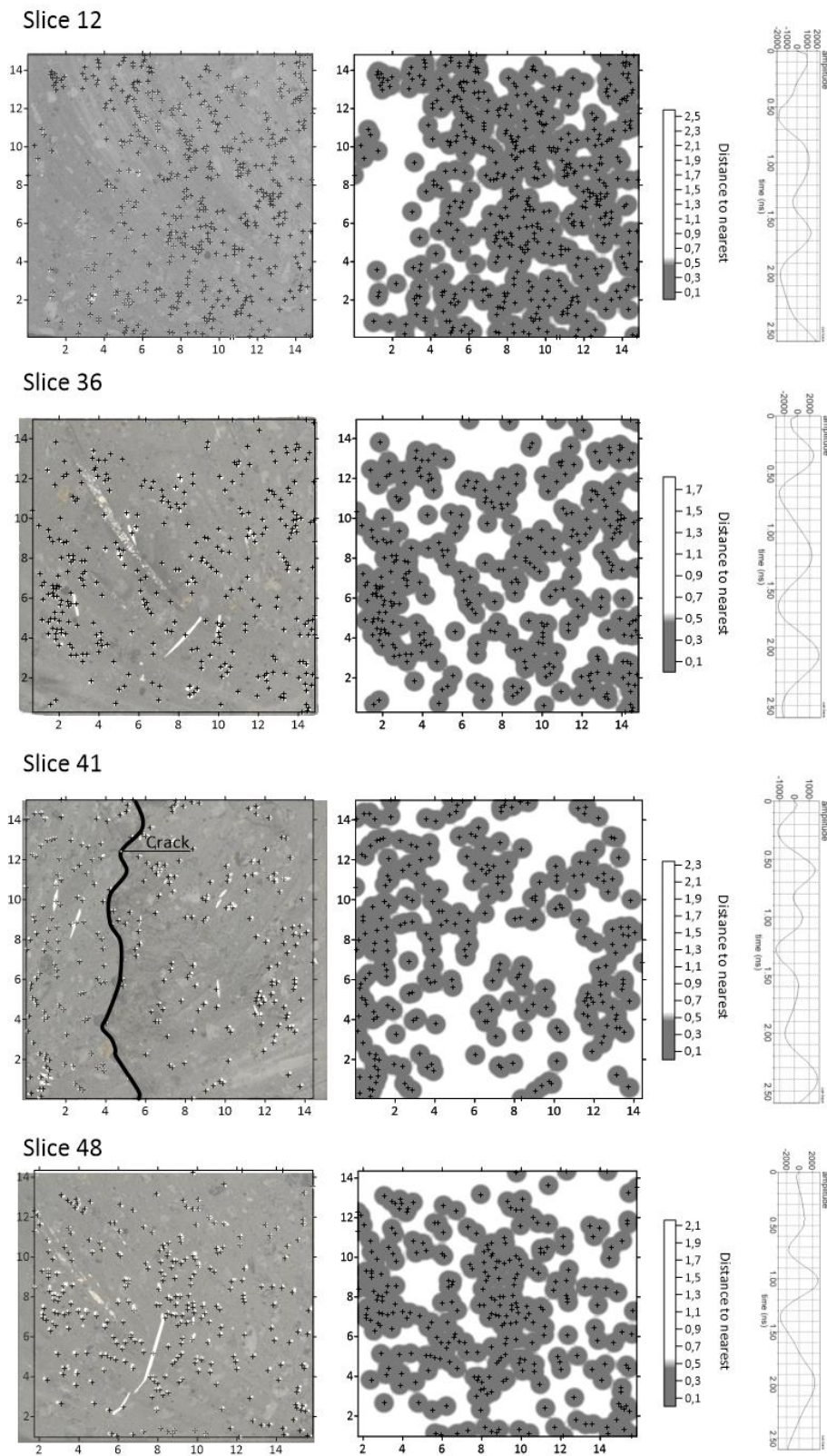


Figure 3.10. Comparison between GPR signal in a single radar trace mode, digital and processed images of four slices of a 1% fiber reinforced concrete short beam

The determined values of vertical and horizontal resolution are listed in Table 3.4. Since the horizontal resolution is a function of depth, the values listed on Table 3.4 correspond to the maximum resolution since they were calculated assuming that the antenna to the reflection surface distance was 15 cm. Since the target of interest herein is the hooked fiber, which has 60 mm in length, it is reasonable to assume that the GPR antenna used in the survey was able to detect them.

Table 3.4. Determined values of vertical resolution and maximum horizontal resolution

Fiber Reinforcement	v (m/ns)	k	r_{vertical} (mm)	$r_{\text{horizontal,max}}$ (mm)
0% fiber	0.0275	3.3	22,92	78,19
0.5% fiber	0.0195	3.9	16,25	71,93
1% fiber	0.0160	4.3	13,33	68,54

On the other hand, Luo et al. (2019), suggested that the dielectric contrast is another important aspect of GPR imaging quality. According to the authors, feature visibility is the ability of the GPR to distinguish the target feature from the background medium. The dielectric contrast is manifested as the reflection coefficient as Eq. 12 shows.

As Figure 3.11 shows, the amplitude of the GPR signal collected at similar distances in each self-consolidating concrete short beams seems not to be impaired by scattering and reflection/transmission losses at the reinforced concrete slab interface. The results show that the amplitude of the GPR signals was influenced by the presence of steel fibers within each short beam. Besides, it appears that despite the energy losses caused by scattering reflection/transmission losses at the reinforced concrete slab interface the propagating electromagnetic waves were able to penetrate the reinforced concrete slab as it was possible to detect reflectors position. In these cases, the position of the slab interface was approximately 3 ns.

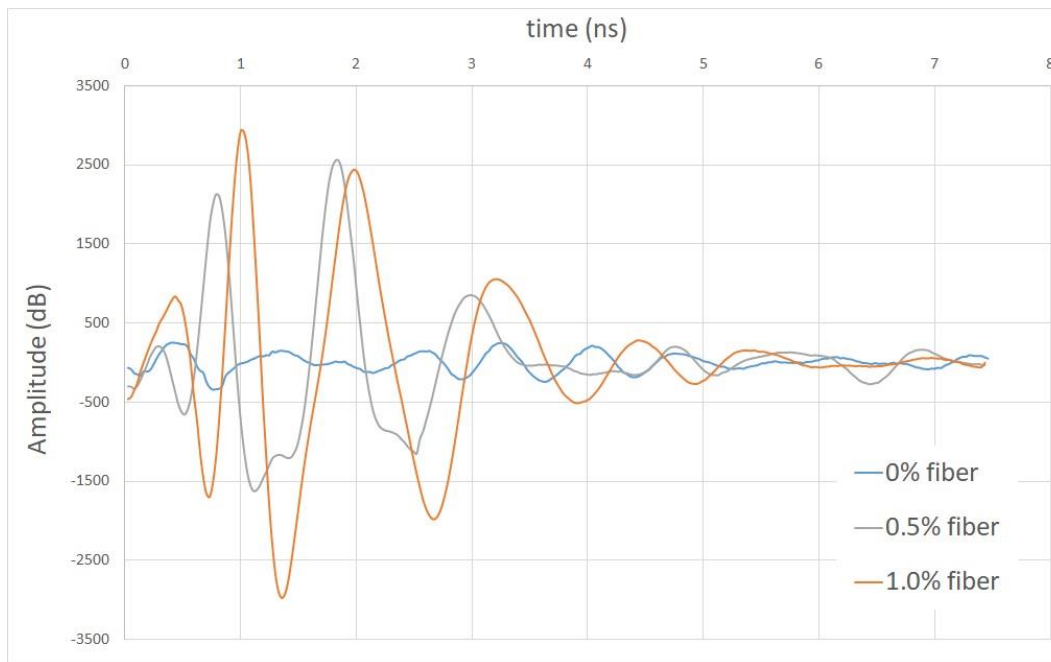


Figure 3.11. GPR signal amplitude

However, special attention should be drawn to energy attenuation, α showed on Eq. 10, which may be whitened as a function of relative dielectric permittivity, k , magnetic permeability, μ , and electrical conductivity, σ , as well as the frequency of the signal itself, $\omega=2\pi f$:

$$\alpha = \omega \sqrt{k\mu \frac{\sqrt{1+(\sigma/\omega k)^2} - 1}{2}} \quad \text{Eq. 23}$$

Figure 3.12 shows the results of GPR energy attenuation, expressed as dB decay, on the same short beams where the results of GPR signal amplitude were analyzed. Data were also collected at similar distances in each beam. The results suggest that the number of steel fibers on the self-consolidating concrete did not play a significant role in attenuation. Also, the observed similarities between the measured attenuation patterns suggest that the fiber-reinforced concrete short beams could still be considered as non-magnetic low-loss material despite the number of fibers used in the reinforcement (i.e., 40 kg/m³ for 0.50% and 80 kg/m³ for 1.00%).

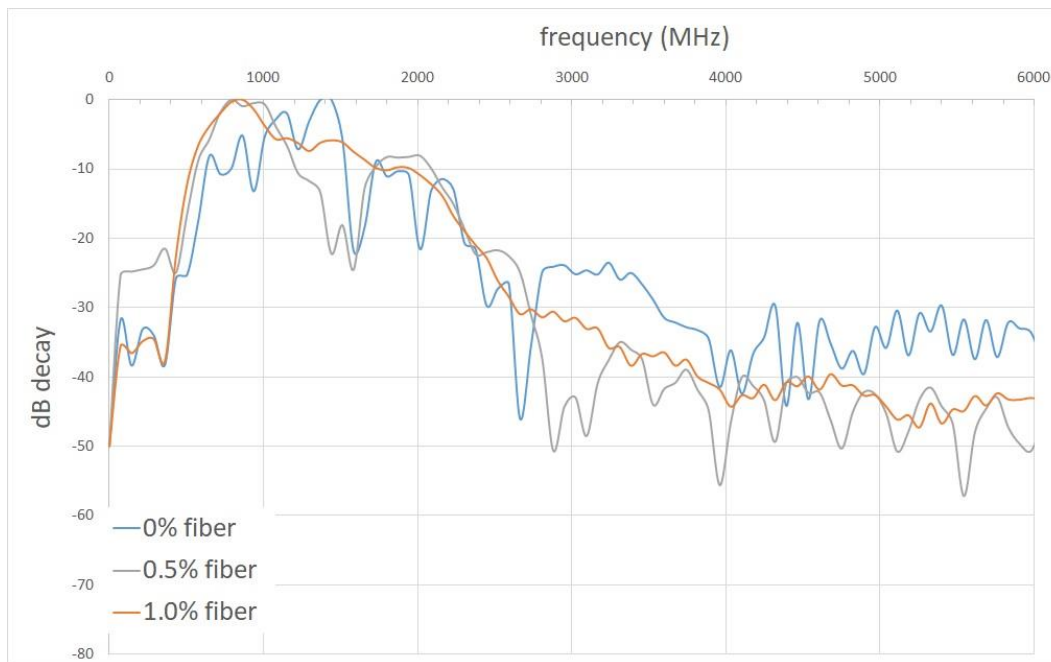


Figure 3.12. GPR energy attenuation

To show that a GPR system using high-frequency antennas could assess the weaker zones of steel fiber reinforcement within self-consolidating concrete, surveys were carried out on six short beams reinforced with 0.5% and 1% steel fibers. All surveys were carried out before a four-point test method was performed in each short beam. In all results shown in the subsequent figures, GPR data are displayed in either greyscale and wiggle mode as radargrams. According to Hugenschmid and Mastrangelo (2006), radargrams consist of a large number of traces lined up according to their acquisition position, as sketched in Figure 3.13, where the antenna is moved in the x-direction recording data continuously.

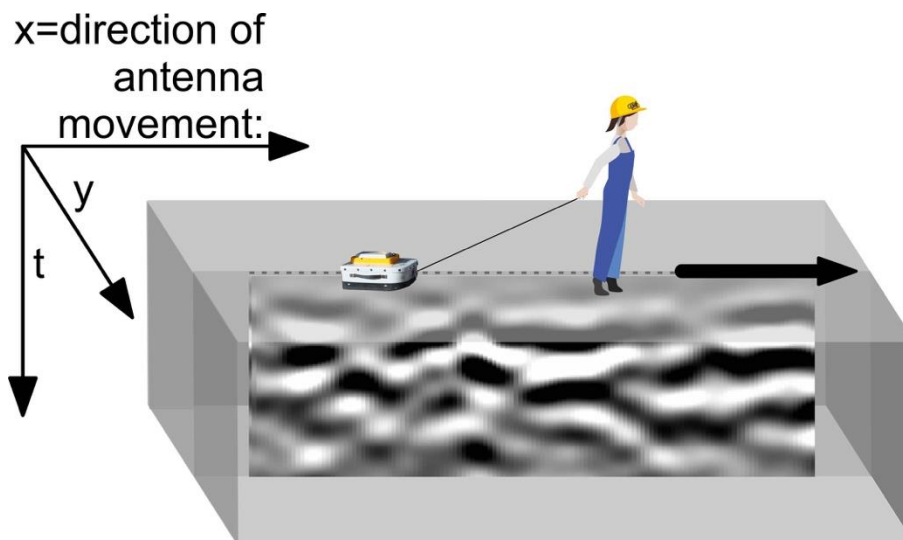


Figure 3.13. Schematic sketch of a radargram in greyscale mode

Figure 3.14-4.19 show the results. Each figure shows the generated crack on its top as well as the regions where different patterns of GPR reflection were spotted by the greyscale mode radargrams and the associated wiggles on each region.

In all radargrams, but the ones presented in Figure 3.15 and 4.17, cracks were formed on the region where wiggles presented lesser amplitude suggesting that GPR could well identify weaker zones of steel fiber reinforcement. In the radargram that showed the case of CP2 with 0.5% fiber reinforcement, the wiggle on the right presented lesser amplitude than the one represented by the white dot where the crack was formed. However, the crack formed at that place since it was subjected to a larger bending moment during the four-point test a bending moment diagram illustrated in Figure 3.20 shows. A similar pattern happened with CP1 with 1% fiber reinforcement, where the wiggle on the left presented lesser amplitude as compared to the one where the crack was formed. As in the former case, the region where the crack was formed was also subjected to a larger bending moment during the four-point test.

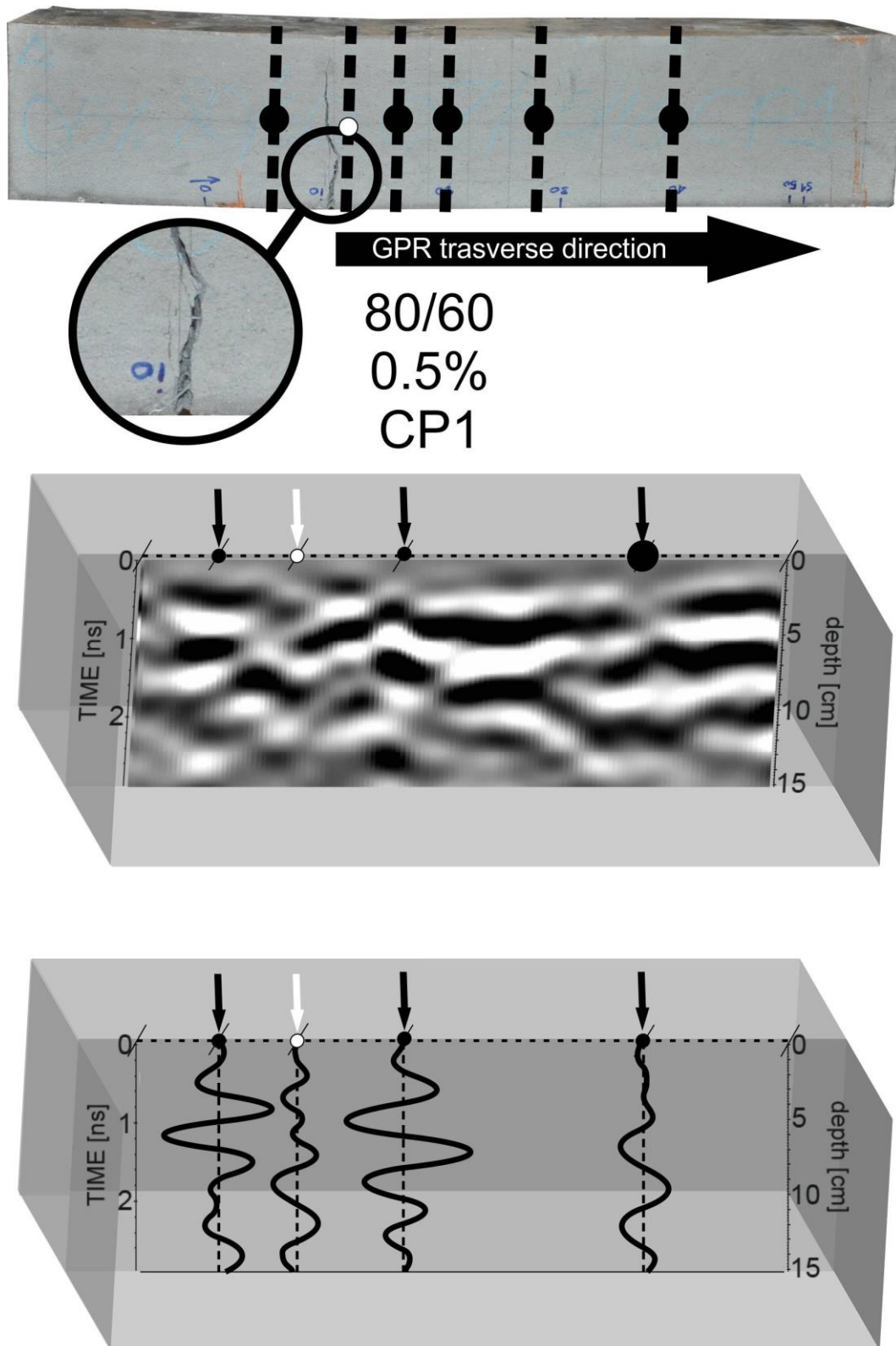


Figure 3.14. GPR survey on CP1 short beam with 0.5% fiber reinforcement

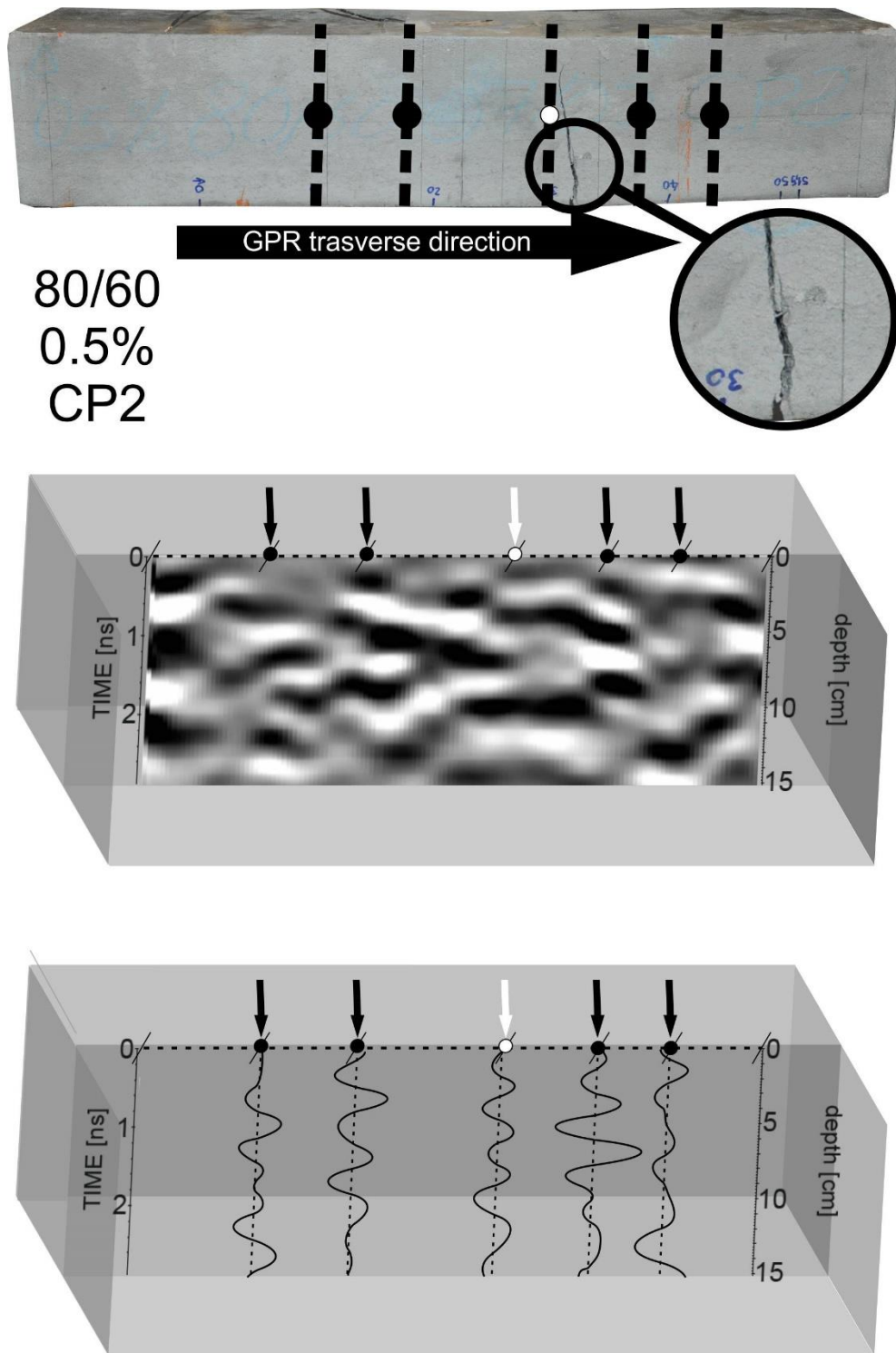


Figure 3.15. GPR survey on CP2 short beam with 0.5% fiber reinforcement

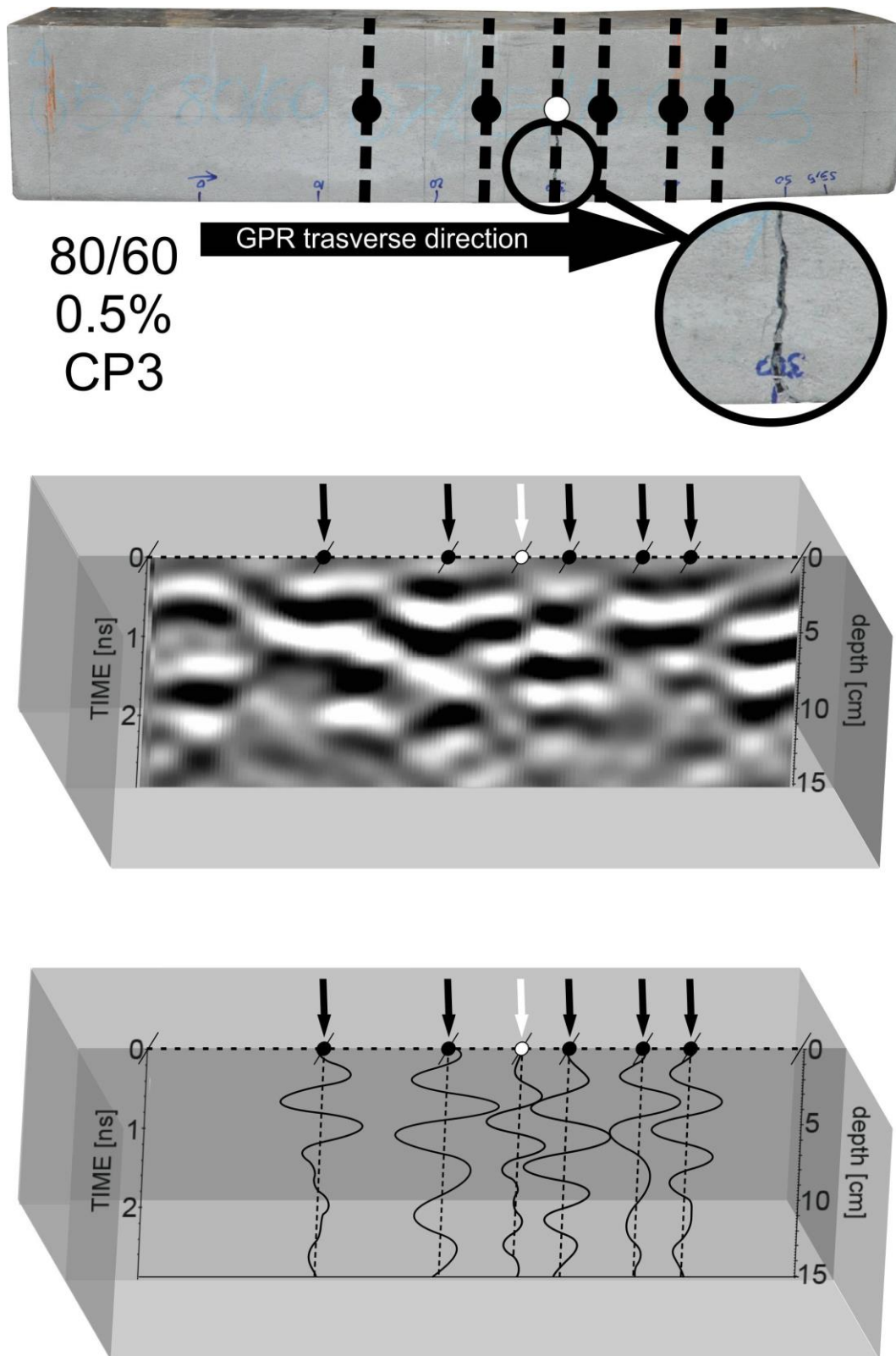


Figure 3.16. GPR survey on CP3 short beam with 0.5% fiber reinforcement

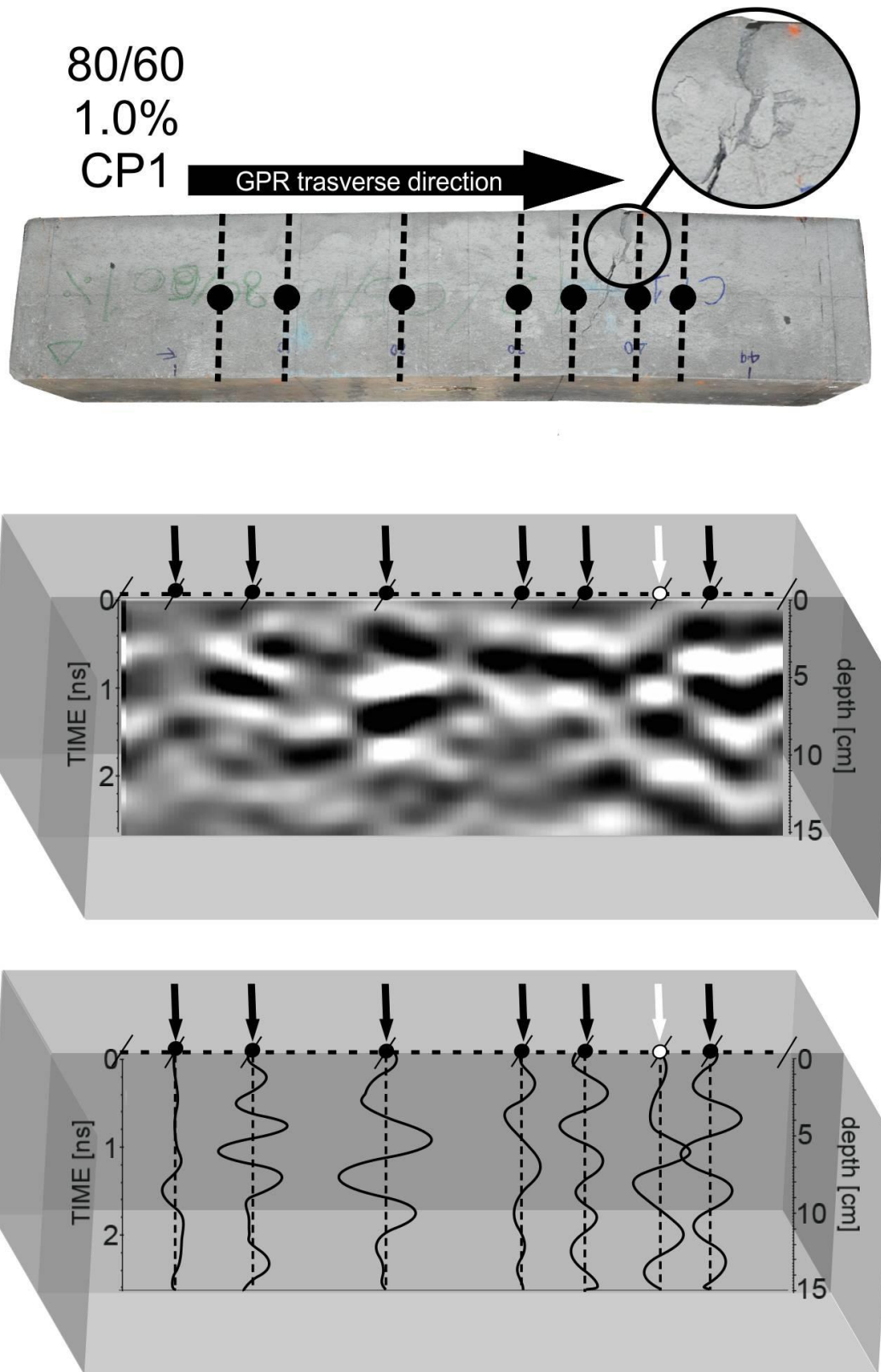


Figure 3.17. GPR survey on CP1 short beam with 1% fiber reinforcement

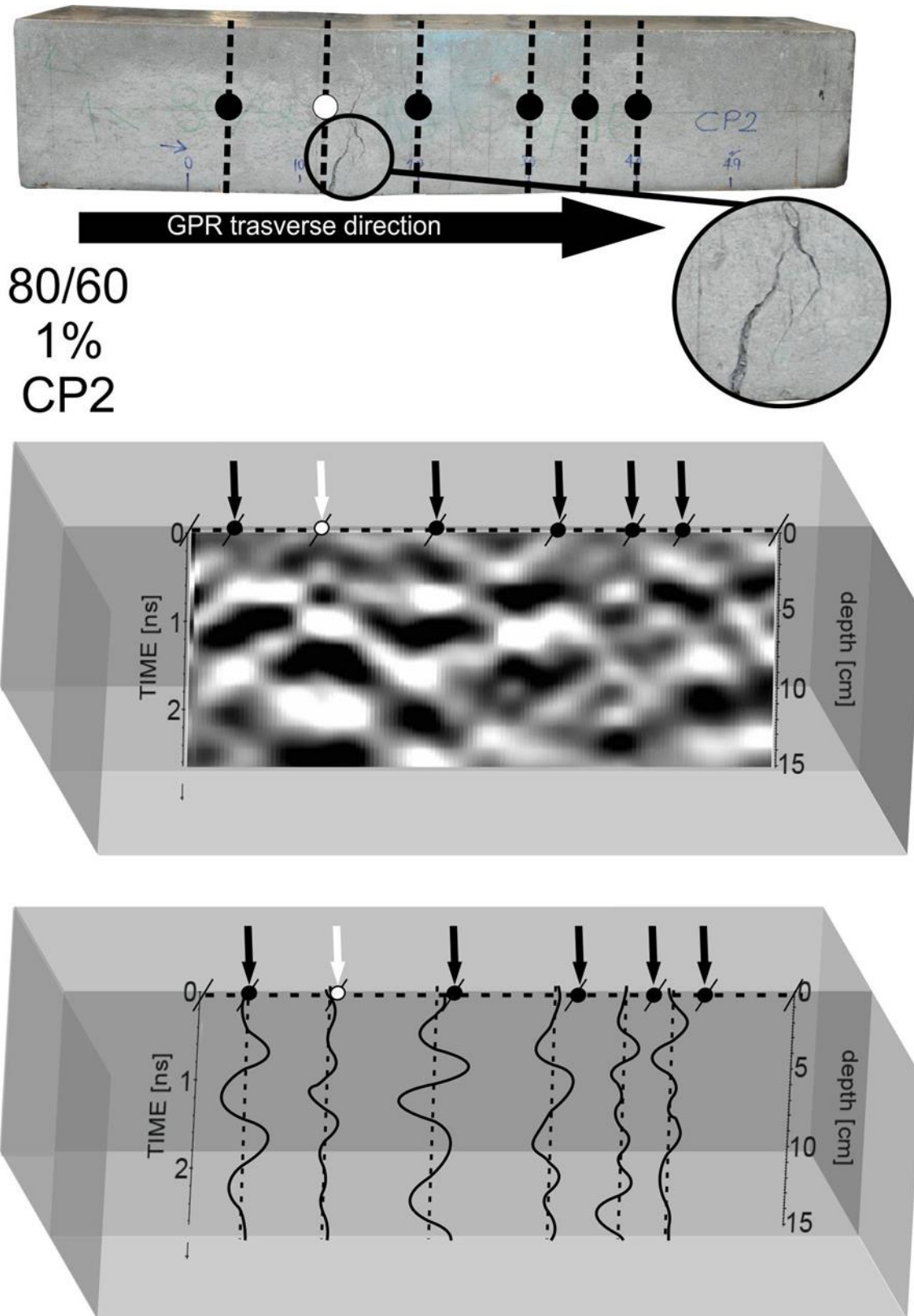


Figure 3.18. GPR survey on CP2 short beam with 1% fiber reinforcement

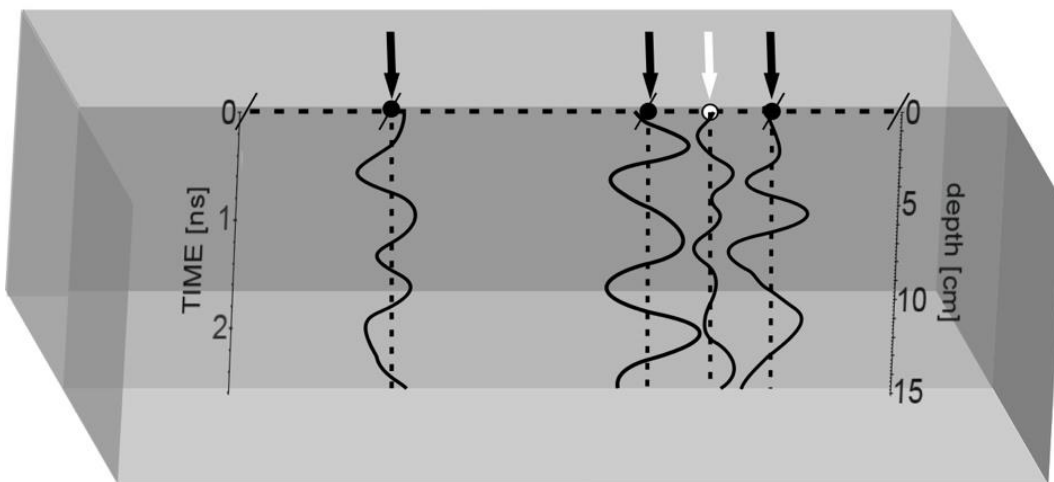
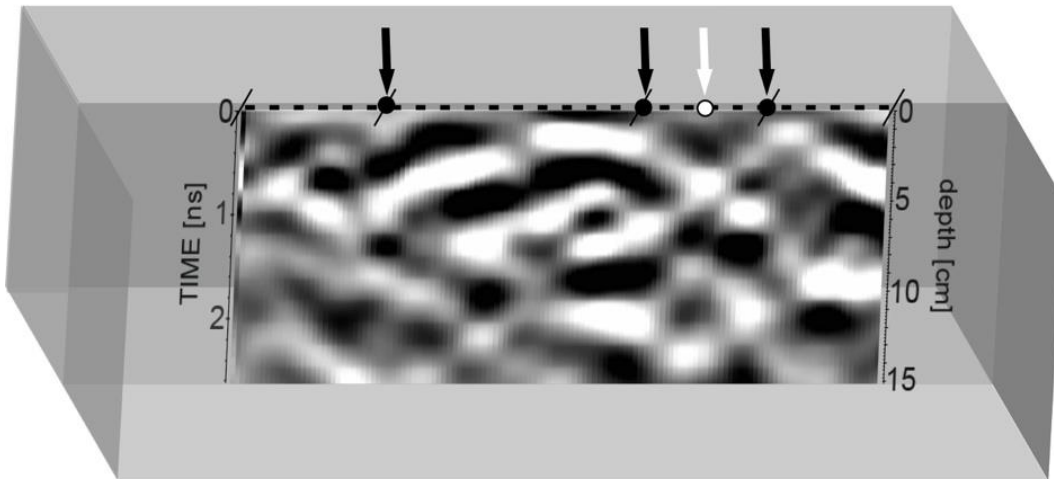
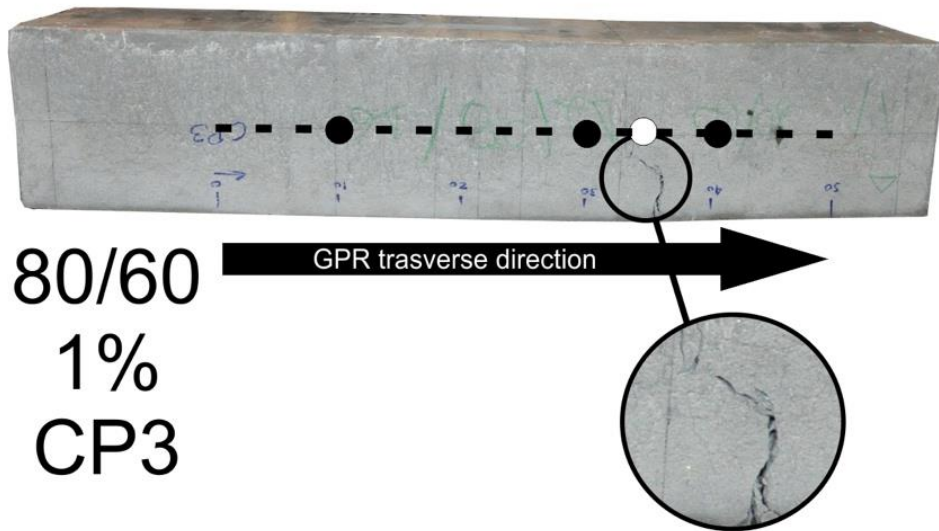


Figure 3.19. GPR survey on CP3 short beam with 1% fiber reinforcement

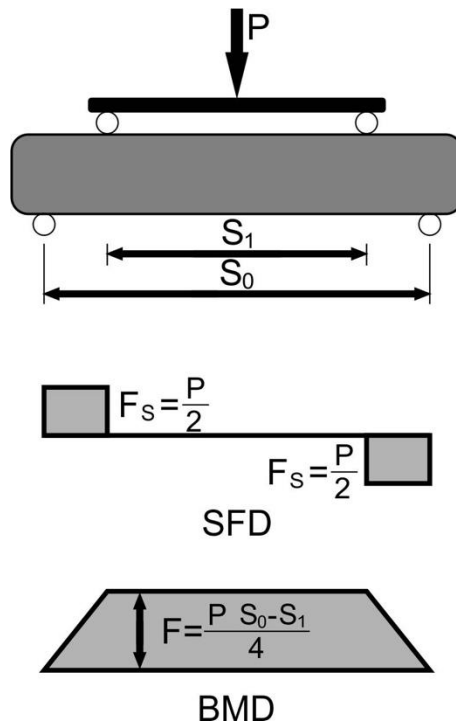


Figure 3.20. Shear force and bending moment diagrams for four-point bending test

3.3 Conclusions

Based on extensive mechanical tests, image analyses and GPR surveys in this study, the following conclusions can be drawn:

- The distribution of steel fibers within a self-consolidated shotcrete beam is not uniform in terms of the number and spacing of fibers in different sections of the short beam.
- The digital and processed images in fiber distribution study are correlated well with the GPR mappings in a single radar trace mode. In particular, the GPR amplitude does not only provide information on how close the fibers are to each other but also reflects regions with no fibers. A GPR system using high-frequency antenna can thus be applied to assess the weak zones of steel fiber reinforcement within self-consolidating concrete beams.
- As a fast non-invasive method, GPR cannot quantitatively characterize the orientations of the fiber in the concrete nor quantitatively determine the steel fiber content.

4 Health assessment of deteriorating reinforced concrete structures in residential buildings in coastal areas using GPR: A case study in the Brazilian Northeastern coastline

Fortaleza is the fifth most populated city in Brazil with approximately 2.6 million inhabitants and one of the most important economic and recreational hubs in Northeastern Brazil. Fortaleza has a tropical, semiarid climate where rainfalls are practically restricted to the rainy season (essentially from February to May). Fortaleza is facing north-east and due to its geographical position, as mentioned by Candella (2019), it is directly exposed to permanent east-to-west prevailing winds that flow in the Earth's equatorial region (i.e., trade winds). According to Pereira et al. (2015), during the dry season when skies are mostly cloud-free, wind speeds are stronger and steadier (i.e., ~6.5 m/s), whereas during the raining season winds are less intense and more breeze-like (i.e., ~3 m/s). The authors also pointed out that the wind intensifies around noon. The modal direction is east–southeast in the rainy season and southeast in the dry season.

The chloride concentration in the Fortaleza sea breeze has a large variation within its city limits. Data obtained from Cabral and Campos (2016) indicates that chloride ions concentration is rapidly reduced with distance from the sea line. The study has also shown that are different chloride ions concentration levels in the salt spray zone concerning distance from the sea line corroborating with the findings of Moreno et al. (2015). The authors also found out that the average chloride ions concentration within a 50 m distance from the sea line are much larger in Praia do Futuro (~1498.77 mg.m⁻².d⁻¹) since winds come to the city through it bringing all the charge of marine aerosols. It was also found that peak values were measured during the dry season where wind speeds are stronger and steadier.

Despite chloride-induced corrosion on concrete structures constitutes a major cause of concrete anomalies in residential buildings in Fortaleza, only recently it has generated a major concern amongst its inhabitants. Much of the attention was due to the victims from building collapses that occurred during the past couple of years. Accidents took place not only in low standard residential buildings but also in luxurious residential buildings as Figure 4.1 illustrates.



Figure 4.1. Recent residential building collapses in Fortaleza: a) building collapse in Maraponga district after its columns failed (June 2019), b) balcony collapse in Meireles district (March 2015), and c) debris of Andrea building in Dionísio Torres dist.

According to Bertolini et al. (2013), inspection should be considered any time when a structure shows signs of degradation, and it is needed to investigate the causes of the phenomenon and its extent. Some authors, including Hobbs and Kebir (2007), advocate the use of non-destructive test methods in such inspections since they do not damage or affect the structural performance of building components. In addition, as pointed out by Bertolini et al. (op. cit.), inspection is necessary to look for the best repair solution and to avoid corrosion problems in the future. In coastal

areas, concrete structures showing damage caused by reinforcement corrosion have to be immediately repaired in order to reach their expected service life.

The objective of this paper is to validate a sound procedure of health assessment of deteriorating reinforced concrete structures in coastal areas employing the ground-penetrating radar (GPR) in such a way that any damage introduced, or any inherent fault would be immediately detectable. GPR was chosen since it is considered one of the most popular non-destructive testing methods adopted for concrete structure imaging because of its relative insensitivity to ambient conditions, high resolution, effectiveness, and availability of real-time images (Sbartai et al., 2006). Further to this, the objective is that, after GPR detection, any fault could be located and its severity inferred so that decisions can be made as to what actions need to be taken next to increase human safety and reduce economic losses.

4.1 Theoretical information

4.1.1 Chloride induced corrosion

According to Liu et al. (2017), chloride aerosol is generated along the seashore by breaking wave movement and transported inland by the wind. Low levels of chloride ions are necessary to initiate corrosion in structures exposed to the atmosphere, where oxygen can easily reach the reinforcement (Guimarães et al., 2011). In coastal areas, where the concrete structure is exposed to a sea breeze, marine aerosols are deposited on the surface of concrete structures and chloride ions then penetrate their masses resulting in a strong likelihood of them corroding the reinforcement (Xu et al., 2011).

Moreno et al. (2015) suggested that chloride ions build up faster than atmospheric carbon dioxide, which is responsible for carbonation of the concrete so that chloride action is often the main factor in the corrosion of reinforcement in this type of atmosphere. Once on the surface, as explained by Hong et al. (2014), chloride ions penetrate under cyclic wetting and drying cycles by several mechanisms. Chloride ions are absorbed by capillary action together with moisture through the interconnected pores in the cement paste. According to Hong et al. (op. cit.), the depth of chloride ions penetration driven by absorption is governed by the

hydraulic conductivity and porosity of the concrete cover mass as well as by the resulting moisture from the dry-wetting cycle. Bertolini et al. (2013) revealed that porosity in cement paste consists of capillary pores, gel pores, and calcium silicate hydrate interlayers. The authors mentioned that capillary pores are the remains of original water containing spaces between cement particles that have not been filled up by products of hydration. They are the largest, possessing diameters over 5 nm, and their number and interconnectivity control the ingress of chloride ions, oxygen and moisture into the concrete. The authors also mentioned that gel pores and interlayer spaces are believed to be too small and disconnected to contribute to transport. Even on dry surfaces, dissolved chloride ions are absorbed by capillary action together with moisture through the interconnected pores in the cement paste. Once absorbed, chloride ions are transported by diffusion from the region with a higher concentration in the pore solution into the deeper region with minor concentration since the concrete mass seldom dries out. However, one must point out that the diffusion of chloride ions is a much slower process than absorption. The diffusion process, as mentioned by Kurumisawa and Nawa (2016), is also strongly dependent upon the concrete pore structure and that the diffusion coefficient is related to the porosity, tortuosity, and pore connectivity. A third mechanism, cited by Bertolini et al. (2013), is the transport via cracks in the concrete cover. According to the authors, while interconnected capillary porosity provides a tortuous path for the ingress of chloride ions, oxygen and moisture into concrete, cracks provide a more direct path.

Chloride-induced reinforcement corrosion takes place once the concentration of chloride ions at the reinforcement reaches the critical chloride content. Bertolini et al. (2013) describe the chloride threshold as the chloride content required for depassivation (i.e., drop in the measured corrosion potential) or the chloride content necessary to reach by an averaged sustained corrosion rate higher than 2 mA/m². As soon as this stage is reached, chloride ions lead to a local breakdown of the protective oxide film on the reinforcement in alkaline concrete, so that a subsequent localized corrosion attack takes place. The corrosion products (i.e., rust) accumulates in the concrete-steel interface zone and can quickly lead to a marked reduction in the cross-section of the reinforcement without being manifested by cracking or spalling and is thus difficult to detect by visual inspection. According

to Hong et al. (2014), when the rust expansive stress exceeds the local tensile strength of the concrete, cracking occurs in the surrounding concrete generating spalling or delamination of the concrete cover. This process is illustrated in Figure 4.2.

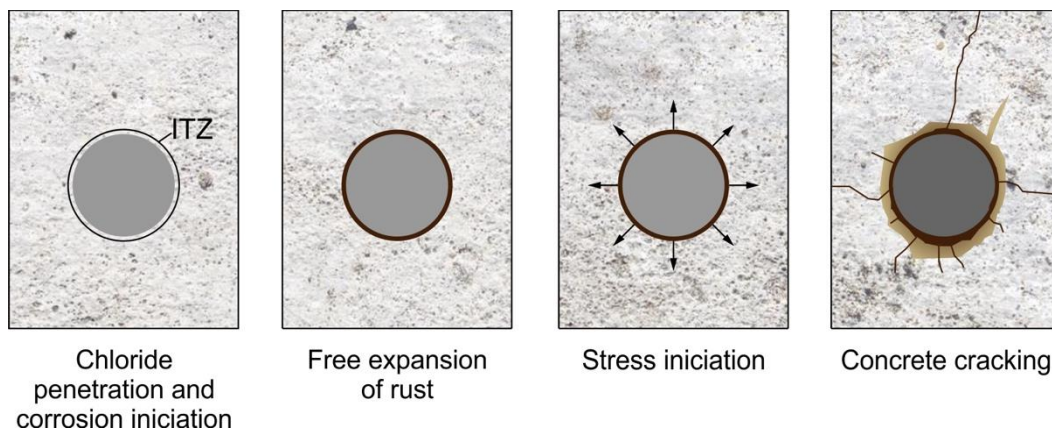


Figure 4.2. Reinforcement corrosion and cracking patterns

4.1.2 GPR principle

GPR is a time-domain system that applies an impulse to the antenna, placed close to the air-ground interface, that creates and detects key electromagnetic fields. According to Annan (2009), the GPR transmitter antenna translates the excitation voltage into a predictable temporal and spatial distributed field and the receiving antenna detects the temporal variation of a vector component of the electromagnetic field (EM) field and translate it into a recordable signal. The author also points out that a shield could be used to focus or direct EM signal downward. Besides, shielded antennas also minimize the direct transmitter to receiver energy, minimize the energy that escapes into the air and minimize external electromagnetic noise. The appropriate antenna selection is made in accordance with the anticipated depth of investigation. The higher the antenna frequency the lower the antenna signal penetration through the porous or fractured media.

During a scan, a GPR transmitter emits through an antenna an electromagnetic pulse source into the concrete mass. When this pulse encounters a boundary between materials having different dielectric permittivity, it will be

partially reflected or refracted back to the surface where a receiving antenna records the magnitude and arrival time of the turned pulse.

GPR waves propagation is governed by the permittivity of a dielectric material ε that can be written in terms of real and imaginary parts as

$$\varepsilon = \varepsilon' - i\varepsilon'' \quad \text{Eq. 24}$$

where ε' is the dielectric permittivity of the material, ε'' is the loss factor, and $i = \sqrt{-1}$ (Sbartai et al., 2006). According to Halabe et al. (1993), in a typical concrete mass with low to medium salt and moisture content the dielectric constant is related to the propagation velocity (v) of EM waves in the material is given by Eq. 25.

$$\varepsilon' = \left(\frac{c}{v}\right)^2 \quad \text{Eq. 25}$$

where c is the propagation velocity of EM waves in free space (2.998×10^8 m/s).

Sbartai et al. (op. cit.) suggested that the loss factor ε'' strongly affects the attenuation of EM waves due to absorption. According to the authors, the attenuation coefficient α of EM waves could be expressed as:

$$\alpha = \frac{\omega\varepsilon''}{2} \sqrt{\frac{\mu_0}{\varepsilon'}} \quad \text{Eq. 26}$$

where ω is the angular frequency and μ_0 the magnetic permeability of free space. Hong et al. (2014), stated that EM energy is adsorbed primarily due to dielectric relaxation and electrical conduction.

Since concrete is a composite material constituted by a solid phase (i.e., mineral aggregate, hydrated components, anhydrous cement), a gaseous phase (i.e., air), and a liquid phase (i.e., pore solution), the permittivities of solid and gaseous phases are considered to be real numbers and the permittivity of free water is considered a complex number since its molecules are free to rotate.

Eq. 26 suggests that moisture in the concrete mass will attenuate the high-frequency component of the EM signal faster than the low-frequency component. Hong et al. (op. cit.) pointed out that moisture will cause a downshift of center frequency and will reduce the signal amplitude (e.g., moisture will serve as a low-pass filter). The authors also mentioned that when a concrete mass is contaminated with chloride, the conductivity is produced by the chloride dissolved in the pore water and with increasing chloride content the GPR signal attenuation increases.

4.2 Experimental program

The health of deteriorating reinforced concrete structures in coastal areas were investigated in three residential buildings constructed during the 1980's. The buildings are situated in three different districts of Fortaleza (i.e., Praia do Futuro, Varjota and Aldeota) that show different patterns of chloride concentration sea breeze as established by Cabral and Campos (2016). The residential buildings locations are shown in Figure 4.3.

The building was chosen to represent the most aggressive zone (i.e., Praia do Futuro district) is located 200 m from the sea line with respect to the sea breeze direction. It has eight floors, each with two apartments. The building has no underground floor and its ground floor is used as parking slots. It went under maintenance twice during its lifetime. During the last maintenance, carried out 10 years ago, ceramic tiles were placed on its front facade and ground columns in order to minimize concrete corrosion as Figures 4.4a and 4.4b show. However, as it can be seen from Figure 4.4c, corrosion is still a major issue in its beams and slabs.



Figure 4.3. Satellite image of Fortaleza (Google Image)

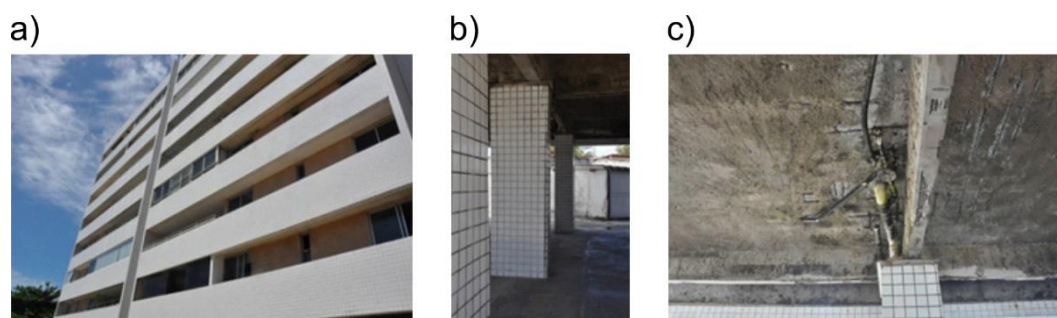


Figure 4.4. Building at Praia do Futuro district

The building was chosen to represent the second most aggressive zone (i.e., Varjota district) is located 2,600 m from the sea line concerning to the sea breeze direction. It has three floors, each with two apartments. The building showed in Figure 4.5 has no underground floor and its ground floor is used as parking slots. It went under maintenance once during its lifetime.



Figure 4.5. The building at Varjota district

The building was chosen to represent the third most aggressive zone (i.e., Aldeota district) is located 5,200 m from the sea line with respect to the sea breeze direction. It has five floors, each with four apartments. The building has no underground floor and its ground floor is used as parking slots. It was currently under maintenance when the GPR survey was carried out as can be seen from Figure 4.6.

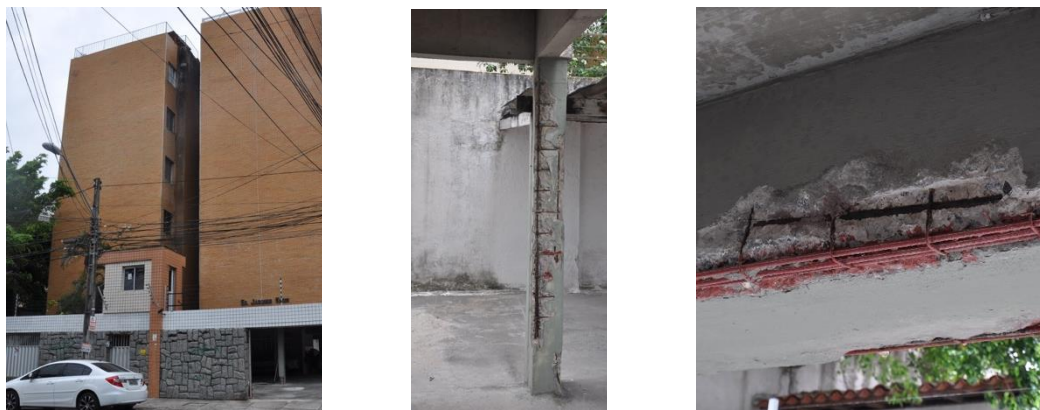


Figure 4.6. Building at Aldeota district

GPR surveys at each building were carried out at selected ground floor columns to provide information to design their as-built drawings. The purpose of the survey was also to detect any unseen damage and location. Ground floor columns were chosen since they are the structures that primarily control the building stability.

2D and 3D data were acquired using a MALÅ CX ground penetrating radar (GPR) concrete scanning system with a shielded 1.2 GHz center frequency. According to Pérez-Gracia et al. (2009), the shielded 1.2 GHz is a wideband frequency antenna, with bandwidth on the order of its nominal center frequency. The authors also stated that the fundamental wavelength of the emitted wave is about 18.8 cm and the separation between the receiver and the transmitter devices is 6 cm. Two panels of medium-density fiberboard (MDF) were used next to each column to provide enough space to perform a continuous scan on its entire width as Figure 4.7 shows.



Figure 4.7. GPR survey setup at the building on Aldeota district

The GPR signal velocity was estimated from GPR profile data collected perpendicular to the columns rebars. The hyperbola fitting method available in the REFLEXW software version 9.0 (Sandmeier, 2019) was used to determine the signal velocity. Data processing was carried out following recommendations given by Bennedeto et al. (2017), with the processing workflow shown in Figure 4.8.

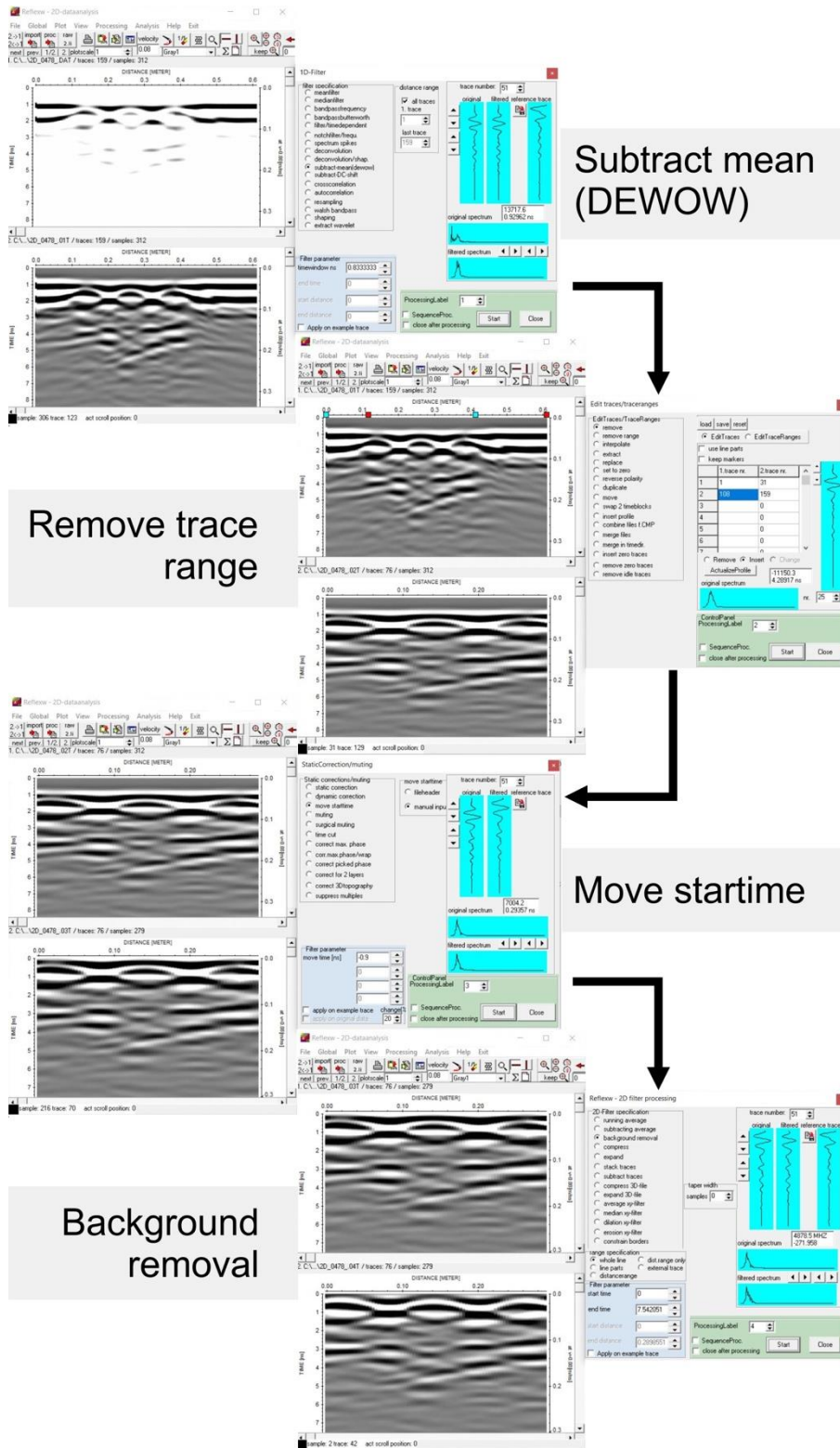


Figure 4.8. Data processing sequence

4.3 Experimental results and discussions

Producing construction drawings that have been revised to show changes made to the original plans during construction (i.e., as-built drawings) is an important task in civil engineering projects. In fact, as Angers (2001) mentioned, complete and accurate structural detailing drawings are more than just paperwork acquired at the end of a construction project. According to the author, as-built drawings are essential tools that provide critical information in an emergency and non-emergency situation. Further to this, like Gargoum et al. (2018) suggested, these drawings must be updated whenever major maintenance work takes place.

GPR is a useful tool in producing structural detailing drawings since it can provide the thickness of covering concrete and the depth and location of reinforcement. The accuracy of a GPR estimate of the aforementioned parameters is influenced by important processes including a scattering of energy attenuation, and reflection/transmission losses at interfaces. According to Luo et al. (2019), scattering of light from electromagnetic waves contributes to the visible appearance of most features and their visibility is related to the ratio of GPR wavelength to a reflector's radius. Once a feature is visible, the authors also pointed out that spatial vertical and horizontal resolution are a concern for a good GPR imaging quality. The authors implied that horizontal resolution is defined as the capability of a GPR system to distinguish 2 adjacent targets on the same plane in the direction of the antenna movement. According to Pérez-Gracia et al. (2008a), the horizontal resolution depends on the antenna frequency, the achieved depth and on the electromagnetic properties of the medium. The authors suggested that horizontal resolution might also be affected by filtering and stacking. Luo et al. (op. cit.) described vertical resolution as the GPR system's ability to separate two adjacent features at different depths (i.e., the capability of the antenna to detect two horizontal discontinuities as separate anomalies). According to Pérez-Gracia et al. (2008a), it is a resolution in time and also depends on the wave velocity and its length.

The effectiveness of GPR in gaining vital information about the thickness of covering concrete, and the depth and location of reinforcement (rebar) is illustrated in Figure 4.9. This figure shows the result from a GPR scan carried out at column P17 from the Aldeota district building. This column was chosen since the concrete

covering on its toe was removed and its rebars were exposed providing a means of validation of the GPR estimates.

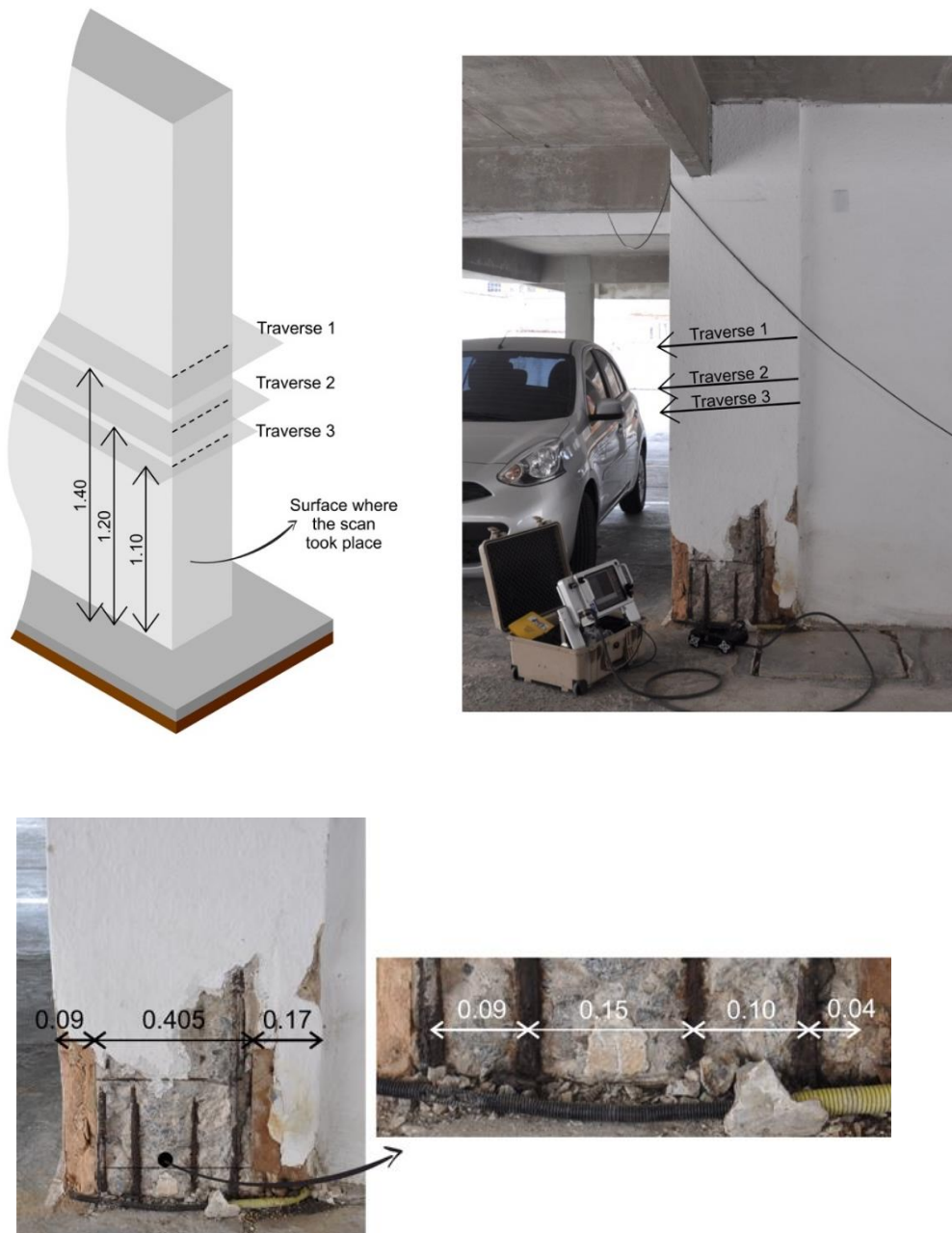


Figure 4.9 (cont.). Results from the GPR scan carried out at column P17 from the Aldeota district building (indicated values are in meter)

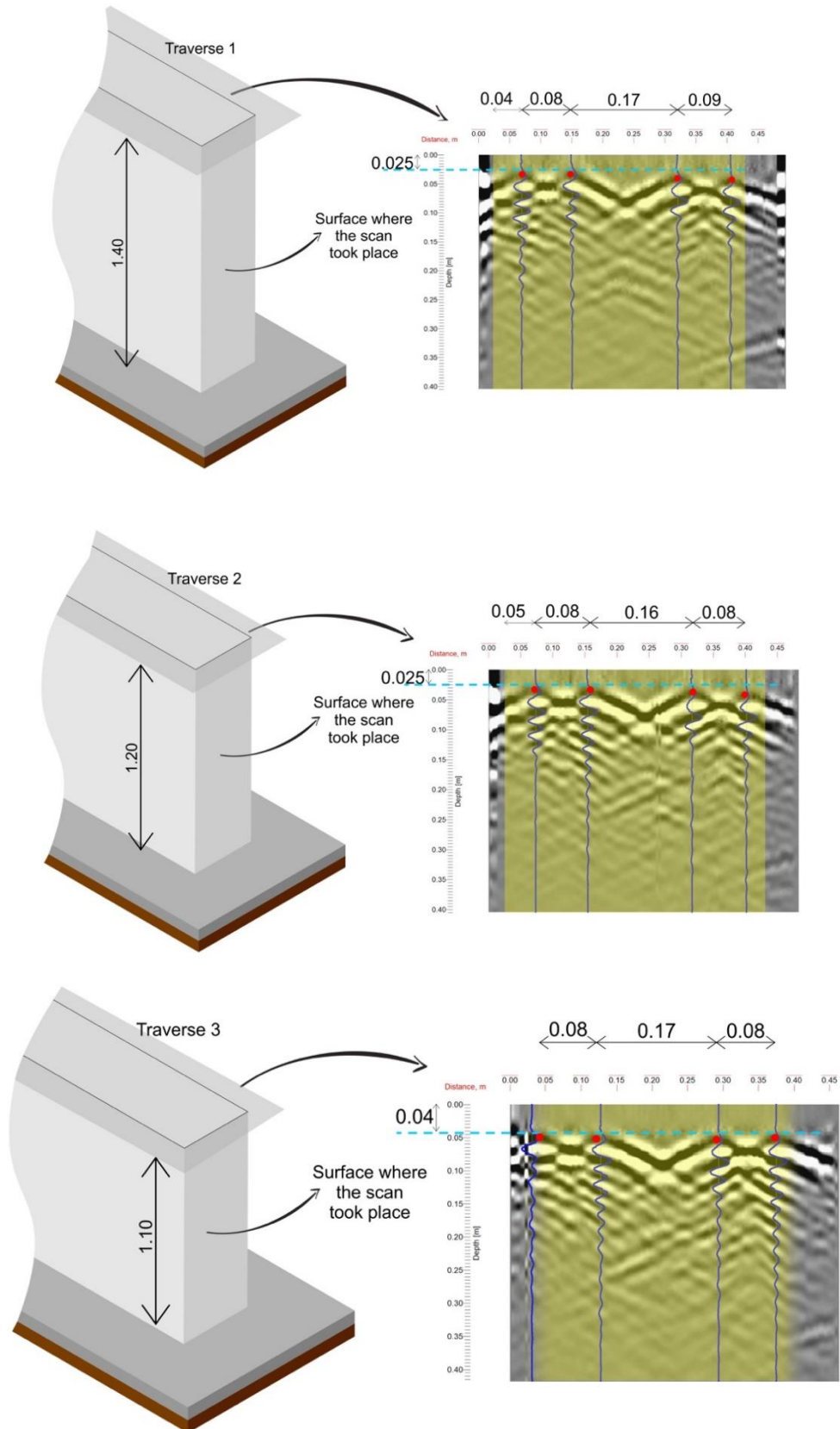


Figure 4.9 (cont.). Results from the GPR scan carried out at column P17 from the Aldeota district building (indicated values are in meter)

The resolution of the GPR scan is estimated through the traveling velocity of the GPR wave. As Figure 4.10 shows, traveling velocities determined by the hyperbola fitting method available in the processing software have different magnitudes since the resulting hyperbolas have different width. Narrow hyperbola indicates a quicker speed of radar wave into concrete whereas wider shaped hyperbola indicates the slower speed of radar wave. The results at each trace are illustrated above the vertex of each hyperbola. The horizontal and vertical resolutions for each trace calculated using Eq. 2.4 and 2.5 are shown in Table 4.1. The horizontal resolution was calculated assuming that the thickness of covering concrete in this traverse was 25 mm.

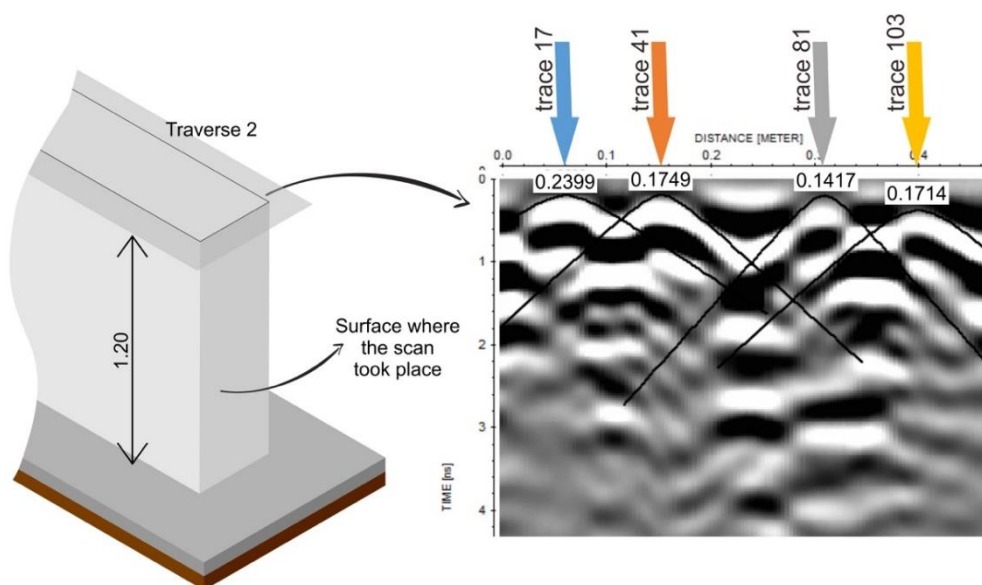


Figure 4.10. The traveling velocity of the GPR wave

Table 4.1. Determined values of vertical resolution and horizontal resolution

Trace	v (m/ns)	ϵ'	Γ_{vertical} (mm)	$\Gamma_{\text{horizontal}}$ (mm)
17	0.2399	3.53	4.99	16.73
41	0.1749	4.14	3.64	14.66
81	0.1417	4.60	2.95	13.51
103	0.1714	4.18	3.57	14.55

By comparing the estimated with the actual values, an average error of all rebars spacing was found to be 11%. It was also found that the thickness of covering concrete, and the depth and location of reinforcement were visible since the estimated values were well above the calculated resolution. Therefore, results showed a good agreement between the measured values and those estimated by GPR processing and interpretation.

In the chloride-induced corrosion process of embedded steel rebars in concrete, iron ions from the rebar are converted to iron oxide or rust. As Figure 4.11 suggests, during a GPR scanning of chloride-induced deteriorated concrete columns, the EM wave travels through the rust contaminated concrete towards the rebar, penetrating through the corrosion products to hit the surface of the rebar and then reflected back towards the receiver of the GPR antenna. As mentioned by Annan (2009), the magnitude of the reflection wave from the interface of two different materials depends on the contrast of the dielectric constants of the two media. At the interface of the corroded product and the concrete, the dielectric contrast is not so high since the dielectric constant of iron oxide (i.e., 14) is a little higher than the dielectric constant of concrete (Clipper Controls, 2019). In this case, a part of the incident wave gets reflected and most of it travels through the iron oxide and/or rust medium. On the other hand, since steel is a very good electrical conductor, the contrast between the corroded products and the non-corroded core of the rebar is very high and most of the incident wave gets reflected.

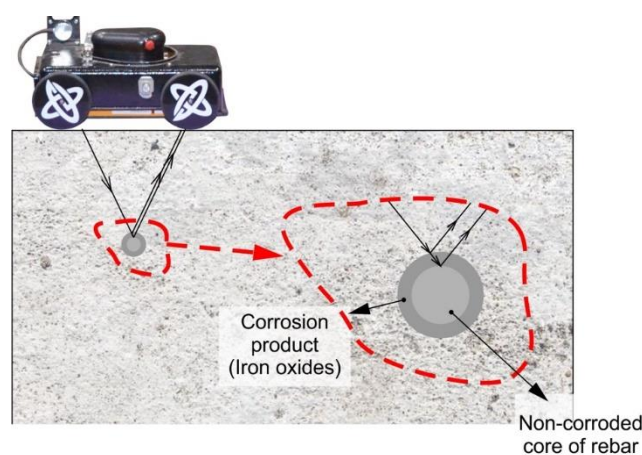


Figure 4.11. GPR scanning of corroded rebar in concrete

Luo et al. (2019) suggested that the dielectric contrast is another important aspect of GPR imaging quality. According to the authors, feature visibility is the ability of the GPR to distinguish the target feature from the background medium. The dielectric contrast is manifested as the reflection coefficient showed on Eq. 12.

The strength of EM waves emitted from a GPR antenna weakens as they travel through the concrete mass. According to Rhee et al. (2019), EM attenuation depends on electric conductivity, media and magnetic relaxation, and material and dielectric damping of concrete. It is generally believed that a sound concrete mass presents low hydraulic conductivity, low water content, and can be considered as a low-loss material irrespective of conductivity. The authors also mentioned that the attenuation of the EM waves transmitted to concrete is governed by the dielectric damping based on the constant antenna frequency and the relative permittivity of concrete. As stated earlier, permittivities of solid and gaseous phases are considered to be real numbers and permittivity of free water is considered a complex number since its molecules are free to rotate. Further to these, as Eq. 26 suggested, moisture in the concrete mass will attenuate the high-frequency component of the EM signal faster than the low-frequency component and will reduce the signal amplitude. Hence, it seems reasonable to assume that in a cured unreinforced concrete specimen attenuation will be very low. Figure 4.12 shows that this is the case.

Rhee et al. (2019) also suggested that a reduction in the amplitude of EM waves is observed with increasing the depth of a reflector in concrete. In contrast, deteriorated concrete is characterized by its higher hydraulic conductivity due to enhanced porosity and micro-cracks, which allows conductive materials such as moisture and chlorides to penetrate the concrete. The conductive enhancement has been widely used as a measure of the severity of deterioration in concrete structures using the GPR (Rhee et al. 2018; Varnavina et al. 2015).

This pattern is illustrated in Figure 4.13 where deterioration of the concrete column and the corrosion of its rebars could be also be assessed by the attributes provided by a GPR scan. It can be seen from Figure 4.13 that deterioration is marked with reducing the depth of the reflector, increasing in the amplitude of EM waves and increasing in attenuation expressed by the dB decay.

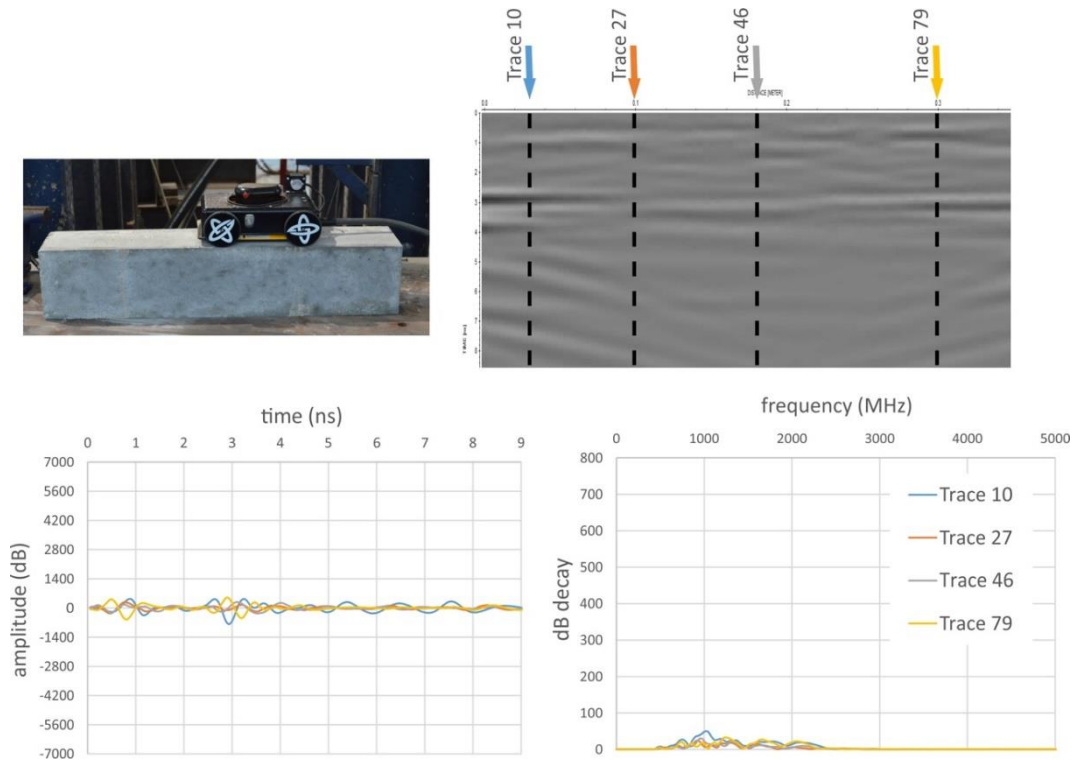


Figure 4.12. Attributes derived from the GPR scan carried out at a cured unreinforced concrete short beam

Figure 4.14 shows a typical result obtained from the survey carried out at the Varjota district residential building. This figure shows that the attributes obtained on trace 81 and 51 follow the aforementioned pattern of deterioration (i.e., deterioration is marked with reducing the depth of the reflector, increasing in the amplitude of EM waves and increasing in attenuation expressed by the dB decay). However, one can notice on trace 21 that the depth of the reflector is lower than those observed on trace 81 and 51. This could be related to the actual position of the rebar within the column caused by the concrete placement procedure. Since this behavior, illustrated in Figure 4.15, is a rather common one should bear in mind that the position of the vertex of the hyperbola should be taken with precaution when analyzing concrete deterioration using GPR wave attributes.

Figure 4.16 shows a typical result obtained from the survey carried out at the Praia do Futuro district residential building. Similarly with the other buildings deterioration is marked with reducing the depth of the reflector, increasing in the amplitude of EM waves and increasing in attenuation expressed by the dB decay.

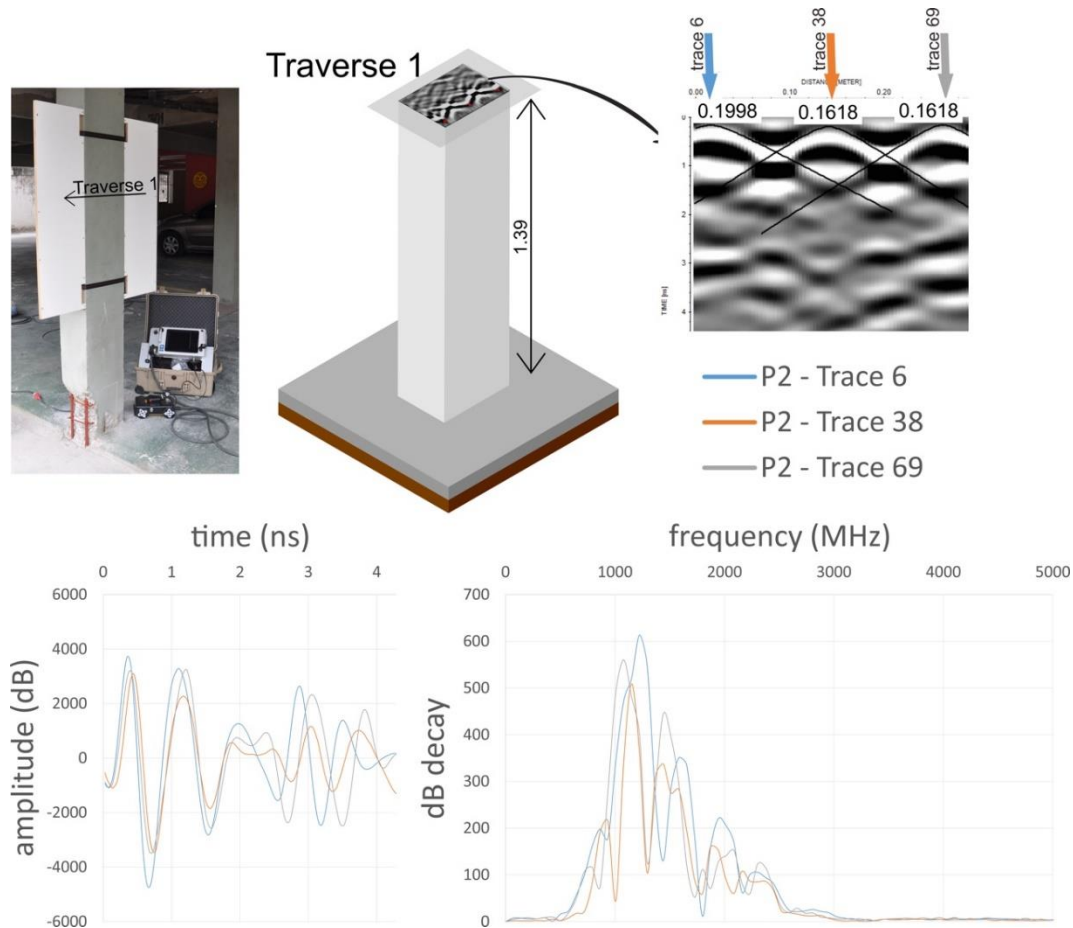


Figure 4.13. Attributes derived from the GPR scan carried out at column P2 from the Aldeota district building

As mentioned earlier, when a concrete structure is contaminated with chloride the conductivity is produced by the chloride dissolved in the pore water. As a consequence of the increase in chloride content, the GPR signal attenuation will also increase. When comparisons were made concerning this attribute, it is observed that attenuation values are higher at the Varjota district building as compared to the values found at the Aldeota district building. This behavior is related to the distance to the sea line for the sea breeze direction. However, signal attenuation values measured at the Praia do Futuro district building were the lowest even though this building was very close to the sea line. The lowest values could be credited to the placement of ceramic tiles on its columns that created an additional barrier against chloride-induced corrosion.

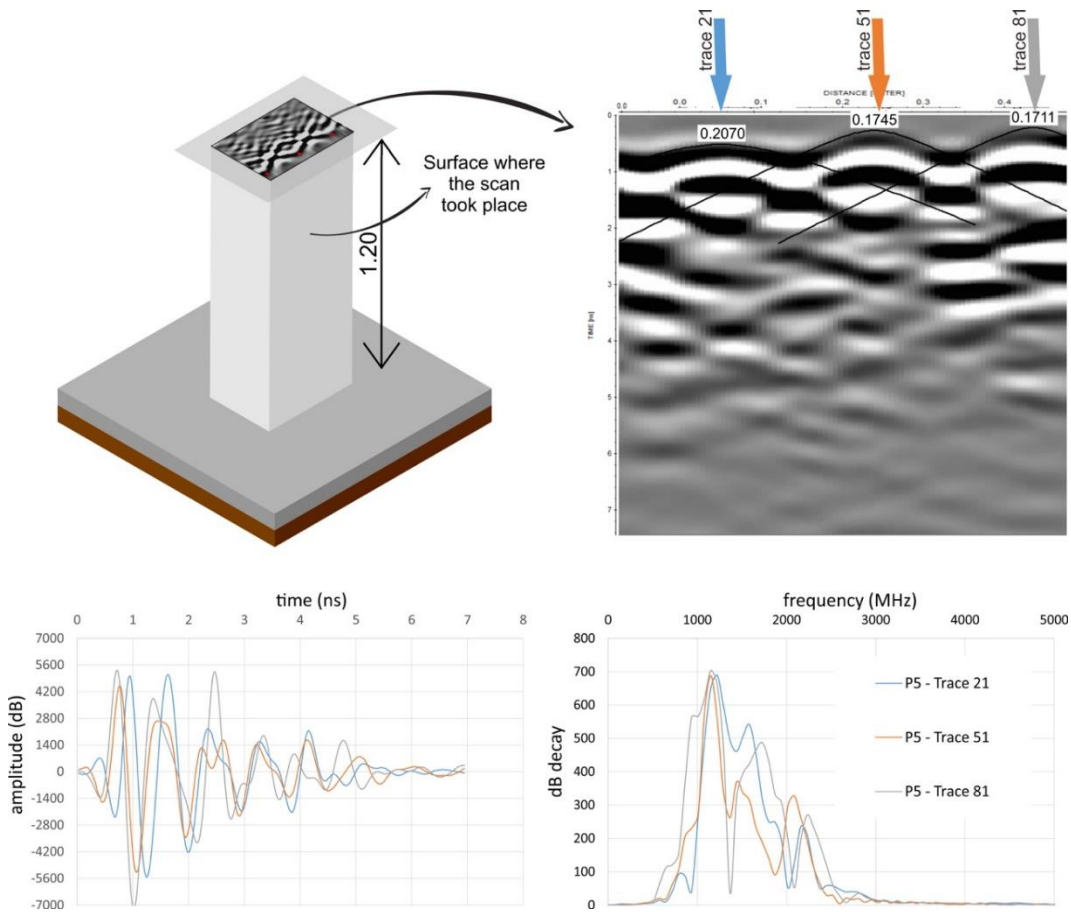


Figure 4.14. Attributes derived from the GPR scan carried out at column P5 from the Varjota district building

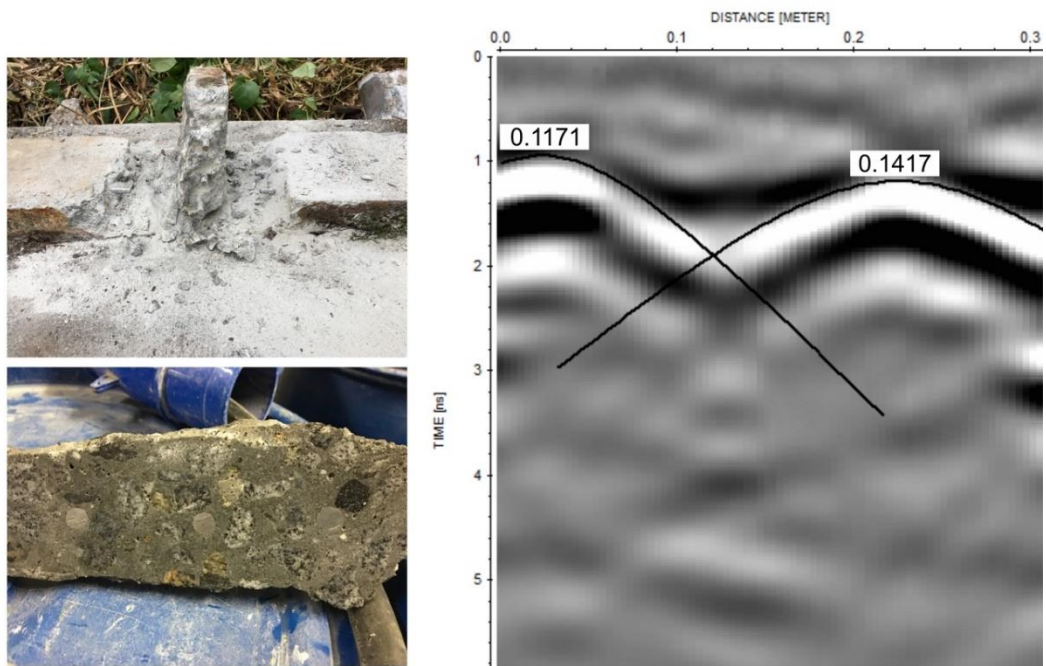


Figure 4.15. Position of rebars within the concrete composite slab showing embedded steel rebars possessing a different thickness of covering

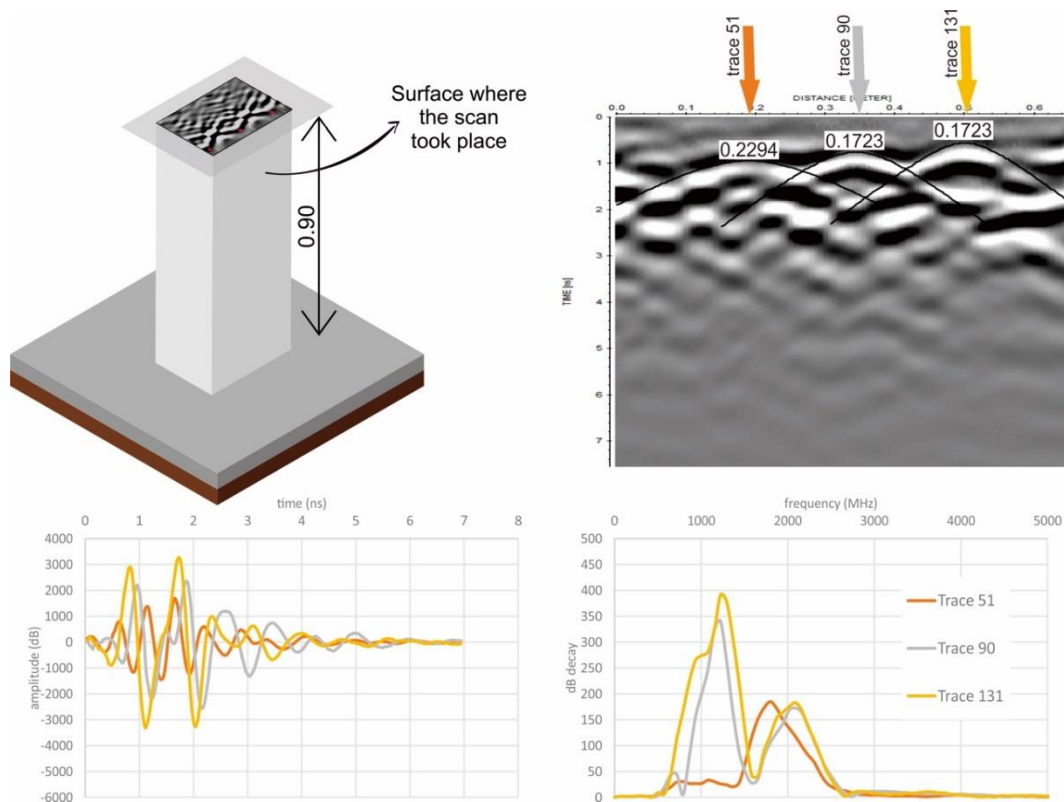


Figure 4.16. Attributes derived from the GPR scan carried out at column P1 from the Praia do Futuro district building

Concrete is a composite material constituted by a solid phase (i.e., mineral aggregate, hydrated components, anhydrous cement), a gaseous phase (i.e., air), and a liquid phase (i.e., pore solution). As stated before, permittivities of solid and gaseous phases are considered to be real numbers and permittivity of free water is considered a complex number since its molecules are free to rotate. Further to these, as Eq. 2.3 suggested, moisture in the concrete mass will attenuate the high-frequency component of the EM signal faster than the low-frequency component and will reduce the signal amplitude. Hence, it seems reasonable to assume that signal amplitude will also play an important role in assessing concrete deterioration. The results presented herein show that higher values of amplitude were determined on the Varjota district building followed by the Aldeota district building. Once again, values measured at the Praia do Futuro district building was the lowest and the ceramic covering played an important role in this behavior.

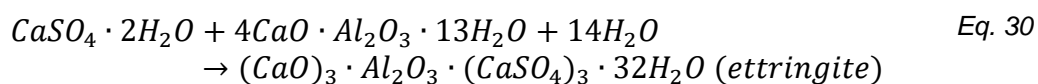
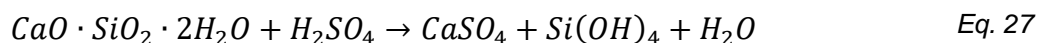
4.4 Conclusions

Chloride-induced corrosion on concrete structures constitutes a major cause of damages in residential buildings in coastal areas. In these areas, inspection should be considered any time when a structure shows signs of degradation as well as it is necessary to look for the best repair solution in order to reach their expected service life.

The results presented herein demonstrated that the ground-penetrating radar (GPR) is a rapid, non-destructive and non-invasive technique, which could be used as a useful tool in producing structural detailing drawings since it can provide the thickness of covering concrete and the depth and location of reinforcement. The results also show that deterioration of concrete mass and corrosion of its rebars could be also be assessed by the attributes provided by a GPR scan. Damages are detected with reducing the depth of the reflector, increasing in the amplitude of EM waves and increasing in attenuation expressed by the dB decay. Once the damage is detected, its effect on the integrity of a structure could be assessed by coring samples of concrete and/or steel rebars at the specific location given by the GPR and having the compressive strength of the concrete and the tensile strength of the rebar determined by conventional laboratory testing.

5 The use of ground penetrating radar in appraising the serviceability of a wastewater treatment plant concrete structure

Deterioration of sanitation facilities has caused not only loss of concrete mass but also structural capacity, ultimately leading to structural collapse (Jiang et al. 2015). Concrete deterioration in wastewater treatment systems is a result of a range of abiotic chemical reactions and biotic processes on the cementitious materials used in the production of concrete. According to Jiang et al. (2014a), concrete deterioration advances from carbonation (CO_2) and H_2S acidification during the initial stages that convert hydrated calcium silicate ($\text{CaO}\cdot\text{SiO}_2\cdot 2\text{H}_2\text{O}$) and portlandite ($\text{Ca}(\text{OH})_2$) into CaCO_3 , $\text{Ca}(\text{HS})_2$ and S_0 . These processes, as described by Joseph et al. (2012), reduce the pH of concrete from around 12 to 9, and provide favorable conditions to the biological production of sulfuric acid from oxidation of hydrogen sulfide present in the sewer gas phase during later stages. Jiang et al. (op. cit.) suggested that biotic processes, caused by bacteria and fungi, lead to the formation of two important corrosion products: gypsum and ettringite, according to the reactions below:



The authors also pointed out that gypsum and ettringite formation causes a volumetric expansion in the concrete mass. This process leads to internal cracking and pitting that exposes the concrete steel rebar for an acid attack as Figure 5.1 shows.

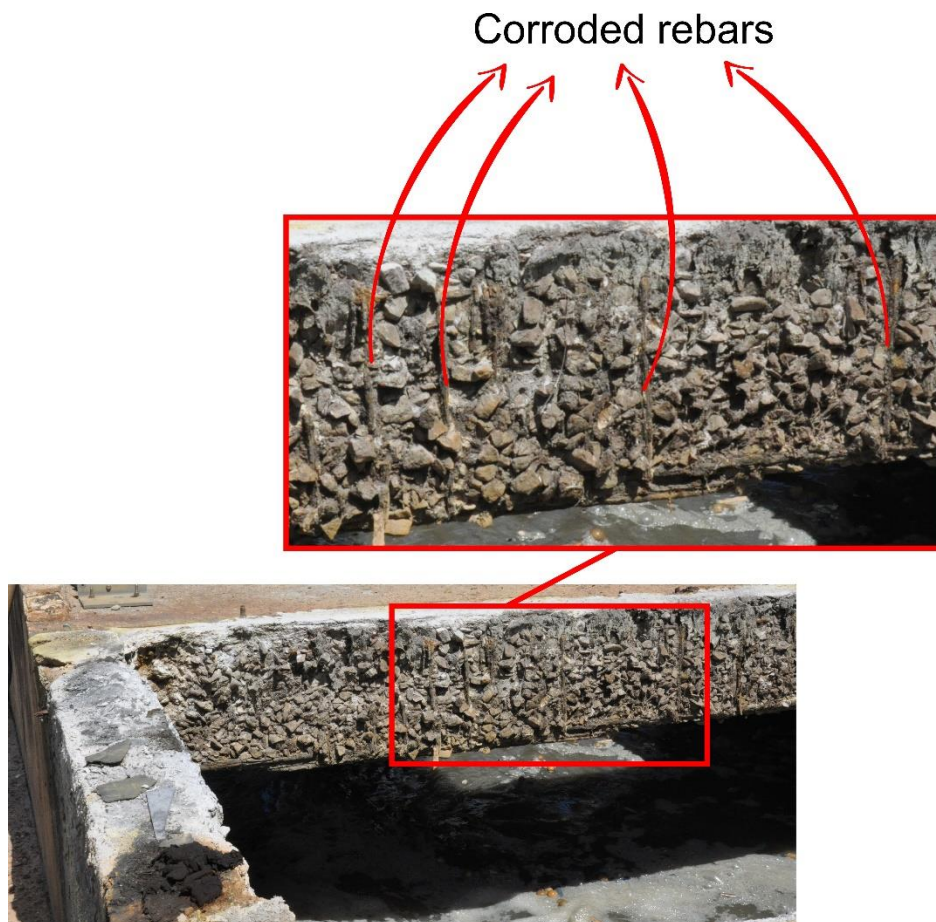
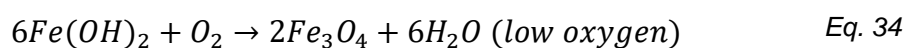
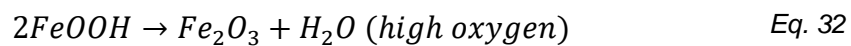


Figure 5.1. Steel rebar corrosion on a wastewater treatment facility

According to Song et al. (2019), the key corrosion process of rebar in concrete wastewater facilities likely conforms to the corrosion mechanisms shown in the reactions below:



Ideally, as Hui and Jinping (2011) suggested, a structure should meet the requirement of safety, durability, serviceability, and sustainability for long-term

operation. But this is not often the case in wastewater treatment systems. Grengg et al. (2015) pointed out that the acid attack on concrete could significantly decrease the lifespan of concrete structures from 100 to 30-50 years. In severe environments, as described in Hubber et al. (2017), their lifespan could be reduced to 10 years.

Maintenance and rehabilitation of such damaged structures usually involve high costs. Several authors, including Sterling et al. (2010), Jiang et al. (2014b) and Sun et al. (2016), estimate that billions of dollars are spent worldwide annually on maintenance expenses on sanitation systems caused by concrete deterioration. Thus, the appropriate maintenance of structural integrity over their lifespans is required to minimize economic losses. Also, the use of non-destructive testing methods is imperative not only for evaluating their structural integrity but also to make informed decisions regarding their repair strategies.

The primary objective of the present investigation was to assess the feasibility of the ground penetrating radar (GPR) in aiding on the serviceability appraisal of wastewater treatment plant concrete structures. GPR is considered one of the most popular non-destructive testing methods adopted for infrastructure imaging because of its high resolution, effectiveness, and availability of real-time images. In accordance to Lai et al. (2018), GPR surveys could be used to map concrete deterioration and to serve as a decision-making tool for preventive/ad-hoc maintenance. Due to its minimal intrusion, GPR could be used without a major impact on wastewater treatment systems activities.

GPR is based on the propagation of electromagnetic (EM) waves in the microwave band of the radio spectrum. According to Annan (2009), the GPR principle is similar to seismic reflection. The difference arises from the fact the energy may be reflected at boundaries where subsurface electrical properties change rather than the change in mechanical properties associated with acoustic energy. GPR is a time-domain system that applies an impulse to the antenna, placed close to the air-ground interface, that creates and detects key electromagnetic fields. The GPR transmitter antenna translates the excitation voltage into a predictable temporal and spatial distributed field and the receiving antenna detects the temporal variation of a vector component of the EM field and translate it into a recordable signal. During a survey, a GPR transmitter emits through an antenna an

electromagnetic pulse source into the ground. When this pulse encounters a boundary between materials having different dielectric permittivity, it will be partially reflected or refracted back to the surface where a receiving antenna records the magnitude and arrival time of the returned pulse. In the case of wastewater treatment plants, a shield could be used to focus on direct EM signal through the concrete structure. Also, shielded antennas minimize the direct transmitter to receiver energy, minimize the energy that escapes into the air and minimizes external electromagnetic noise.

5.1 Study site

The investigated wastewater treatment plant is located in the city of Fortaleza in the north-eastern region of Brazil and began its operation in March 1998. In the plant, shown in Figure 5.2, seven drum screens are used to separate coarse materials, such as sanitation articles and other rubbishes, from 3 m³/s of wastewater. The material removed is washed and pressed and disposed of in the municipal solid waste landfill. Gases are collected at the drum screen facilities and treated using chemicals to neutralize the foul smell at the odor treatment facility. The screened wastewater is then pumped to grit removal units where heavy but fine material such as sand and gravel is removed from the wastewater. This material is also disposed of in the municipal solid waste landfill. The remaining sewage is disposed of on the ocean by a 3,330 m long pipeline at a depth of 16 m.



- 1 - pumping station 2 - sieving unit
 3 - grit removal unit 4 - odor treatment facility

Figure 5.2. The wastewater treatment plant under investigation

5.2 GPR survey

The GPR survey was carried out at the sieving unit to provide information regarding its repair strategies since pitting exposed the steel reinforcement of its concrete structures. When 2D and 3D data were acquired using a MALÅ CX GPR scanning system with a shielded 1.2 GHz center frequency, the concrete covering, the distance between rebars, and the slab thickness are referenced as shown in Figure 5.3.

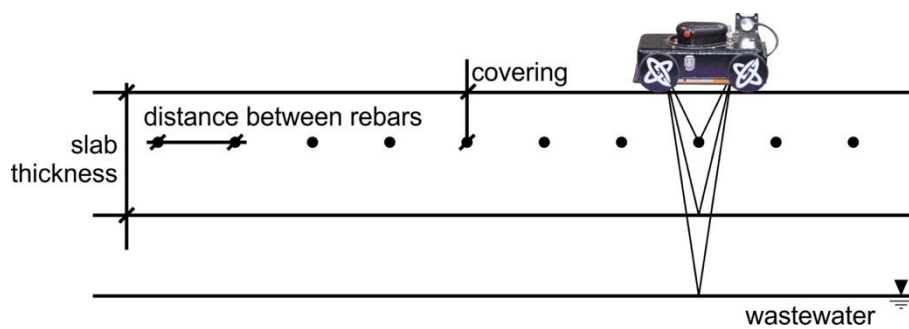


Figure 5.3. GPR survey targets

According to Pérez-Gracia et al. (2009), the shielded 1.2 GHz is a wideband frequency antenna, with bandwidth on the order of its nominal center frequency. The authors also stated that the fundamental wavelength of the emitted wave is about 18.8 cm and the separation between the receiver and the transmitter devices is 6 cm. The survey took place in the locations shown in Figure 5.4.

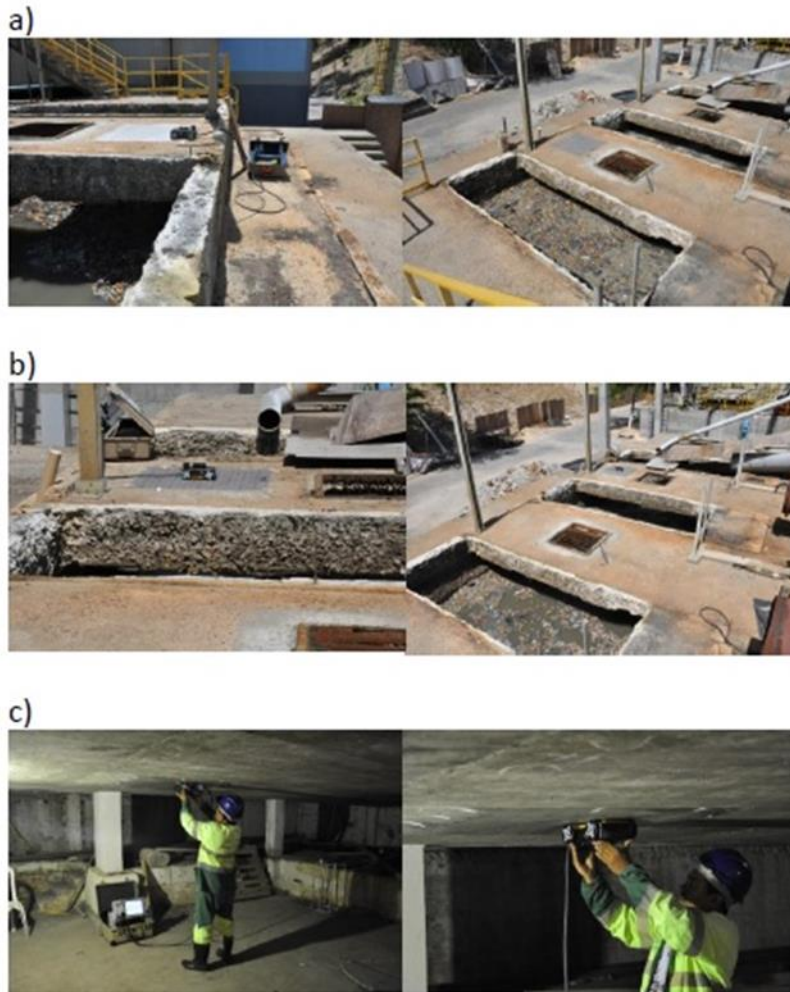


Figure 5.4. GPR survey at the sieving unit: a) cross-section on the sieving unit; b) slab between sieves #1 and #2; c) slab between sieves #2 and #3, and d) slab under sieves #4, #5, #6 and #7

The acquisition parameters can be summarized as follows:

- Trace length: 8.44 ns;
- Samples per trace: 313;
- Traces per meter: 260;
- Transmitter–receiver offset: 0.079 m, and
- Data processing during acquisition: none.

The GPR signal velocity was estimated from GPR profile data collected perpendicular to the slab rebars. The hyperbola fitting method available in the REFLEXW software version 9.0 (Sandmeier, 2019) was used to determine the signal velocity.

Data processing was carried out using REFLEXW software (Sandmeier, op. cit.), following recommendations given by Bennedeto et al. (2017), with the processing workflow shown in Figure 5.5.

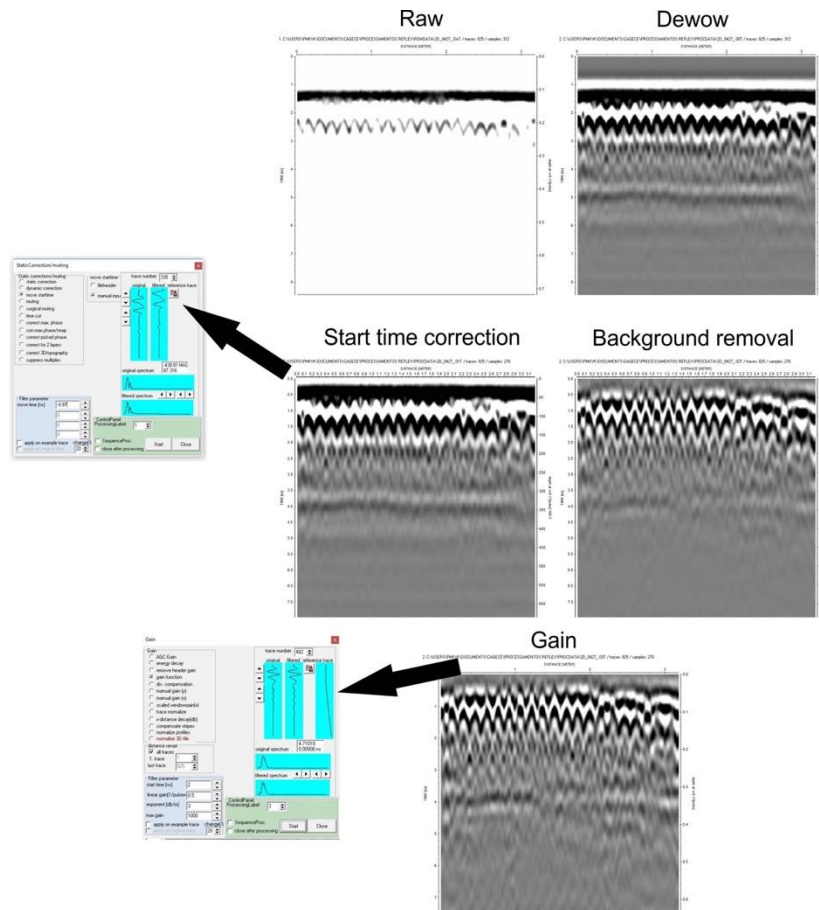


Figure 5.5. Data processing sequence

5.3 Results and discussion

GPR data are displayed in either greyscale and wiggle mode with two different configurations, as radargrams and as time slices. According to Hugenschmid and Mastrangelo (2006), radargrams consist of a large number of traces lined up according to their acquisition position, as sketched in Figure 5.6, where the antenna is moved in the x-direction recording data continuously. When data are acquired not only along single lines but covering a whole grid area, many parallel lines, slices from different times/depths are plotted as shown in Figure 5.7.

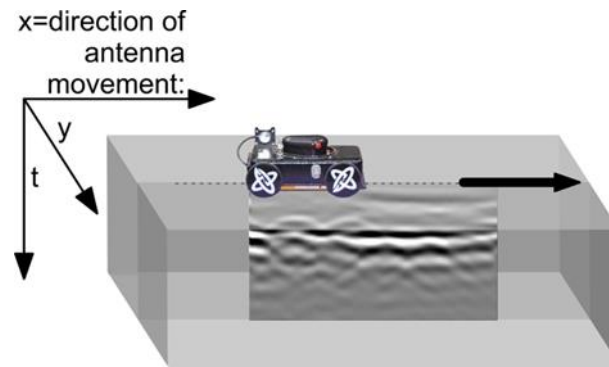


Figure 5.6. Schematic sketch of a radargram in greyscale mode

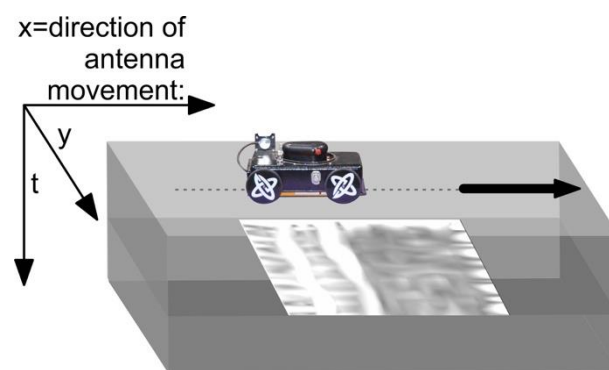


Figure 5.7. Schematic sketch of a time slice

The resulting representative hyperbolic curves of the slab upper rebars between sieves #1 and #2, sieves #2 and #3 and bottom slab on sieve #6 are shown in Figure 5.8. GPR signal velocities were estimated from profile data collected perpendicular to the slab rebars, following recommendations from Shihab and Al-Nuaimy (2005) and Zhou et al. (2018), using a plastic grid to increase measurement accuracy. It was also possible to detect the second set of hyperbolic curves shown in Figure 5.8a and Figure 5.8b. These hyperbolas belong from table tennis balls that were floating on the wastewater tank when the GPR survey took place as Figure 5.4b and Figure 5.4c show. These pieces of information were used to validate the position of the wastewater table on the tank.

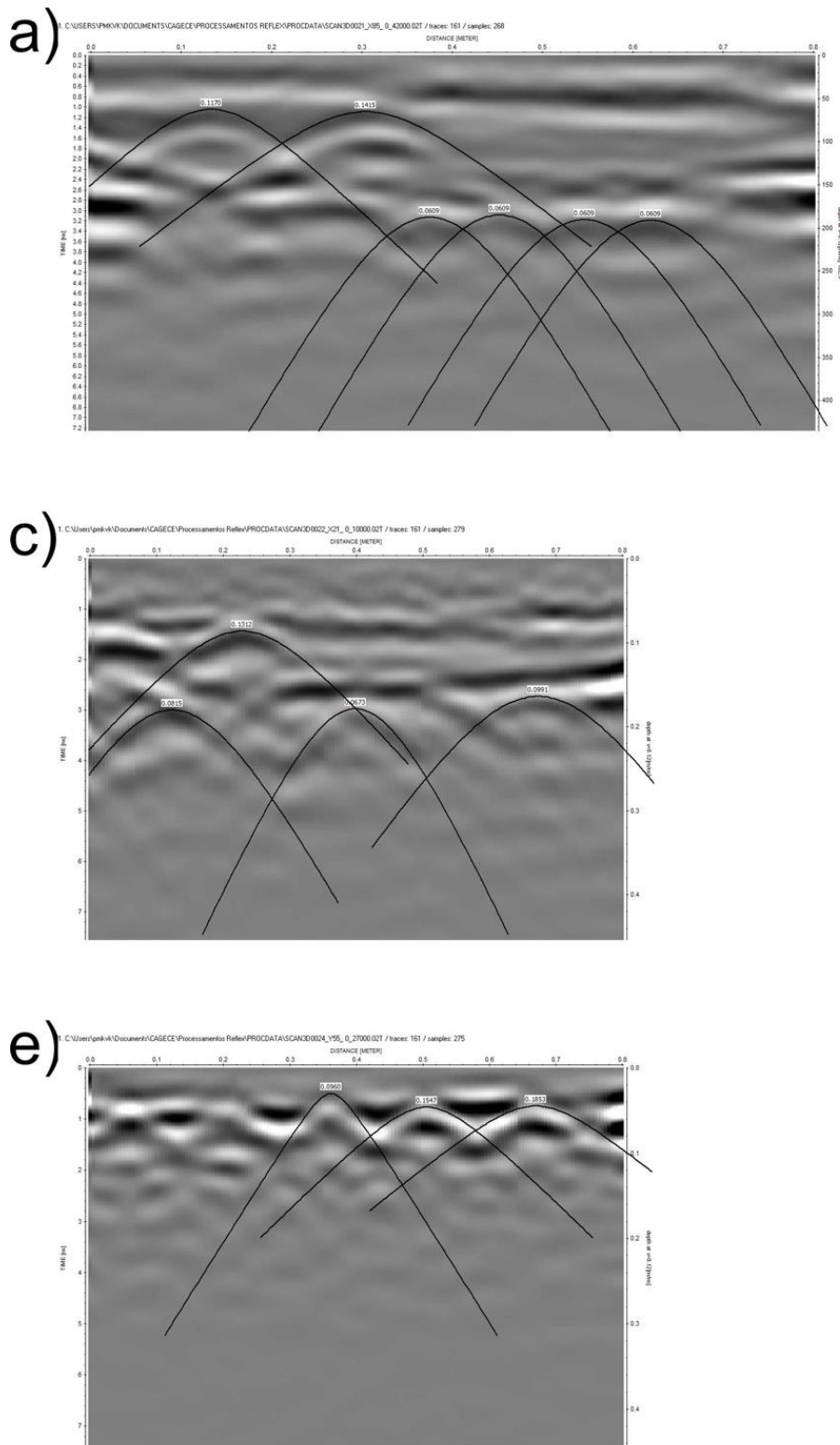


Figure 5.8. Hyperbolas on radargrams: a) upper slab between sieves #1 and #2; b) upper slab between sieves #2 and #3 and c) slab under sieves #4, #5, #6 and #7

The relative dielectric permittivity (k), as well as the vertical (r_{vertical}) and horizontal ($r_{\text{horizontal}}$) resolutions, were determined by multiple detections of the

traveling velocity of the GPR wave (v) in each surveyed slab as Figure 5.9 shows. The results indicate that the concrete medium in each slab is not uniform as denoted by changes in the traveling velocity of the GPR wave. In addition, the results have shown that GPR could be used to obtain accurate estimation of steel rebars since vertical and horizontal resolutions are smaller than the diameter of the rebars used in the upper slabs (i.e., 6.3 mm diameter) and the bottom slab (i.e., 10 mm diameter in the horizontal direction and 16 mm diameter in the vertical direction).

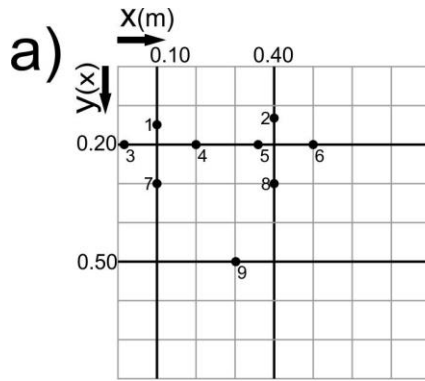
According to Jamil et al. (2013), concrete is considered as a dielectric material that stores energy when exposed to an electromagnetic signal. The authors also pointed out that the exposure of a dielectric material to an electromagnetic field, as in the case of a GPR survey, results in a change of the arrangements of its microscopic electric dipoles composed of positive and negative charges whose centers do not quite coincide. The authors mention that these are not free charges, and they cannot contribute to the conduction process since they are bound in place by atomic and molecular forces and can only shift position slightly in response to external fields. On the other hand, as indicated by Jamil et al. (op. cit.), free charges are the ones that determine conductivity.

Upon the exposure to an electromagnetic field during a GPR survey, a shift in the relative positions of the internal bound positive and negative charges against normal molecular and atomic forces results in the storage of electrical energy in what is known as polarization. The latter is expressed by the real part of the complex permittivity (or dielectric constant) of the material. As suggested by Kwon et al. (2010), the dielectric constant is a measure of how much energy from an external electric field is stored in a material. Jamil et al. (op. cit.), suggest that while the real part (dielectric constant) reflects the amount of polarization of the material, the imaginary part (or loss factor) reflects the losses caused by conductivity (controlled by free charges) and the relaxation of the water dipole. This is why a perfect dry dielectric material (with no free charges) would have an imaginary part of zero.

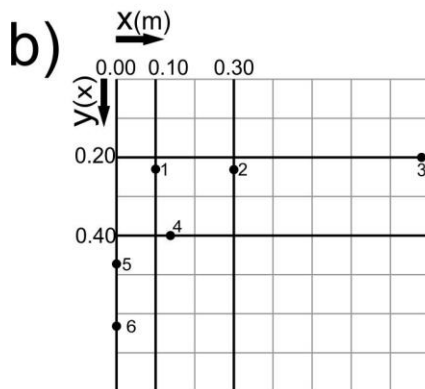
As the dielectric permittivity of water has a higher value than all other concrete constituents (aggregate and cement), the amount and state of water is the most significant factor in determining the dielectric properties of the concrete slabs at the Waste Water Treatment Plant Sieving Unit (WWTPSU). In accordance to

Lai et al. (2010), just after concrete mixing curing starts to allow continued absorption of water by cement to develop and formulate dense solid calcium silicate hydrates (C-S-H). The authors also pointed out that as the volume of C-S-H increases, the gel and capillary channels are blocked, segmented, and then isolated. Free water is reduced, absorbed, and bounded since water is hydrated to change from free to bound form.

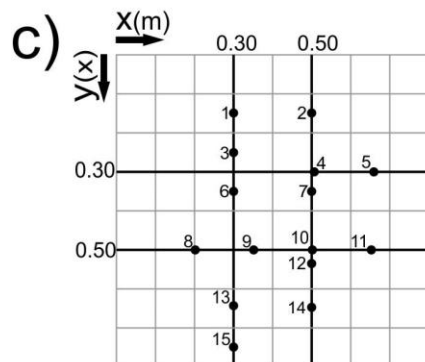
However, as in the case of the surveyed slabs of the WWTPSU, gypsum and ettringite formation caused a volumetric expansion in the concrete mass. Also, concrete was subjected to the cyclic drying-wetting salt-fog environment due to its proximity to the ocean. These processes led to internal cracking and pitting, and the pore sizes in the concrete mass became bigger in the upper slab between sieves #1 and #2 and in the upper slab between sieves #2 and #3, thus making it easier for the movement of free ionized water within the concrete slab. Therefore, the higher degree of saturation of concrete in those slabs leads to an increase in the measured values of dielectric constant as shown in Figure 5.9. The smaller measured values of the dielectric constant of the slab under sieves #4, #5, #6 and #7 were consistent with a concrete mass without cracking and pitting. It is also worth mentioning that this slab was protected from the salt-fog environment.



	v (m/ns)	k	rvertical (mm)	rhorizontal (mm)
1	0,13	5,33	0,04	4,02
2	0,12	6,57	0,04	3,67
3	0,11	7,34	0,03	3,50
4	0,12	5,90	0,04	3,84
5	0,11	7,06	0,03	3,56
6	0,11	7,34	0,03	3,50
7	0,15	4,23	0,04	4,42
8	0,14	4,49	0,04	4,31
9	0,17	3,26	0,05	4,89
MEAN	0,13	5,73	0,04	3,97
SD	0,02	1,49	0,01	0,49



	v (m/ns)	k	rvertical (mm)	rhorizontal (mm)
1	0,13	5,23	0,04	4,05
2	0,12	6,45	0,04	3,70
3	0,12	6,33	0,04	3,73
4	0,13	5,08	0,04	4,10
5	0,15	4,10	0,04	4,47
6	0,15	4,10	0,04	4,47
MEAN	0,13	5,22	0,04	4,08
SD	0,01	1,03	0,00	0,34



	v (m/ns)	k	rvertical (mm)	rhorizontal (mm)
1	0,15	3,83	0,05	4,59
2	0,17	3,08	0,05	5,00
3	0,15	3,83	0,05	4,59
4	0,15	3,76	0,05	4,63
5	0,18	2,62	0,06	5,31
6	0,15	3,83	0,05	4,59
7	0,17	3,08	0,05	5,00
8	0,17	3,27	0,05	4,89
9	0,12	5,80	0,04	3,87
10	0,11	7,60	0,03	3,44
11	0,14	4,29	0,04	4,39
12	0,20	2,21	0,06	5,64
13	0,15	3,83	0,05	4,59
14	0,14	4,51	0,04	4,30
15	0,15	3,83	0,05	4,59
MEAN	0,15	3,96	0,05	4,63
SD	0,02	1,31	0,00	0,53

Figure 5.9. GPR survey determined parameters: a) upper slab between sieves #1 and #2; b) upper slab between sieves #2 and #3 and c) slab under sieves #4, #5, #6 and #7

Concrete deterioration was also appraised by analyzing the amplitude of electromagnetic waves measured during the GPR surveys on each slab. The results are presented in Figure 5.10.

According to Sbartai et al. (2006), the amplitude of EM waves depends on the attenuation that takes place during their propagation. The authors pointed out that attenuation of EM waves in concrete results from two mechanisms: 1) absorption of EM energy due to dipole polarization (the rotation movement of permanent dipoles such as water molecules) and ionic conduction (the displacement of anions and cations in the liquid phase); and 2) geometrical attenuation, which is related to the variation of the radiation pattern of the antenna due to a change in the dielectric constant.

Figure 5.10 shows that the increase in the degree of saturation of concrete, caused by a salt-fog environment allied to the internal cracking and pitting caused by gypsum and ettringite formation, lead to a decrease in the aperture of radiation pattern and the amplitude of the direct wave signal. The results show smaller values of amplitude on the scans of the upper slab between sieve #1 and #2 (Figure 5.10a) and the upper slab between sieve #2 and #3 (Figure 5.10b) when compared to those measured at the slab under sieves #4, #5, #6 and #7 (Figure 5.10c).

The amplitude of EM waves seems to be a good indicator to assess deterioration on a concrete mass as Figure 5.11 shows. This figure, a result from a GPR scan on the slab between sieve #1 and #2, shows a zone of different attenuation pattern of EM waves between 0.2 m and 0.4 m (Figure 5.11a). When wiggles representing different portions of the concrete slab are superimposed to the radargram as depicted in Figure 5.11b, it is possible to see that the amplitude of EM wave is close to zero in the zone with different attenuation pattern. When the magnitude of the amplitude of EM waves is compared as shown in Figure 5.11c, one can see that the amplitude of the EM wave is very similar in different regions of the slab.

In fact, as Figure 5.12 shows, the resulting amplitudes of EM waves from a GPR scan on the bottom slab of sieve #6 indicate values very close to each other. They suggest a more uniform structure free from corrosion caused by a salt-fog environment, which was supported by a slow deteriorating process in its performance due to abiotic chemical reactions and biotic processes on the cementitious materials.

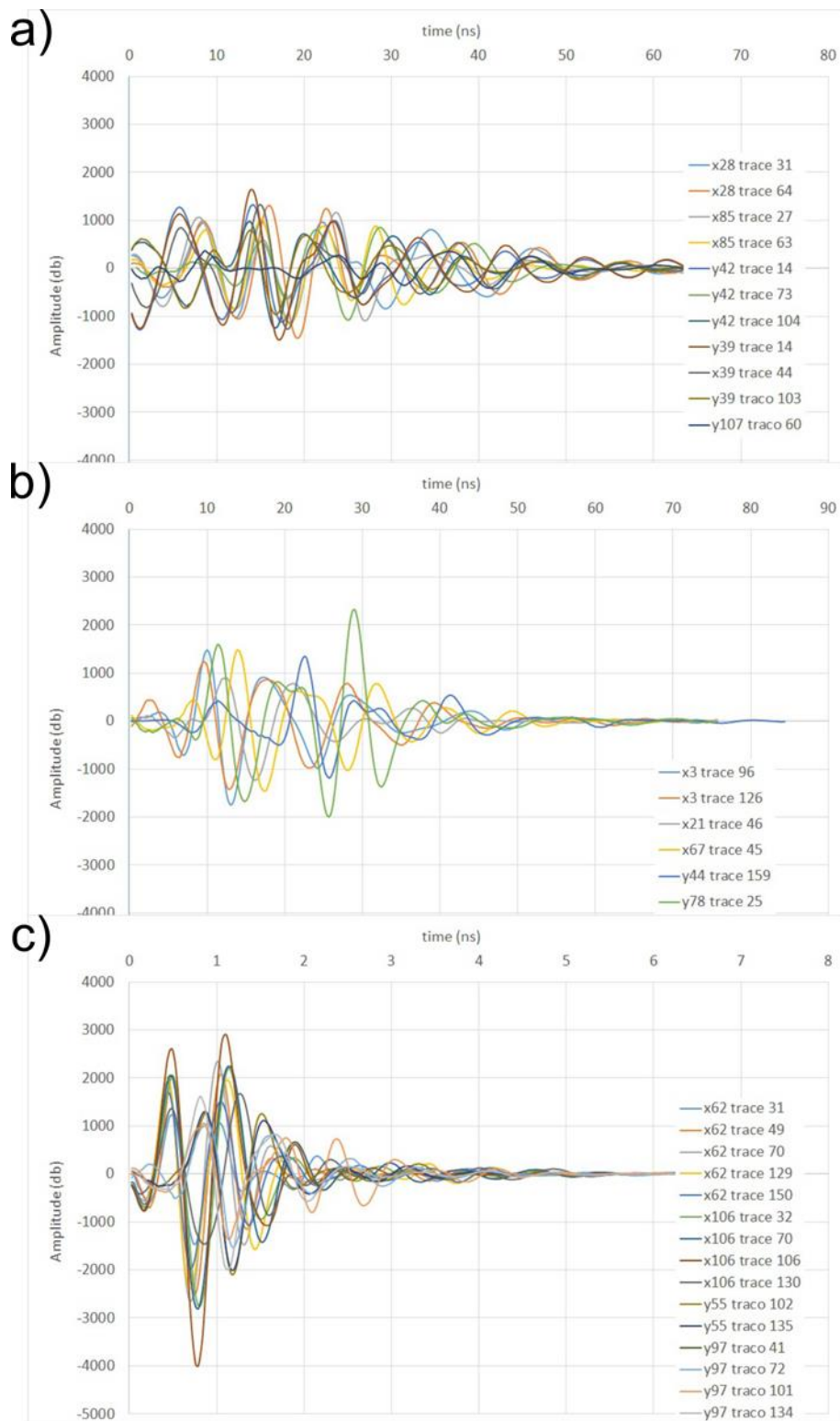


Figure 5.10. Amplitude of EM waves: a) a) upper slab between sieves #1 and #2; b) upper slab between sieves #2 and #3 and c) slab under sieves #4, #5, #6 and #7

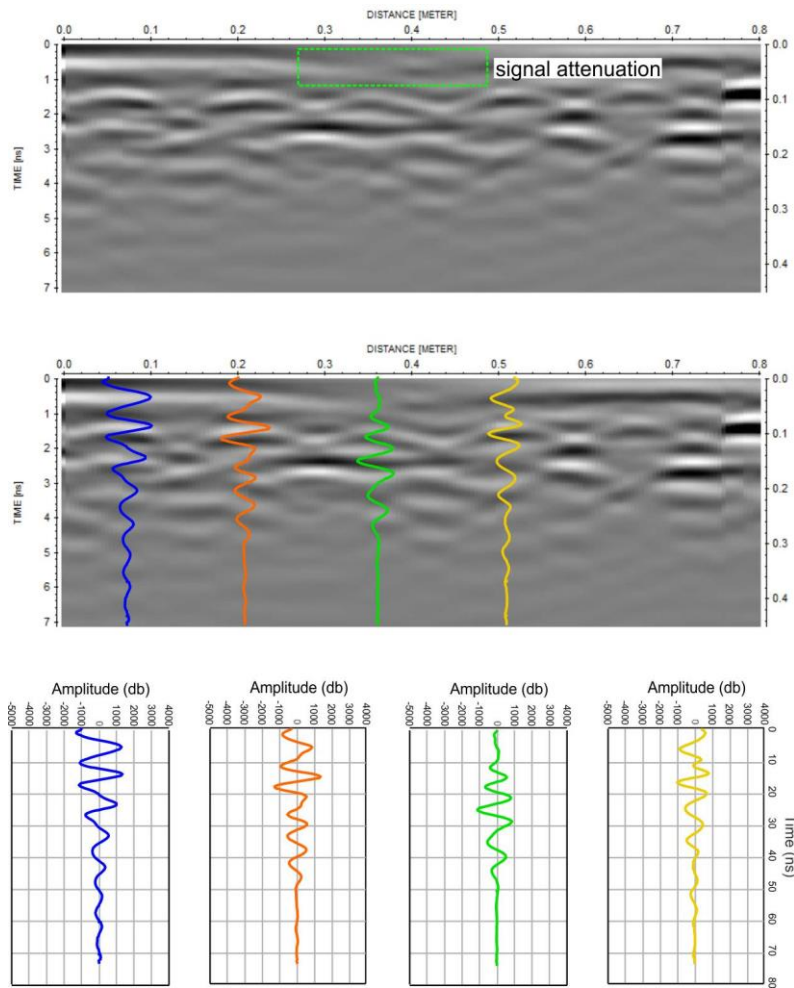


Figure 5.11. GPR scan on the slab between sieve #1 and #2

The health of the rebars was assessed through the information provided by slices from different times/depths provided by 3-D surveys covering a 0.8 m x 0.8 m grid area. The information related to the upper slabs investigated is shown in Figure 5.13 and 3.14. In these figures, the reinforcement detailing is shown on the left side and the slices are on the right. The contour of the 0.8 m x 0.8 m grid area is denoted by the red square. The position of the localized reinforcement is denoted by the green dotted rectangles and the transverse slab reinforcement bars are represented by the white portions of the slice.

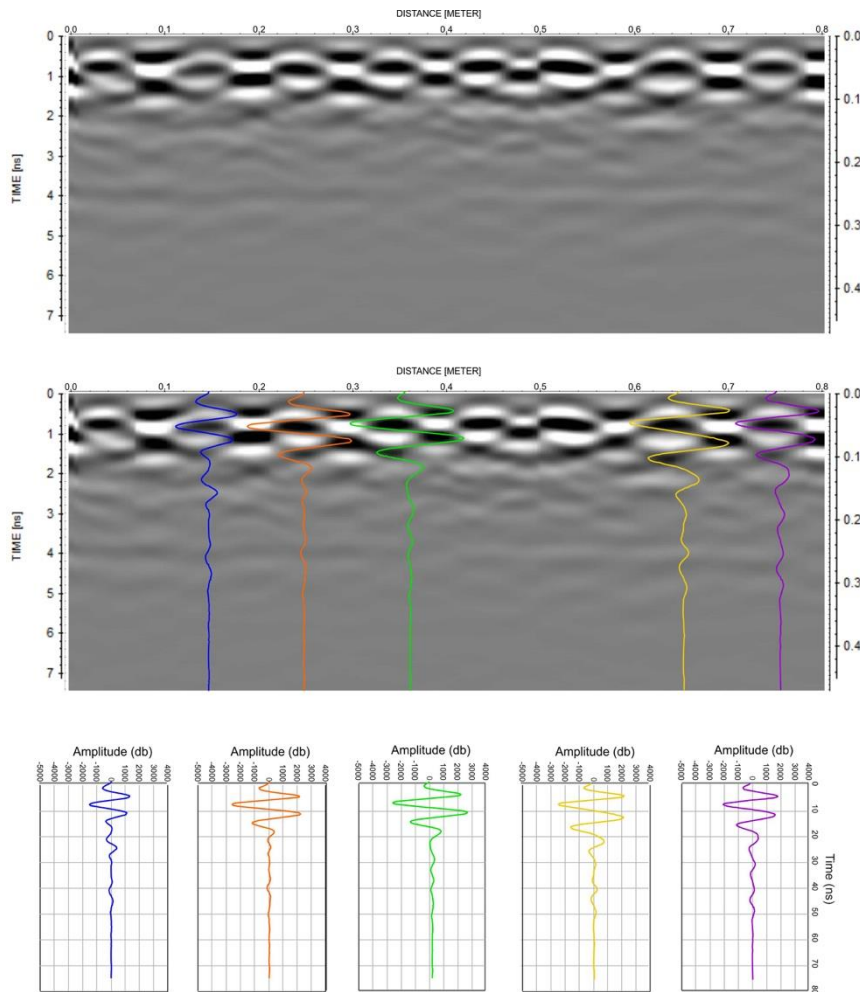


Figure 5.12. GPR scan on the slab under sieves #4, #5, #6 and #7

The time slice shown in Figure 5.13 indicates the presence and pattern of two transverse slab rebars spaced circa 15 cm from each other and the localized longitudinal rebars. The survey did not detect the remaining transverse slab rebars whose positions are delineated by the blue dotted lines. The fact that these rebars were not detected on the radargrams of the 2-D surveys carried out in the same position suggests that severe corrosion took place. This region of the slab suffered more from the sulfuric acid attack from the oxidation of hydrogen sulfide present in the wastewater gas phase due to the presence of the nearby window as Figure 5.14 shows.

A similar pattern was observed on the slice representing the 3-D survey carried out at the upper slab between sieve #2 and #3. The localized rebars were detected in both longitudinal and transverse directions with spacing similar to that

specified on the reinforcement detailing drawing. The difference arose from the fact that just one transverse slab rebar was detected together with a longitudinal rebar. The higher degree of corrosion detected in this slab could be attributed to the greater turbulence on the wastewater flow below it that provided a more intense sulfuric acid attack.

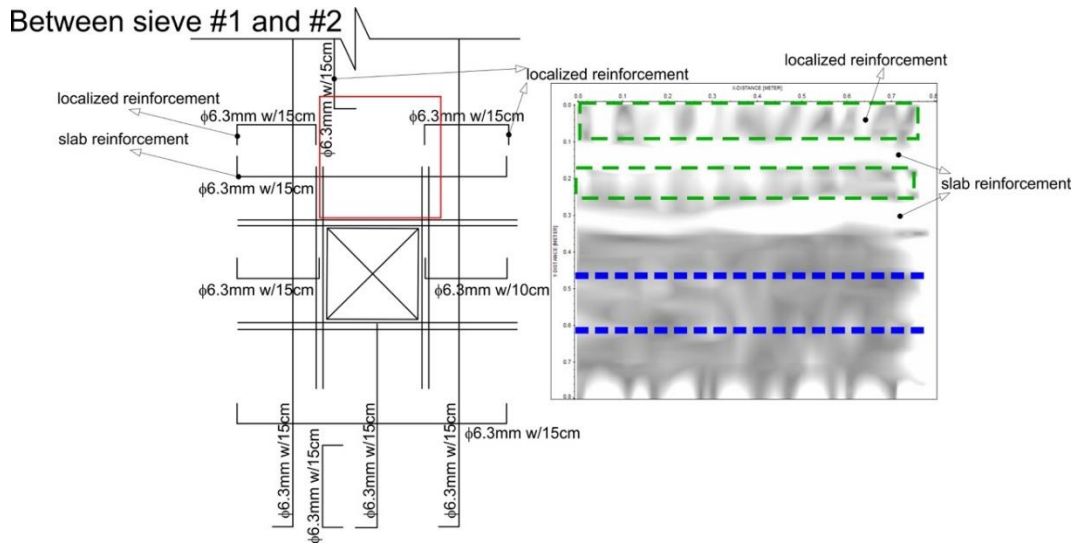


Figure 5.13. Time slice showing rebars in the slab between sieve #1 and #2

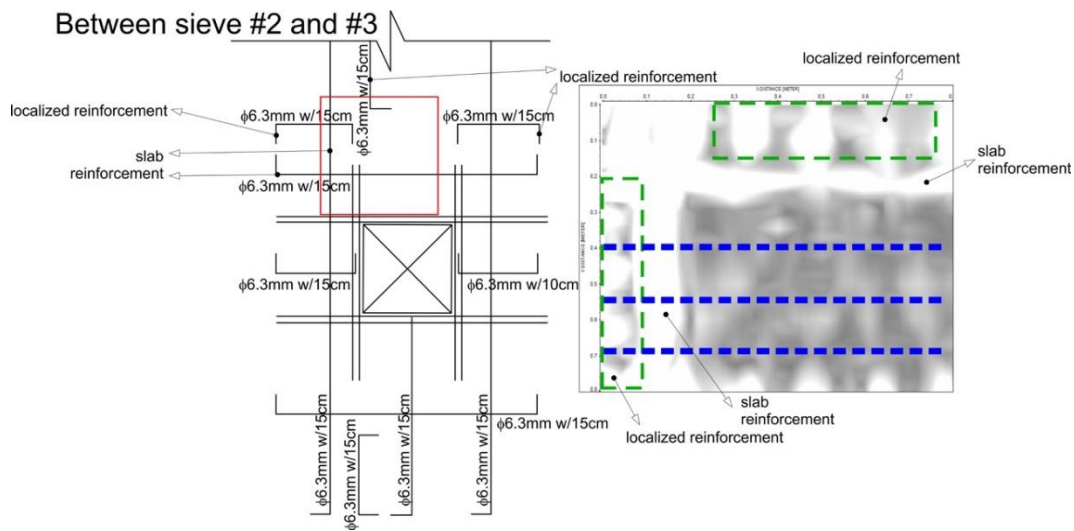


Figure 5.14. Time slice showing rebars in the slab between sieve #2 and #3



Figure 5.15. Position where the 3-D survey took place on the slab between sieve #2 and #3

For a matter of comparison, Figure 5.16 shows a time slice where a GPR survey was performed on the slab under sieves #4, #5, #6 and #7. This slab presented a lesser degree of corrosion as it was found based on the results from the dielectric permittivity and the amplitude of EM waves. The position where the survey took place is denoted by the red square on the reinforcement detailing drawing. It is clear on the time slice the presence and pattern of transverse and longitudinal rebars corroborating the findings from the other parameters investigated herein.

PUC-Rio - Certificação Digital Nº 1521883/CA

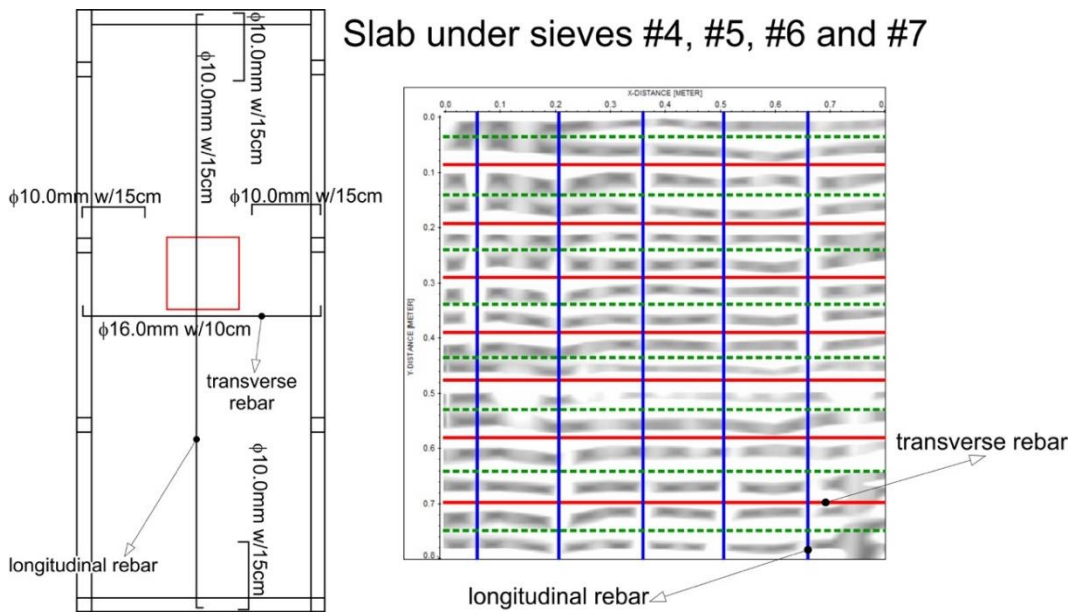


Figure 5.16. Time slice showing rebars in the slab under sieves #4, #5, #6 and #7

5.4 Conclusions

A GPR survey was carried out aiming at detecting anomalies on the concrete structure of a wastewater treatment plant sieving unit. This unit had its concrete structure exposed to sulfuric acid attack from the oxidation of hydrogen sulfide present in the wastewater gas phase and subjected to the cyclic drying-wetting salt-fog environment due to its proximity to the ocean. As a consequence, volumetric expansion in the concrete mass took place due to the gypsum and ettringite formation in the process of rebar corrosion.

The results presented herein suggest that the amplitude of EM waves from a GPR scan as well as the determined values of dielectric permittivity can be used to monitor concrete deterioration in a structure in such a way that any growth of inherent faults would be immediately detectable. The results also indicate that the health of the rebars could be assessed through the information provided by slices from different times/depths obtained from a 3-D survey.

Further to these, GPR seems to be a valuable tool to locate an anomaly and infer its severity so that decisions can be easily made as to which actions need to be taken next (e.g., mandatory closure, immediate repair, etc.). In the case of the present investigation, it was suggested to the owner of the wastewater treatment plant to demolish the upper slabs and preserve the bottom slabs of the sieving unit.

6 Conclusions

This thesis presented the experimental issues concerning the health assessment of concrete structures with the desire to replace the traditional subjective assessment of civil structures with a more objective assessment using the GPR. The emphasis here was on validating a sound procedure of health assessment for concrete test specimens, buildings, and wastewater treatment stations. GPR was chosen since it is considered one of the most popular non-destructive testing methods adopted for concrete structure imaging because of its relative insensitivity to ambient conditions, high resolution, effectiveness, and availability of real-time images. The research carried out in this thesis emphasized on as-built designing, damage detection, location, and quantification, which is of interest in the context of structural control.

To achieve the objective of this thesis it was necessary to design an experimental program that included laboratory work and field surveys. The laboratory research program was performed at the Materials and Structures Laboratory where there is a strong research group dedicated to composite materials. It was chosen to carry out the fieldwork at the city of Fortaleza, in the State of Ceará - Brazil, since the high charge of marine aerosols has been deteriorating residential buildings over the past decades and one of its wastewater treatment plant stations was about to enroll on a maintenance process and there was a need to provide informed decisions regarding its repair strategy.

Results from self-consolidating cured casted short beams revealed that the distribution of steel fibers within a beam is not uniform. Digital and processed images showed that fibers are not evenly distributed and there is a disparity between the numbers of fibers in different sections of the short beam. A statistical analysis performed on the results also found that the distance between fibers also varies within the short beam. When sketches of the emitted and recorded GPR signal in a single radar trace mode are compared to the digital and processed images it was perceived a good relationship between the GPR signal and the distribution of steel

fibers within the short beam. It was additionally noticed that GPR signal amplitude not only supplies information on how the fibers are close to each other but also reflects regions with an absence of fibers. Results have also shown that a GPR system using a high-frequency antenna could assess weaker zones of steel fiber reinforcement within self-consolidating concrete short beams.

It was found during inspections to choose the residential building to compose the subject of this study that chloride-induced corrosion on concrete structures constitutes a major cause of damages in residential buildings in Fortaleza. Based on interviews with several structural consultants, it was clear that inspection should be considered any time when a structure shows signs of degradation as well as it is necessary to look for the best repair solution in order to reach their expected service life. The results presented in this thesis demonstrated that the ground-penetrating radar (GPR) is a rapid, non-destructive and non-invasive technique, which could be used as a useful tool in producing structural detailing drawings since it can provide the thickness of covering concrete and the depth and location of reinforcement. The results also show that deterioration of concrete mass and corrosion of its rebars could also be assessed by the attributes provided by a GPR scan. Damages are detected by reducing the depth of the reflector, increasing the amplitude of EM waves and increasing attenuation expressed by the dB decay.

It was also found during the experimental fieldwork in Fortaleza that wastewater treatment plants also experience a great deal of deterioration in their structures due to rebar corrosion in concrete. Their structures are exposed to the sulfuric acid attack from the oxidation of hydrogen sulfide present in the wastewater gas phase and subjected to the cyclic dry-wet salt-fog environment due to its proximity to the sea line. The results from the field survey suggest that the amplitude of electromagnetic waves from a GPR scan and the determined dielectric permittivity values can be used to monitor steel rebar corrosion in a concrete structure by rapidly detecting any growth of inherent faults. The results also indicate that the rebar condition can be assessed through slices at different times/depths obtained from a 3-D survey.

As a matter of fact, researches in carbon dioxide, chloride- and sulfur-induced concrete deterioration are still prosperous, due to the emergence of new cement-

based materials and the complexity in modern engineering practices. Despite the growing interest in the long-term durability assessment draws more attention to the computational investigation, there is an increasing need to develop new experimental techniques. The challenge lies in combining investigative tools that could detect, locate and quantify structural damage as well as to detect multi-ionic species, moisture and heat that are involved in the multi-species transportation process of chloride, sulfur and carbon dioxide.

References

- Al-Nuaimy, W.; Huang, Y; Nakhkash, M.; Fang, M. T. C.; Nguyen, V. T.; Eriksen, A. (2000). Automatic detection of buried utilities and solid objects with GPR using neural networks and pattern recognition. *Journal of Applied Geophysics*. v. 43, 157-165.
- Alani, A.M. and Tosti, F. (2018). GPR applications in structural detailing of a major tunnel using different frequency antenna systems. *Construction and Building Materials* 158, 1111–1122.
- Alani AM, Aboutalebi M, Kilic G. (2013) Applications of ground penetrating radar (GPR) in bridge deck monitoring and assessment. *Journal of Applied Geophysics* 97:45–54. doi: 10.1016/j.jappgeo.2013.04.009.
- Anderson, N. L., Torgashov, E., & Kovin, O. (2010). Ground Penetrating Radar: Utility/Rebar/Cable Detection and Concrete/Subgrade Debonding. *Symposium on the Application of Geophysics to Engineering and Environmental Problems 2010*. doi:10.4133/1.3445546
- Angers, J. (2001). As-built drawings: As good as gold. *American Water Works Association Journal* 93(12), 46-48.
- Annan, A.P. (2001) *Ground Penetrating Radar Workshop Notes*. Sensors & Software Inc. 192p.
- Annan, A.P. (2005). GPR methods for hydrogeological studies. In *Hydrogeophysics* (eds. Y. Rubin and S. S. Hubbard), Springer, Dordrecht.
- Annan, A.P. (2009). *Ground Penetrating Radar (GPR) Principles*. In: *Ground Penetrating Radar: Theory and Principles* (edited by R.M. Jol), Elsevier Science, Oxford.
- Ansell, A. (2010). Investigation of shrinkage cracking in shotcrete on tunnel drains. *Tunneling and Underground Space Technology* 25, 607-613.
- Barnett, S.J., Lataste, J-F., Parry, T., Millard, S.G., and Soutsos, M.N. (2009) Assessment of fibre orientation in ultra-high performance fibre reinforced concrete and its effect on flexural strength. *Mater Struct*;43(7):1009–23.
- Barraca. N., Almeida, M., Varum, H., Almeida, F., Matias, M. S. (2016) A case study of the use of GPR for rehabilitation of a classified Art Deco building: the Inova Domus house. *Journal of Applied Geophysics* 127, 1–13.

- Barrile, V. and Pucinotti, R. (2005) Application of radar technology to reinforced concrete structures: a case study. *NDT E International* 38, 596–604.
- Battista, B. M., Addison, A. D., and Knapp, C. C. (2009) Empirical Mode Decomposition Operator for Dewowing GPR Data. *Journal of Environmental & Engineering Geophysics* 14, 163-169.
- Behar, V., Vassileva, B., and Kabakchiev, C. (2008) A Software Tool for GPR Data Simulation and Basic Processing. *Cybernetic and Information Technologies* 8(4), 69-76.
- Benedetto A. (2013) A three dimensional approach for tracking cracks in bridges using GPR. *Journal of Applied Geophysics* 97, 37–44.
- Benedetto, F. and Tosti, F. (2017). A signal processing methodology for assessing the performance of ASTM standard test methods for GPR systems. *Signal Processing* 132, 327–337.
- Benedetto, A., Tosti, F., Ciampoli, L.B., and D’Amico, F. (2017). An overview of ground-penetrating radar signal processing techniques for road inspections. *Signal Processing* 132, 201–209.
- Bertolini, L., Elsener, B., Pedferri, P., Redaelli, E., and Polder, R. (2013). *Corrosion of Steel in Concrete: Prevention, Diagnosis, Repair (Second Edition)*. Wiley-VCH Verlag GmbH & Co, Weinheim, Germany, 414 pp.
- Bordelon, A.C., and Roesler, J.R. (2014). Spatial distribution of synthetic fibers in concrete with Xray computed tomography. *Cement and Concrete Composites* 53, 35–43.
- Burger, H.R. (1992): *Exploration Geophysics of the Shallow Subsurface*. Englewood Cliffs, New Jersey, Print Hall, pp. 489.
- Cabral, A.E.B. and Campos, A.M.R. (2016). Study on Air Aggressiveness in Fortaleza/CE (in Portuguese). Graduate Program in Civil Engineering. Federal University of Ceará, 98 pp. Available at <http://www.pec.ufc.br/images/Edital/16-11-Cartilha-Agressividade-do-Ar-Small-Spreads.pdf>
- Candella, R.N. (2019). Characteristics of ocean waves of Fortaleza, CE, Brazil, extracted from 1-year deep-water measured data. *Ocean Dynamics* 69, 1239–1251.
- Cassidy, N. J., Eddies, R., & Dods, S. (2011). Void detection beneath reinforced concrete sections: The practical application of ground-penetrating radar and ultrasonic techniques. *Journal of Applied Geophysics*, 74(4), 263-276.
- Cattaneo, S., Francesca Giussani, F., and Mola. F. (2012) Flexural behavior of reinforced, prestressed and composite self-consolidating concrete beams. *Construction and Building Materials* 36, 826–837.

- Cavalaro, S.H.P., Lopez, R., Torrents, J.M., and Aguado, A. (2014). Improved assessment of fibre content and orientation with inductive method in SFRC. *Material Structures* .
- Cavalaro, S.H.P., Torrents, J.M., and Aguado, A. (2015) Assessment of fibre content and 3D profile in cylindrical SFRC specimens. *Material Structures*.
- Chang, C. W., Lin, C. H., and Lien, H. S. (2009). Measurement radius of reinforcing steel bar in concrete using digital image GPR. *Construction and Building Materials* 23(2), 1057-1063.
- Cintra, D.C.B. (2019). Methodologies for assessing the structural integrity of historical shells. D.Sc. Thesis, Graduate Program in Civil Engineering, Pontifical Catholic University of Rio de Janeiro, 226 p.
- Clipper Controls (2019). Dielectric Constants of Various Materials. Available at <http://www.clippercontrols.com/pages/Dielectric-Constant-Values.html>.
- Conyers, L.B. and Goodman, D. (1997). *Ground-Penetrating Radar: an Introduction for Archaeologist*, AltaMira Press, London.
- Cross, E.J., Worden, K., and Farrar, C.R. (2013). Structural Health Monitoring for Civil Infrastructure. In *Health Assessment of Engineered Structures: Bridges, Buildings and Other Infrastructures*. World Scientific Publishing Company, Singapore, 1-31.
- Daniels, D. J. (2007). *Ground Penetrating Radar (2nd. Edition)*. The Institute of Engineering and Technology, London.
- Davis, J.L. and Annan, A.P. (1989): Ground penetrating radar for high-resolution mapping of soil and rock stratigraphy, *Geophysics Prospect* 37 (4), 531-551.
- Faifer, M., Ottoboni, R., Toscani, S., Ferrara, L. and Felicetti, R. (2009) A multi-electrode measurement system for steel fiber reinforced concrete materials monitoring. In: *Proceedings to IEEE International Instrumentation and Measurement Technology Conference*, Singapore, 303–308.
- Faifer, M., Ottoboni, R., Toscani, S. and Ferrara, L. (2011) Nondestructive testing of steel-fiber reinforced concrete using a magnetic approach. *IEEE Transactions of Instrumentation and Measurements* 60(5),1709–1717.
- Faifer, M., Ottoboni, R, Toscani S, Ferrara L. (2012) An improved method for steel fiber reinforced concrete analysis. *Proceeding of IEEE International Instrumentation and Measurement Technology Conference*, Graz, Austria, 1896–1901.
- Ferrara, L., Faifer, M. and Toscani, S. (2012) A magnetic method for non-destructive monitoring of fiber dispersion and orientation in steel fiber reinforced cementitious composites. Part 1: method calibration. *Materials and Structures* 45, 575–89.

- Gargoum, S.A., El-Basyouny, K., Shalkamy, A., and Gouda, M. (2018). Feasibility of extracting highway vertical profiles from LiDAR Data. *Canadian Journal of Civil Engineering* 45, 418–421.
- Gettu, R., Gardner, D.R., Saldivar, H., and Barragán, B.E., (2005) Study of the distribution and orientation of fibers in SFRC specimens. *Materials and Structures* 38, 31–37.
- Gonzalez-Drigo, R., Perez-Gracia, V., Di Capua, D. and Pujades, L.G. (2008) GPR survey applied to modernists buildings in Barcelona: the cultural heritage of the College of Industrial Engineering. *Journal of Cultural Heritage* 9, 196–202.
- Grengg, C., Mittermayr, F., Baldermann, A., Böttcher, M.E., Leis, A., Koraimann, G., Grunert, P., and Dietzel, M., (2015) Microbiologically induced concrete corrosion: a case study from a combined sewer network, *Cement and Concrete Research* 77, 16–25.
- Guimarães, A.T.C., Climent, M.A., de Vera, G., Vicente, F.J., Rodrigues F.T., and Andrade, C. (2011). Determination of chloride diffusivity through partially saturated Portland cement concrete by a simplified procedure. *Construction and Building Materials* 25, 785–790.
- Halabe, U. B., Sotoodehnia, A, Maser, K. R., and Kausel, E. A. (1993). Modeling the Electromagnetic Properties of Concrete. *ACI Materials Journal* 90 (6), 552-563.
- Hamann, G.; Tronicke, J. (2011) Assessing uncertainties in determining GPR ground wave velocities: an approach based on spectral velocity analysis. 6th. International Workshop of Advanced Ground Penetrating Radar. Aachen, Germany.
- Hasan, M.I. and Yazdani, N. (2014). Ground penetrating radar utilization in exploring inadequate concrete covers in a new bridge deck. *Cases Studies in Construction Materials* 1, 104-144.
- Hasan, M.I. and Yazdani, N. (2016). An Experimental Study for Quantitative Estimation of Rebar Corrosion in Concrete Using Ground Penetrating Radar. *Journal of Engineering*, Volume 2016, Article ID 8536850, 8 pp.
- Hansson, C.M., Poursaee, A. and Jaffer, S.J. (2012). Corrosion of Reinforcing Bars in Concrete. *The Masterbuilder*, 106-124.
- He, J., Zhang, G., Hou, S., and Cai, C.S. (2011). Geopolymer-based smart Adhesives for Infrastructure Health Monitoring: Concept and Feasibility. *Journal of Materials in Civil Engineering* 23(2), 100-109.
- Herrmann, H., Pastorelli, E., et al. (2016) Methods for fibre orientation analysis of X-ray tomography images of steel fibre reinforced concrete (SFRC). *Materials Science* 51, 3772–83.

- Hobbs, B. and Kebir, M.T. (2007). Non-destructive testing techniques for the forensic engineering investigation of reinforced concrete buildings. *Forensic Science International* 167, 167–172.
- Hong, S., Lai, W.W-L., Wilsch, G., Helmerich, R., Helmerich, R., Gunter, T., and Wigggenhauser, H. (2004). Periodic mapping of reinforcement corrosion in intrusive chloride contaminated concrete with GPR. *Construction and Building Materials* 66, 671-684.
- Hong, S., Lai, W. W., Wilsch, G., Helmerich, R., Helmerich, R., Günther, T., and Wigggenhauser, H. (2014). Periodic mapping of reinforcement corrosion in intrusive chloride contaminated concrete with GPR. *Construction and Building Materials* 66, 671-684.
- Housner, G.W., Bergman, L.A., Caughey, T. K., Chassiakos, A. G., Claus, R. O., Masri, S. F., Skelton, R. E., Soong, T. T., Spencer, B. F., and Yao, J. T. P. (1997). Structural Control: Past, Present, and Future. *Journal of Engineering Mechanics* 123(9), 897-971.
- Hui, L. and Jinping, O., (2011). Structural Health Monitoring: From Sensing Technology Stepping to Health Diagnosis. *Procedia Engineering* 14, 753–760.
- Hubber, B., Hilbig, H., Drewes, J.E. and Muller, E., (2017). Evaluation of concrete corrosion after short- and long-term exposure to chemically and microbially generated sulfuric acid. *Cement and Concrete Research* 94, 36–48.
- Hugenschmidt, J. (2002). Concrete Bridge Inspection with a Mobile GPR System. *Construction and Building Materials* 16 (3), 147–154.
- Hugenschmidt, J. and Mastrangelo, R. (2006). GPR inspection of concrete bridges. *Cement & Concrete Composites* 28, 384–392.
- Hugenschmidt, J, and Kalogeropoulos A. (2009). The inspection of retaining walls using GPR. *Journal of Applied Geophysics* 67, 335–44.
- Jacobs, R.W. and Urban, R.T. (2016). Ground-penetrating radar velocity determination and precision estimates using common-midpoint (CMP) collection with handpicking, semblance analysis and cross-correlation analysis: a case study and tutorial for archaeologists. *Archaeometry* 58 (6), 987–1002.
- Jamil, M., Hassan, M.K., Al-Mattarneh, H.M.A., and Zain, M.F.M., (2013) Concrete dielectric properties investigation using microwave nondestructive techniques. *Materials and Structures* 46, 77–87.
- Jiang, G., Wightman, E., Bogdan, B.C., Yuan, Z., Bond, P.L., and Keller, J. (2014a) The role of iron in sulfide induced corrosion of sewer concrete. *Water Research* 49, 166-174.

- Jiang, G., Keller, J., and Bond, P.L., (2014b) Determining the long-term effects of H₂S concentration, relative humidity and air temperature on concrete sewer corrosion. *Water Research* 65, 152-169.
- Jiang, G., Sun, X., Keller, J., and Bond, P.L., (2015) Identification of controlling factors for the initiation of corrosion of fresh concrete sewers. *Water Research* 80, 30-40.
- Jol, H. M. (2009). *Ground Penetrating Radar: Theory and Applications* (1st edition). Elsevier Science, Amsterdam.
- Joseph, A.P., Keller, J., Bustamante, H., and Bond, P.L. (2012). Surface neutralization and H₂S oxidation at early stages of sewer corrosion: Influence of temperature, relative humidity and H₂S concentration. *Water Research* 46, 4235-4245.
- Kanli, A.I., Taller, G., Nagy, P., Tildy, P., Pronay, Z., and Toros, E. (2015). GPR survey for reinforcement of historical heritage construction at fire tower of Sopron. *Journal of Applied of Geophysics* 112, 79–90.
- Kilic, G. (2015). Using advanced NDT for historic buildings: towards an integrated multidisciplinary health assessment strategy. *Journal of Cultural Heritage* 16, 526–535.
- Kim, N.W., Lee, J., Lee, H., and Seo, J. (2014). Accurate segmentation of land regions in historical cadastral maps. *Journal of Visual Communication and Image Representation* 25,1262–1274.
- Klemm, R. (2009). *Applications of Space-Time Adaptative Processing*. The Institution of Engineering and Technology. Lightning Source UK Ltd., Milton Keynes.
- Klysz, G. and Balayssac, J.P. (2007). Determination of volumetric water content of concrete using ground-penetrating radar. *Cement and Concrete Research* 237,1164–1171.
- Kosno, Ł., Sławski, Ł., and Swit, G. (2016). GPR investigation of flexible soil-steel bridge structure. *Procedia Engineering* 156, 172–179.
- Krause, M., Hausherr, J., Burgeth, B., et al. (2010). Determination of the fibre orientation in composites using the structure tensor and local X-ray transform. *Journal of Material Science* 45(4), 888–896.
- Kurumisawa, K. and Nawa, T. (2016). Electrical Conductivity and Chloride Ingress in Hardened Cement Paste. *Journal of Advanced Concrete Technology* 14, 87-94.
- Kwon, S., Feng, M.Q., and Park, S.S. (2010) Characterization of electromagnetic properties for durability performance and saturation in hardened cement mortar. *NDT&E International* 43, 86-95.

- Lai, W.L., T. Kind, T. and Wiggerhauser, H. (2010) A Study of Concrete Hydration and Dielectric Relaxation Mechanism Using Ground Penetrating Radar and Short-Time Fourier Transform. *EURASIP Journal on Advances in Signal Processing*, Volume 2010, Article ID 317216, 14 pages.
- Lai, W.L. and Poon, C.S. (2012). Applications of nondestructive evaluation techniques in concrete inspection. *Hong Kong Institution of Engineers Transactions* 19, 34–41.
- Lai, W.L., Dérobert, X. and Annan, P. (2018). A review of ground penetrating radar application in civil engineering: a 30-year journey from locating and testing to imaging and diagnosis. *NDT and E International* 96, 58-78.
- Lalagüe, A., Lebens, M.A., Hoff, I., and Grøv, E. (2016). Detection of rockfall on a tunnel concrete lining with ground-penetrating radar (GPR). *Rock Mechanics and Rock Engineering* 49, 2811–2823.
- Lataste, J.F., Behloul, M., and Breyse, D. (2008). Characterization of fibers distribution in a steel fiber reinforced concrete with electrical resistivity measurements. *NDT&E International* 41, 638–647.
- Laurens, S., Balayssac, J-P., Rhazi, J. and Arliguie, G. (2002). Influence of concrete relative humidity on the amplitude of Ground-Penetrating Radar (GPR) signal. *Materials and Structures* 35, 198–203.
- Laurens, S., Balayssac, J., Rhazi, J., Klysz, G. and Arliguie, G. (2005). Non-destructive evaluation of concrete moisture by GPR: experimental study and direct modeling. *Materials and Structures* 38, 827–832.
- Lee, Y.H., Lee, S.W., Youn, J.R., et al. (2002). Characterization of fiber orientation in short fiber reinforced composites with an image processing technique. *Materials Research Innovations* 6, 65–72.
- Leng, Z. and Al-Qadi, I.L. (2014). An innovative method for measuring pavement dielectric constant using the extended CMP method with two air-coupled GPR systems. *NDT&E International* 66, 90–98.
- Leucci, G. (2012). Ground penetrating radar: an application to estimate volumetric water content and reinforced bar diameter in concrete structures. *Journal of Advanced Concrete Technology* 10, 411–422.
- Leucci, G., Negri, S. and Carrozzo, M.T. (2003). Ground Penetrating Radar (GPR): an application for evaluating the state of maintenance of the building coating. *Annals of Geophysics* 46 (3), 481-489.
- Li, S., Li, S., Zhang, Q., Xue, Y., Liu, B., Su, M., and Wang, S. (2010). Predicting geological hazards during tunnel construction. *Journal of Rock Mechanics and Geotechnical Engineering* 2(3), 232-242.

- Li, M., Anderson, N., Sneed, L., and Torgashov, E. (2016) Condition assessment of concrete pavements using both ground penetrating radar and stress-wave based techniques. *Journal of Applied Geophysics* 135, 297–308.
- Liu, J., Qiu, Q., Chen, X., Xing, F., Han, N., He, Y. and Yueshan Ma, Y. (2017). Understanding the interacted mechanism between carbonation and chloride aerosol attack in ordinary Portland cement concrete. *Cement and Concrete Research* 95, 217–225.
- Liu, J., Li, C., Liu, J. et al. (2011) Characterization of fiber distribution in steel fiber reinforced cementitious composites with low water-binder ratio. *Indian Journal of Engineering Material Sciences* 18, 449–457.
- Liu, J. and Sun, W. (2012). Assessment of fiber distribution in steel fiber mortar using image analysis. *Journal Wuhan University Technology- Materials Science*, 166–71.
- Lopez-Rodríguez F, Velasco-Herrera VM, Alvarez-Bejar R, Gomez-Chavez S, Gazzola J. (2016) Analysis of ground penetrating radar data from the tunnel beneath the Temple of the Feathered Serpent in Teotihuacan, Mexico, using new multi-cross algorithms. *Advances in Space Research* 58, 2164–2179.
- Lorenzo, H., Rial, F.I., Pereira, M., and Solla, M. (2011). A full non-metallic trailer for GPR road surveys. *Journal of Applied Geophysics* 75, 490–497.
- Luo, T., Lai, W.W.L., Chang, R.K.W., and Goodman, D., (2019). GPR Imaging Criteria. *Journal of Applied Geophysics* 165, 37–48.
- Maas, C. and Schmalzl, J. (2013) Using pattern recognition to automatically localize reflection hyperbolas in data from ground penetrating radar. *Computers & Geosciences* 58, 116-125.
- Maierhofer, C., Brink, A., Rollig, M. and Wiggenhauser, H. (2003). Detection of shallow voids in concrete structures with impulse thermography and radar. *NDT&E International* 36, 257–263.
- Mason, T.O., Campo, M.A., Hixson, A.D., Woo, L.Y. (2002) Impedance spectroscopy of fiber-reinforced cement composites. *Cement and Concrete Composites* 24, 457–65.
- Mazurek, E. and Łyskowski, M. (2012). Practical application of high resolution ground penetrating radar method inside buildings. *Geological Geophysical Environment* 38, 439–48.
- McMichael, I. (2010). A Note on the Brewster Angle in Lossy Dielectric Media. Technical Paper, Night Vision and Electronic Sensors Directorate, 9 p.
- Monteiro, V.M. de A., Lima, L.R. and Silva, F. de A. (2018). On the mechanical behavior of polypropylene, steel and hybrid fiber reinforced self-consolidating concrete. *Construction and Building Materials* 188, 280-291.

- Moreno, J.D., Bonilla, M., Adam, J.M., Borrachero, M.V., and Soriano, L. (2015). Determining corrosion levels in the reinforcement rebars of buildings in coastal areas. A case study in the Mediterranean coastline. *Construction and Building Materials* 100, 11–21.
- Moyo, P., Brownjohn, J.M.W., Suresh, R., and Tjin, S.C. (2005). Development of fiber Bragg grating sensors for monitoring civil infrastructure. *Engineering Structures* 27, 1828-1834.
- Neal, A. (2004). Ground-penetrating radar and its use in sedimentology: principles, problems and progress. *Earth-Science Reviews* 66, 261–330.
- Orlando, L. and Slob, E. (2009). Using multicomponent GPR to monitor cracks in a historical building. *Journal of Applied Geophysics* 67, 327–334.
- Ozyurt, N., Mason, T.O., and Shah, S.P. (2006a). Non-destructive monitoring of fiber orientation using AC-IS: an industrial-scale application. *Cement and Concrete Research* 36(9), 1653–1660.
- Ozyurt, N., Woo, L.Y., Mason, T.O., et al. (2006b) Monitoring fiber dispersion in fiber-reinforced cementitious materials: comparison of AC-impedance spectroscopy and image analysis. *ACI Materials Journal* 103(5), 340–347.
- Pastorelli, E. and Herrmann, H. (2016). Time-efficient automated analysis for fibre orientations in steel fibre reinforced concrete. *Proceedings of the Estonian Academy of Sciences* 65(1), 28–36.
- Pereira, S. P., Rosman, P. C. C., Alvarez, C., Schetini, C. A. F., Souza R. O., and Vieira, R. H. S. F. (2015). Modeling of coastal water contamination in Fortaleza (Northeastern Brazil). *Water Science & Technology* 72 (6), 928-936.
- Pereira, E.V. (2017). Influence of steel fibers in the mechanical behavior and cracking mechanisms of self-consolidating concretes (in Portuguese). M.Sc. dissertation, Pontifical Catholic University of Rio de Janeiro, Brazil. 170 p.
- Pérez-Gracia, V., F. García García, F., and Rodríguez Abad, I. (2008a). GPR evaluation of the damage found in the reinforced concrete base of a block of flats: A case study. *NDT&E International* 41, 341–353.
- Pérez-Gracia, V., González-Drigo, R., and di Capua, D. (2008b). Horizontal resolution in a non-destructive shallow GPR survey: an experimental evaluation. *NDT&E International* 41, 611– 620.
- Pérez-Gracia, V., García, F., Pujades, L.G., Gonzalez, D.R., and di Capua, D. (2008c). GPR survey to study the restoration of a Roman monument. *Journal of Cultural Heritage* 9, 89–96.
- Pérez-Gracia, V., di Capua, D., González-Drigo, R., and Pujades, L., (2009). Laboratory characterization of a GPR antenna for high-resolution testing: radiation pattern and vertical resolution. *NDT&E International* 42, 336-344.

- Pitonak, M. and Filipovsky, J. (2016). GPR application – non-destructive technology for verification of thicknesses of newly Paved roads in Slovakia. *Procedia Engineering* 153, 537–549.
- Previati, M., Godio, A., and Ferraris, S. (2011). Validation of spatial variability of snowpack thickness and density obtained with GPR and TDR methods. *Journal of Applied Geophysics* 75, 284-293.
- Ranalli, D., Scozzafava, M., and Tallini M. (2004) Ground penetrating radar investigations for the restoration of historic buildings: the case study of the Collemaggio Basilica (L'Aquila, Italy). *Journal of Cultural Heritage* 5, 91–99.
- Rhee, J., Kim, H., Ock, C., & Choi, J. (2018). An investigation of the deterioration characteristics of concrete bridge decks with asphalt concrete in Korea. *KSCE Journal of Civil Engineering* 22(2), 613–621.
- Rhee, J-Y., Choi, J-J., and Kee, S-H. (2019). Evaluation of the Depth of Deteriorations in Concrete Bridge Decks with Asphalt Overlays Using Air-Coupled GPR: A Case Study from a Pilot Bridge on Korean Expressway. *International Journal of Concrete Structures and Materials* 13 (23), 1-17.
- Rial, F., Lorenzo, H., Pereira, M., and Armesto, J. (2009). Analysis of the Emitted Wavelet of High-Resolution Bowtie GPR Antennas. *Sensors* 9(6), 4230-4246.
- Rucka, M., Lachowicz, J., and Zielinska, M. (2016) GPR investigation of the strengthening system of a historic masonry tower. *Journal of Applied Geophysics* 131, 94–102.
- Sandmeier, K.J. (2019). REFLEXW Windows™ XP/7/8/10-program for the processing of seismic, acoustic or electromagnetic reflection, refraction and transmission data (Version 9.0). Karlsruhe, Germany. 664 p.
- Sbartai, Z.M., Laurens, S., Balayssac, J-P., Gérard Ballivy, B. and Arliguie, G., (2006) Effect of Concrete Moisture on Radar Signal Amplitude. *ACI Materials Journal* 103(6), 419-426.
- Shen, H., Nutt, S., and Hull, D. (2004) Direct observation and measurement of fiber architecture in short fiber-polymer composite foam through micro-CT imaging. *Composite Science and Technology* 64(13–14), 2113–2120.
- Shihab, S. and Al-Nuaimy, W. (2005). Radius estimation for cylindrical objects detected by ground penetrating radar. *Subsurface Sensing Technologies and Applications* 6(2), 151-166.
- da Silva, G.C.S., Christ, R., Pacheco, F., de Souza, C.F.N., Gil, A.G., and Tutikian, B.F. (2020). Evaluating steel fiber-reinforced self-consolidating concrete performance. *Structural Concrete* 21, 448–457.
- Slater, J. C. and Frank, N. H. (1947). *Electromagnetism*. McGraw-Hill Book Company, New York.

- Solla, M., Asorey-Cacheda, R., Núñez-Nieto, X., and Conde-Carnero, B. (2016) Evaluation of historical bridges through recreation of GPR models with the FDTD algorithm. *NDT&E International* 77, 19–27.
- Song, Y., Wightman, E., Tian, Y., Jack, K., Li, X., Zhong, H., Bond, P.L., Yuan, Z., and Jiang, G., (2019) Corrosion of reinforcing steel in concrete sewers. *Science of the Total Environment* 649, 739–748.
- Soroushian P, Lee CD. (1990) Distribution and orientation of fibers in steel fiber reinforced concrete. *ACI Materials Journal* 87(5), 433–439.
- Sterling, R., Simicevic, J., Allouche, E., Condit, W., and Wang, L. (2010). State of Technology for Rehabilitation of Wastewater Collection Systems U.S. Environmental Protection Agency, Washington, DC, EPA/600/R-10/078.
- Stryk, J., Matula, R., and Pospisil K. (2013) Possibilities of ground penetrating radar usage within acceptance tests of rigid pavements. *Journal of Applied Geophysics* 97, 11–26.
- Sun, M., Bastard, C. L., Pinel, N., Wang, Y., Li, J., Pan, J., & Yu, Z. (2017). Estimation of time delay and interface roughness by GPR using modified MUSIC. *Signal Processing* 132, 272-283.
- Sun, X., Jiang, G., Chiu, T.H., Zhou, M., Keller, J., and Bond, P.L. (2016). Effects of surface washing on the mitigation of concrete corrosion under sewer conditions. *Cement and Concrete Composites* 68, 88-95.
- Szymczyk, M. and Szymczyk, P. (2013). Processing of GPR Data. *Image Processing & Communication* 8 (2-3), 83-90.
- Taner, M. T. and Koehler, F. (1969) Velocity spectra-digital computer derivation and applications of velocity functions. *Geophysics* 34 (6), 859-881.
- Tillard, S., Dubois, J. C. (1995) Analysis of GPR data: wave propagation velocity determination. *Journal of Applied Geophysics* 33, 77– 91.
- Topczewski, L., Fernandes, F.M., Cruz, P.J., and Lourenço, P.B. (2007). Practical implications of GPR investigation using 3D data reconstruction and transmission tomography. *Journal of Building Appraisal* 3, 59–76.
- Torrents, J.M., Juan-García, P., Patau, O., and Aguado A. (2009). Surveillance of steel fibre reinforced concrete slabs measured with an open-ended coaxial probe. *Proceedings of the XIX IMEKO world congress: fundamental and applied metrology, Lisbon, Portugal*, 2282–2284.
- Torrents, J.M., Blanco, A., Pujadas, P., et al. (2012) Inductive method for assessing the amount and orientation of steel fibers in concrete. *Materials Structures* 45, 1577–1592.

- Utsi, E., 2017. Ground penetrating radar: theory and practice. Elsevier Science & Technology, Amsterdam.
- van Damme, S., Franchois, A., de Zutter, D., and Taerwe, L. (2004) Nondestructive determination of the steel fiber content in concrete slabs with an open-ended coaxial probe. *IEEE Transactions of Geoscience Remote Sensing* 42(11), 2511–21.
- Vandewalle L, Heirman G, Rickstal FV. (2008) Fibre orientation in self-compacting fibre reinforced concrete. In: Gettu R, editor. Proceedings of 7th international RILEM symposium on fibre reinforced concrete, India, Chennai: 719–728.
- Varela-Gonzalez, M., Solla, M., Martínez-Sanchez, J., and Arias P. (2014) A semi-automatic processing and visualisation tool for ground-penetrating radar pavement thickness data. *Automation in Construction* 45, 42–49.
- Varnavina, A. V., Sneed, L. H., Khamzin, A. K., Torgashov, E. V., & Anderson, N. L. (2015). An attempt to describe a relationship between concrete deterioration quantities and bridge deck condition assessment techniques. *Journal of Applied Geophysics* 142, 38–48.
- Vieira, J.D. (2003). Theoretical-Experimental Behavior Study of Composite Deck-Slab with Incorporated Formed Steel Shape (in Portuguese). M.Sc. Dissertation, Graduate Program on Civil Engineering, Pontifical Catholic University of Rio de Janeiro, 104 p.
- Wansom, S., Kidner, N.J., Woo, L.Y., and Mason, T.O. (2006) AC-impedance response of multi-walled carbon nanotube/cement composites. *Cement and Concrete Composites* 28, 509–519.
- Whitmer, R. M. (1963). *Electromagnetics* (2nd edition). Prentice-Hall, Upper Saddle River, New Jersey.
- Woo, L., Wansom, S., Ozyurt, N., Mu, B., Shah, S., and Mason, T. (2005). Characterizing fiber dispersion in cement composites using AC-Impedance Spectroscopy. *Cement and Concrete Composites*, 27(6), 627-636.
- Xiang, L., Zhou H-L., Shu, Z., Tan, S-H., Liang, G-Q., Zhu, J. (2013). GPR evaluation of the Damaoshan highway tunnel: a case study. *NDT&E International* 59, 68–76.
- Xie, X., Qin, H., Yu, C., and Liu, L. (2013). An automatic recognition algorithm for GPR images of RC structure voids. *Journal of Applied Geophysics* 99, 125–34.
- Xu, J., Jiang, L., Wang, W., and Jiang, Y. (2011) Influence of CaCl₂ and NaCl from different sources on chloride threshold value for the corrosion of steel reinforcement in concrete. *Construction and Building Materials* 25, 663–669.

- Xu, X., Peng, S., Xia, Y., and Ji, W. (2014) The development of a multi-channel GPR system for roadbed damage detection. *Microelectronics Journal* 45,1542–55.
- Yang, C.Y., Xu, M.X., and Chen, W.F. (2007). Reliability analysis of shotcrete lining during tunnel construction. *Journal of Construction Engineering and Management* 133 (12), 875-981.
- Ye, H., Jin, N., Jin, X., Fu, C., and Chen, W. (2016). Chloride ingress profiles and binding capacity of mortar in cyclic drying-wetting salt fog environments. *Construction and Building Materials* 127, 733–742.
- Yu, Q-M., Zhou, H-L., Wang, Y-H., and Duan R-X. (2016) Quality monitoring of metro grouting behind segment using ground penetrating radar. *Construction and Building Materials* 110,189–200.
- Zak, G., Park, C.B., and Benhabib B. (2001) Estimation of three-dimensional fibre-orientation distribution in short-fibre composites by a two-section method. *Journal of Composite Materials* 35(4), 316–39.
- Zanzi, L. and Arosio, D (2013). Sensitivity and accuracy in rebar diameter measurements from dual-polarized GPR data. *Construction and Building Materials* 48,1293–301.
- Zhang, S., Liao, L., Song, S., and Zhang, C., (2018) Experimental and analytical study of the fibre distribution in SFRC: A comparison between image processing and the inductive test. *Composite Structures* 188, 78–88.
- Zhang, S, Zhang, C., Liao, L., Wang, C., and Zhao, R., (2020) Investigation into the effect of fibre distribution on the post-cracking tensile strength of SFRC through physical experimentation and numerical simulation. *Construction and Building Materials* 248, paper 118433.
- Zhou, X., Chen, H., and Li. J. (2018). An Automatic GPR B-Scan Image Interpreting Model. *IEEE Transactions on Geoscience and Remote Sensing* 56 (6), 3398-3412.
- Zhu, J. and Popovics, J. (2005). Non-contact imaging for surface-opening cracks in concrete with air-coupled sensors. *Material Structures* 38, 801–806.